Activation of Samples in the Secondary Neutron Flux Generated with a 66 MeV Proton Beam on a Radionuclide Production Target

By

Mogakolodi Adolf Motetshwane
Reg. No: 14100381

BSc(Physics) (UB), NQF level 8 (Medical Physics) (Wits)

Department of Physics and Astronomy,
Faculty of Sciences,
Botswana International University of Science and Technology
motetshwanem@biust.ac.bw, (+267)71110428

A thesis submitted to the Faculty of Sciences in Partial Fulfilment of the Requirements for the Degree of Master of Science (Physics) of BIUST

Supervisors: Prof G.C. Hillhouse
Department of Physics and Astronomy,
Faculty of Sciences, BIUST
hillhouseg@biust.ac.bw, (+267) 7531 5505

Signature: _____ Date: 11/02/2019

Dr. G.F. Steyn
Department of Subatomic Physics, iThemba LABS
deon@tlabs.ac.za, +27 (21) 8431141

Signature: _____ Date: 11/02/2019

Dr. B.S. Batlokwa
Department of Chemical and Forensic Sciences,
Faculty of Sciences, BIUST
batlokwab@biust.ac.bw, (+267) 72364794

Signature: _____ Date: 12/02/2019

February, 2019

Declaration

I, Mogakolodi Adolf Motetshwane, declare that this thesis is my own original work, unless otherwise referenced or acknowledged. It is being submitted for the degree of Master of Science (Physics) in the Botswana International University of Science and Technology and has not been presented nor under consideration for any degree or examination in any other university for a similar or any other degree award.



_____

__11th__day of: __February__2019

Abstract

Activation of Samples in the Secondary Neutron Flux Generated with a 66 MeV Proton Beam on a Radionuclide Production Target

In this work, a small activation chamber was specially designed to facilitate the irradiation of selected samples with secondary neutrons behind a radionuclide production target in the vertical-beam target station (VBTS) at iThemba LABS. The main aim was to assay the radionuclides formed in the samples, with a special interest in those of medical importance. The experiment was performed simultaneously with a routine radionuclide production run, during which the target was bombarded with a 66 MeV proton beam with a nominal beam intensity of 220 μA. The target was a tandem Rb/Ga target for production of the relatively long-lived radionuclides ^{82}Sr and ^{68}Ge, receiving an accumulated charge of 20 000 μAh. Twenty-two materials were selected for neutron activation, covering a large mass region from 7 to 209 atomic mass units (amu). Activated samples ranging from ^{7}Be to ^{209}Bi were assayed for their gamma-ray emissions by means of a high-purity germanium (HPGe) detector. Based on these activation data, physical yields were determined for all uniquely identified reaction products.

The experimental yields measured in this project are compared with yield predictions based on neutron fluxes obtained from Monte Carlo simulations with the radiation transport code MNCP 6.1 in conjunction with evaluated cross sections for neutron-induced reactions from the TENDL-2015 and TENDL-2017 nuclear data libraries. Six different physics selections were employed in the Monte Carlo simulations, leading to several sets of predicted results.

Activation products from a total of 104 nuclear reactions have been observed cleanly, more than 40 of which are used in medical applications. In the majority of cases the yields are too low for this method to be profitably exploited in a routine radionuclide production facility. In several cases the specific activities of the radionuclides will be too low for use in medical applications. In a few cases the use of secondary neutrons clearly has potential. Six medically interesting radionuclides have been singled out for further scrutiny, namely ^{46}Sc, ^{59}Fe, ^{103}Ru,^{141}Ce, ^{161}Tb and ^{203}Hg. Although the production rates are generally low, the produced quantities are nevertheless sufficient for research purposes, e.g. radiochemical separation studies, the development of methods for radiolabeling of biomolecules, calibration sources for radiation detectors, etc.

One of the principle aims of this study is to obtain information that will assist the design of future target stations for the proposed 70 MeV cyclotron facility at iThemba LABS, on the aspect of making provision for suitable infrastructure that will exploit the secondary neutrons. There is a renewed interest worldwide to exploit neutrons emitted from high-power targets, which iThemba LABS has not hitherto investigated or implemented. As 66 MeV proton beams are routinely available, close to the design energy of a new generation of commercial 70 MeV cyclotrons, iThemba LABS has a unique opportunity to make a contribution in the context of future production facilities, utilizing secondary neutrons, in this important energy region.

Acknowledgements

I would like to start by expressing my gratitude to my supervisor and mentor, Prof Gregory Hillhouse, through whom I met a patient, knowledgeable and experienced co-supervisor, Dr Deon Steyn. I have never acquired so much knowledge in such a short period of time. I would also like to thank Dr Peane Maleka, who opened doors for me by patiently introducing me to the Monte Carlo simulation code and for always making sure that my visits to iThemba LABS were smooth and fruitful. Above all, I am grateful to Dr Batlokwa for the financial support, encouragement and guidance when there seemed to be no light at the end of the tunnel.

To the Director of iThemba LABS and his management team, I appreciate every decision you took to make sure that my visits to your institute were productive. A special thanks to Drs Rudolf Nchodu and Rudzani Nemutudi for your inspiring presentations given at BIUST in mid 2016, which opened doors for me to this amazing research facility. To Dr Clive Naidoo and your Radionuclide Production team, your patience and having been always welcoming me when I needed assistance at your department helped me to finally get my project completed. I would also like to express my gratitude to Drs Fhumulani Nemulodi and Joele Mira for your assistance with accelerator physics. Ntombi Kheswa, the training you gave us on target making was a rare opportunity and I am very grateful to you for that.

To the friendly iThemba LABS postgraduate students, thank you all for your hospitality and having always been willing to assist me where you could. A special thanks to Ms Mistura Bolaji Ajani for your assistance with LaTeX issues. To Mr Lindsey Davids and your team of professional drivers, without you my arrivals and departures from iThemba LABS would not have been so memorable. To Hombakazi “Hombie” Wanana, you are an asset to iThemba LABS, that is all I can say. My thanks also to the National Research Foundation (NRF). Through iThemba LABS I have benefitted much and I really appreciate the financial assistance received. The rare opportunities that I could experience, especially the worthwhile iThemba LABS Summer School and the Student Practice in Russia at the Joint Institute of Nuclear Research (JINR), are gratefully acknowledged.

Once again I would like to thank Prof Hillhouse, Dr Oscar Kureba, Dr Jacobus Diener and all the BIUST nuclear physics post graduate students for your critical and helpful comments during the Nuclear Physics Team (BIUST) weekly meetings. My acknowledgements would be incomplete without mentioning the BIUST physics teaching assistants (TAs) who stood in for me so that I could work on my research project at iThemba LABS.

Last but not least, I would like to thank my family, whom at times I could not be with when you desperately needed me. I appreciate that you respected my decision to concentrate on my academic work and the unconditional moral support that you gave me. Glory be to God, who makes all things possible.

Table of Contents

Declaration i
Abstract iii
Acknowledgements v

1 Motivation and Outline **1**
1.1 INTRODUCTION 1
1.1.1 Why accelerator production methods for medical radioisotopes? 2
1.2 THE PROPOSED SOUTH AFRICAN ISOTOPE FACILITY (SAIF) 3
1.3 PREVIOUS STUDIES 4
1.4 OBJECTIVES OF THIS PROJECT 5
1.5 OUTLINE OF THESIS 6

2 Experimental Methods **7**
2.1 THE VERTICAL-BEAM TARGET STATION 7
2.2 NEUTRON ACTIVATION CHAMBER 8
2.3 TARGET COMPOSITION 9
2.4 NEUTRON-ACTIVATED SAMPLES 11
2.5 BOMBARDMENT 11
2.6 RADIONUCLIDE ASSAYS 12

3 Monte Carlo Simulations **15**
3.1 OVERVIEW AND HISTORY 15
3.2 NUCLEAR MODELS AND PHYSICS SELECTIONS 16
3.3 GEOMETRY SPECIFICATION 18
3.4 PROTON BEAMS AND PARTICLE HISTORIES 19
3.5 NEUTRON SPECTRA 22

4 Data Analysis **25**
4.1 PREDICTED YIELDS 25
4.1.1 Energy-group structure 26
4.1.2 Pointwise and group-averaged cross sections 27
4.1.3 The mean formation cross section 30
4.1.4 Accumulated charge 31
4.1.5 Physical yield 32
4.2 EXPERIMENTAL YIELDS 32

4.3 COMPARISON BETWEEN CALCULATED AND EXPERIMENTAL YIELDS 34
4.3.1 Indicators of relative difference 34
4.3.2 The logarithmic mean 36
4.3.3 Indicator of relative difference using the logarithmic mean 37
4.3.4 Percentage difference of physical yields 37
4.3.5 Log percentage difference of physical yields 38
4.4 EFFECTIVE CROSS SECTIONS AND UNCERTAINTIES 38

5 Results and Discussion **41**
5.1 NEUTRON-INDUCED ACTIVATION PRODUCTS 41
5.2 SENSITIVITY OF CAPTURE REACTIONS ON GROUP STRUCTURE 45
5.3 PHYSICAL YIELDS 46
5.3.1 Dependence on physics selection 48
5.3.2 Average neutron spectrum and yield outliers 60

6 Summary and Conclusions **65**

A Selected Applications **67**
A.1 SCANDIUM-46 67
A.2 IRON-59 67
A.3 RUTHENIUM-103 69
A.4 CERIUM-141 69
A.5 TERBIUM-161 70
A.6 MERCURY-203 71

B MCNP 6.1 input code to model the VBTS **73**

C Calculated physical yields: TENDL-2015 **81**

D Calculated physical yields: TENDL-2017 **85**

E Acronyms and Abbreviations **89**

References **91**

Chapter 1

Motivation and Outline

1.1 INTRODUCTION

This work focuses on the production of radioisotopes using secondary neutrons generated by a 66 MeV proton beam on a radionuclide production target at the cyclotron facility of iThemba LABS, located near Cape Town, South Africa. Currently, most of the routine radionuclide production at this laboratory is performed with primary proton beams of 66 MeV, which is the same energy that has been used for neutron therapy for many years. These beams are delivered by the separated-sector cyclotron (SSC), which can accelerate protons up to 200 MeV for research in basic and applied nuclear physics as well as related applications. The current long-range plan (LRP) of iThemba LABS [AZA2018], however, includes the purchase of a dedicated 70 MeV cyclotron for radionuclide production to free the SSC for pursuing the research objectives of the laboratory. The project reported here is the first investigation utilizing the secondary neutrons emitted from a radionuclide production target at iThemba LABS, mainly to get an idea of the production rates that can be achieved and whether provision must be made to exploit these neutrons on the future 70 MeV cyclotron facility.

The distinctive physical and chemical properties of various radionuclides play a notable role in technological applications of importance to today's society and are substantial to a broad range of scientific investigation. One field in which the importance of radionuclides cannot be overstated is medicine. To make major breakthroughs in this field, it is essential to first address the availability issue of those radionuclides of primary interest. Worldwide, radionuclides and radiopharmaceuticals are used extensively for different procedures in diagnostic nuclear medicine and radiotherapy [HRI2007].

For example, a radionuclide can be attached to a biomolecule that selectively delivers it to the diseased area and that is often the best way to diagnose and/or treat the disease, usually cancer, which is among the highest priorities in Botswana [CHA2013]. The country succeeded in addressing the HIV/AIDS epidemic but as the HIV/AIDS survivors are now aging, they become more susceptible to cancer, a disease that has now become increasingly common. Most common are breast cancer, cervical cancer, prostate cancer, head and neck cancer, and Kaposi's sarcoma in both women and men. The sad truth is that many patients present with the disease in its advanced stages, consequently the survival rate is very low and mortality is almost seventy-five percent (see e.g. Morhason-Bello et al. [MOR2013]). In actual fact, cancer

kills more people globally than HIV/AIDS. The Sub-Saharan Africa region is predicted to have a greater than eighty-five percent increase in cancer burden by 2030 [MOR2013].

Radionuclides and radiopharmaceuticals are already very successful in fighting certain types of cancer. Even though other treatment methods such as chemotherapy and surgery are available, in certain cases the inventive use of radionuclides in targeted radiotherapy gives greater flexibility and its use in the treatment of cancer is expected to become increasingly important in the future (see e.g. Adelstein and Manning [ADE1995]). Some radionuclides have the advantage of serving as concentrated sources of radiation when localized within the diseased cells or organs, while largely preventing damage to adjacent healthy cells – the so-called collateral damage [ADE1995, SHA2005]. Examples of this will be discussed in Chapter 6.

Two important features of radionuclides need to be highlighted. Firstly, they can be used in extremely minute amounts, as low as 10^{-10}g of radioactive material, which does not disturb the physiological functions of the patient when administered [WEI1975]. Secondly, they can selectively be delivered to specific body tissues or organs, such as the bone marrow, red blood cells, the liver, the kidneys and many others to cure/treat or diagnose diseases [SCH2009]. Radionuclide production with accelerators has become increasingly important in the world.

1.1.1 Why accelerator production methods for medical radioisotopes?

Although many radionuclides have potential applications in diagnostic nuclear medicine and/or radiotherapy, the ultimate choice of the radioisotope is based on the type of emitted radiation, energy, half-life, ease of production, availability and cost (see e.g. Rajendran [RAJ2007]). One of the mature and commonly used production regimens for radionuclides, namely via a nuclear reactor (either by neutron activation or by nuclear fission) has both advantages and disadvantages. Even though reactors offer a large irradiation volume and high production yields, some of the major production reactors are old, closing down and not being replaced. This results in shortfalls of certain important radionuclides (e.g. ^{99}Mo and its daughter ^{99m}Tc). Secondly, most reactors use highly-enriched ^{235}U (HEU), which is discouraged by the Non-Proliferation Treaty (NPT) due to proliferation concerns, the on-going usage of HEU and significant accumulation of high-level fission waste. To reduce the proliferation risks, the Reduced Enrichment in Research and Test Reactors (RERTR) Programme was implemented in 1978 to convert the HEU to low-enriched uranium (LEU) fuels [GLA2005, RAG2013]. Some HEU reactor facilities have already converted to LEU but that resulted in lower efficiency, more waste and hence significant increase in production costs. Since nuclear reactors are being shut down worldwide, the complementary way to produce medical radionuclides via particle accelerator is becoming increasingly important. In addition to being less expensive, nuclear weapon proliferation free and adaptable to a local population size, the particle accelerator route has some notable advantages. Schlyer et al. [SCH2009] discussed this based on the following points:

- Suitable chemical and/or physical means for separation can usually be found.
- No-carrier-added products of high specific activity can be obtained because the targets and product isotopes are normally not of the same element.

- In many cases, fewer radionuclidic impurities are formed when selecting the most appropriate target material, bombarding particle and the ideal energy for irradiation.

This project should be seen in the context of the proposed South African Isotope Facility (SAIF), which will consist of two parts: (1) Accelerator Centre for Exotic Isotopes (ACE Isotopes); (2) Accelerator Centre for Exotic Beams (ACE Beams). This initiative is discussed briefly below.

1.2 THE PROPOSED SOUTH AFRICAN ISOTOPE FACILITY (SAIF)

The routine production of radionuclides at iThemba LABS is performed with a 66 MeV proton beam supplied by a K = 200 separated-sector cyclotron (SSC), located at Faure (near Cape Town) in South Africa. The SSC facility recently celebrated 30 years of beam operations, shared predominantly by radionuclide production, radiotherapy and nuclear physics research. The load in terms of beam time for these three programmes on the same cyclotron is a limitation, taking into consideration that beam time is a scarce commodity and in high demand. This has become more so in recent years due to a continuous increase in the demand for certain high-value radionuclides, both for medical and industrial applications.

To increase the beam time for radionuclide production and nuclear physics research, the establishment of a new facility, currently known as the South African Isotope Facility (SAIF) has been proposed [AZA2018]. The new facility will consist of two parts:

1. Accelerator Centre for Exotic Isotopes (ACE Isotopes) will be a dedicated facility for radionuclide production. A commercial, high-current 70 MeV H^- cyclotron for this purpose will free the SSC and allow an increase in beam time for nuclear physics and related research. Such a cyclotron can provide dual beams of up to 350 μA each, which will increase the current production capacity at iThemba LABS by about a factor of 3.

2. Accelerator Centre for Exotic Beams (ACE Beams) will be a Radioactive Ion Beam (RIB) facility for nuclear physics research. The SSC will be used as a driver for an Isotope Separation On-Line (ISOL) facility. A 66 MeV proton beam of up to 50 μA will be delivered by the SSC to produce radioactive beams from a target ion source. The first stage of this project will be a Low-Energy Radioactive Ion Beam (LERIB) Project without post acceleration. The second stage will be the post acceleration of the radioactive beams with a linear accelerator to energies of between 4 and 5 MeV per nucleon. Some of the funding has been secured for the development of LERIB and work on that project is in progress.

With the above "roadmap" for the future of iThemba LABS in place, a design study on new target stations for radionuclide production with a dedicated 70 MeV cyclotron has commenced. This work is now at an advanced stage.

One aspect was recently added to the ACE Isotopes project, namely an investigation into the feasibility to utilize the secondary neutron flux behind a routine production target for producing a number of high-value radionuclides that cannot be produced with a proton beam. Recent studies at the Isotope Production Facility (IPF) at the Los Alamos National Laboratory (LANL), utilizing a proton beam energy of 100 MeV, have shown that such "parasitic" productions have definite potential (see e.g. Engle et al. [ENG2012, ENG2013, ENG2014] and Mosby et

al. [MOS2016]). Important previous work with relevance to the present investigation was also performed at the Medium Energy Intense Neutron (MEIN) beam facility of Brookhaven National Laboratory (BNL), where secondary neutrons were produced by bombarding a water-cooled Cu-beamstop with a 200 MeV proton beam (see e.g. Katcoff et al. [KAT1975] and Mirzadeh et al. [MIR1983]). The proton beam was delivered by the same linear accelerator that provides beam to the Brookhaven Linear Isotope Producer (BLIP). Important aspects of the studies at LANL and BNL will be highlighted in several subsequent chapters.

The current routine production energy of 66 MeV at iThemba LABS is close enough to 70 MeV to perform experiments that can shed light on requirements for the dedicated 70 MeV cyclotron facility proposed for ACE Isotopes. An experiment was therefore designed to activate samples of materials in the secondary neutron flux directly behind the target in one of the existing high-intensity target stations, the vertical-beam target station (VBTS) [STE2013].

1.3 PREVIOUS STUDIES

Katcoff et al. [KAT1975] reported a considerable increase in the ratio of neutron-rich to neutron-deficient radionuclides with reactions induced by the secondary neutrons in comparison to the primary protons, but the resulting activity levels were low. These authors presented effective cross sections for various (n,xn), (n,pxn) and (n,αxn) reactions on a selection of targets covering a reasonably large mass region (^{24}Mg to ^{142}Ce); the neutron flux was reported to be "in excess of 1×10^{11} neutrons cm^{-2} s^{-1} in the energy region 25 to 200 MeV". One would not expect an overall different scenario with regards to low effective cross sections as the incident proton-beam energy is decreased. It is therefore not surprising that the LANL results [ENG2012, ENG2013, ENG2014] at 100 MeV show a similar trend to those of Katcoff et al. [KAT1975]. The broad energy spectra of secondary neutrons emitted by thick targets lack the selectivity of the "ideal energy windows" that can often be exploited in reactions by charged particles. Spectrum-averaged cross sections also usually have relatively low values.

The more important reactions are those where charged particles are emitted, leading to different atomic species than the target material. This is important if the product radionuclides have to be chemically separated from the target matrix, which is the case in the majority of applications of practical interest. Unfortunately, there is a general trend for the (n,pxn) and (n,αxn) reactions to have even lower cross sections than the (n,xn) reactions, except at very low masses [KAT1975]. This disadvantage of low effective cross sections can only be overcome by utilizing a sufficiently high neutron flux.

Engle et al. [ENG2014] reported a total neutron flux of about 1×10^{12} neutrons cm^{-2} s^{-1} directly behind a routine production target at the IPF while under bombardment with a 100 MeV proton beam of 250 μA, with approximately 50% of the neutrons having energies above 1 MeV. They made the point that this neutron flux is beyond that of typical medical cyclotrons and distinctly different from that of reactors. With the significant increase in obtainable beam intensities evident in modern accelerators, there is a renewed interest in exploiting the secondary neutrons, in particular as aging research reactors are being closed down and often not replaced. It has been reported that, in contradiction to their importance, experimental cross-section data for neutron-induced reactions are sparse above 14 MeV, i.e. the energy ob-

tainable with ^{3}He(d,n)^{4}He neutron generators [QAI1974]. Most certainly, one would prefer to have complete excitation functions for neutron-induced reactions to work with instead of only effective cross sections, the latter of which have limited value when predictions are required for a different energy region. As a result of this lack of experimental data, neutron spectra obtained from nuclear model calculations often have to suffice in yield predictions, leading to large uncertainties and errors up to an order of magnitude in exceptional cases [ENG2014]. Experimental data are challenging to obtain as monoenergetic neutron sources do not exists except at quite low energies. So-called quasi-monoenergetic neutron (QMN) facilities are few in the world, with limited beam time due to sharing with other programmes. This situation is not expected to dramatically change anytime soon.

Despite their limitations, effective cross sections are useful as they do provide some constraints for model calculations. Until such time when better "monoenergetic" experimental cross-section data become available, effective cross sections for neutron-induced reactions will remain important.

1.4 OBJECTIVES OF THIS PROJECT

From the outset, it was clear that we would be confronted with relatively low effective production cross sections in the neutron flux behind a VBTS target. On the other hand, there are extensive routine productions throughout the year, mostly for the production of the relatively long-lived radionuclides ^{22}Na, ^{68}Ge and ^{82}Sr. The radionuclide production programme receives about 50% of the total beam time available on the SSC (in recent times even a little bit more than 50%). The total accumulated charge on target is approaching one million μAh per year, which translates into a large number of neutrons that are currently not utilized. Should the ACE Isotopes proposal become a reality, these numbers will be even significantly higher. It therefore seems prudent to investigate the possible use of these neutrons to produce useful radionuclides. Since the bombardments in the VBTS are typically quite long, with the nominal accumulated charge in a single run not less than 20 000 μAh, the focus with neutron-induced reactions should similarly be on relatively long-lived radionuclides. The idea is to perform neutron-induced reaction experiments is a commensalistic way with routine radionuclide production runs, e.g. in such a manner that the usual weekly beam schedule is not disturbed or affected in any way.

The advent of commercial 70 MeV cyclotrons with high-intensity, dual-beam capability is relatively recent. We are not aware of any dedicated studies to date that focused on utilizing the secondary neutrons on these machines. A number of experiments are therefore planned, some with enriched target materials. For the first experiment, however, it was decided to activate only natural target materials, covering a wide mass region (7–209 amu). The various tasks and objectives of this first study are as follows:

- To design and build a small activation chamber that can be located in close proximity behind a standard VBTS target holder. Devise a method to place this chamber into position and to retrieve it without disrupting the routine production programme.

- Collect a relatively large number of samples to activate with secondary neutrons during a routine production with 66 MeV protons in the VBTS. The selection should cover a wide mass region.
- After the activation, to assay all the samples for their induced radioactivity with an off-line gamma-ray spectrometer system.
- Analyze all the measured spectra and derive production yields for all reaction products that can be identified uniquely.
- Perform calculations and simulations in order to make predictions of all observed yields. Select a state-of-the-art Monte Carlo radiation transport code for this purpose to simulate the VBTS and to find in this way the expected neutron spectrum in the location of the activation chamber. Find the most recent evaluated cross-section data for the relevant neutron-induced reactions and use only those values for the calculated predictions.
- Find an appropriate way to compare the yield predictions with the corresponding measurements, where the number of radionuclides may be quite large.
- Estimate to what extent the predictions can be trusted when no experimental data exist.
- Finally, to derive and list the effective cross sections for all the observed reaction products.

1.5 OUTLINE OF THESIS

- Chapter 2 describes the experimental methods of this work, including a description of the VBTS and its targetry, the neutron activation chamber, the bombardment during which the samples of this study were activated, and the subsequent radionuclide assays.
- Chapter 3 presents the Monte Carlo simulations of the VBTS, a routine production tandem target and the 66 MeV proton beam. A brief description of the relevant nuclear models and physics selections is given, followed by a discussion on the resulting neutron spectra.
- Chapter 4 is dedicated to the analysis of both the measured and Monte Carlo raw data to arrive at the final experimental and predicted yields. A description is also given of the methods employed to compare the measured and predicted yields.
- The experimental results and corresponding predictions based on the Monte Carlo simulations are presented and discussed in Chapter 5, including an in-depth comparison of the various data sets of physical yields generated in this study. A few medically relevant radionuclides that can be considered for production with secondary neutrons are singled out. The reasons for their importance are briefly discussed in Appendix A.
- A summary and conclusions are presented in Chapter 6.

Chapter 2

Experimental Methods

In this chapter, the experimental methods and relevant equipment are described, including the vertical-beam target station (VBTS) and its targetry. In addition to the neutron activation chamber that was specifically built for this work, the list of samples activated inside this chamber is presented. A description of the detector set-up used to identify and quantify the activation products in the samples is also given.

2.1 THE VERTICAL-BEAM TARGET STATION

The vertical-beam target station (VBTS) was developed at iThemba LABS for the bombardment of larger-format targets in order to increase the beam intensity. It is a dedicated facility for the production of long-lived, high value radionuclides, such as ^{22}Na, ^{68}Ge and ^{82}Sr [STE2013]. The accumulated charge in a routine bombardment is typically between 20 000 and 30 000 μAh at a beam intensity between 200 and 250 μA. The majority of targets bombarded in the VBTS are tandem targets. A photograph of the VBTS is shown in Fig. 2.1. Routine bombardments in this facility commenced in 2006. Some of the main features of the VBTS are as follows:

- Targets are remotely transported and transferred to and from the target station in order to limit the radiation exposure to staff. Target transport is by means of an electrified rail system and the transfer to and from the station is facilitated with a robot arm.
- During bombardment, the target is completely surrounded with a thick radiation shield. This protects the vault and its contents from becoming excessively activated and it also reduces radiation damage to sensitive components and materials, e.g. components made of polymer materials.
- The VBTS can only accommodate one target holder, i.e. it does not have a magazine for additional target holders. Since the objective of this facility was the production of relatively long-lived radionuclides, it was foreseen that target exchanges would be relatively few and that a target would remain inside the station for a relatively long period (at least several days). A magazine for target holders was therefore deemed unnecessary.
- The beam is swept in a circular fashion around the beam axis in order to spread it on target. This is to better distribute the heat generated inside the target and to prevent overheating at potential “hot spots”.

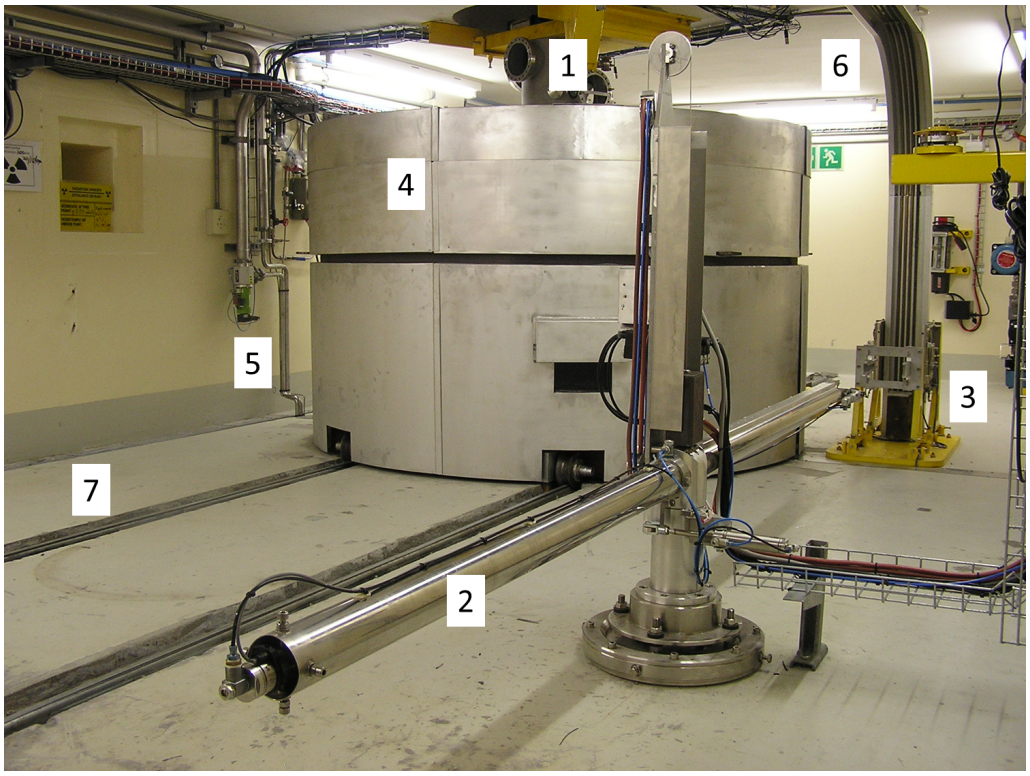


Figure 2.1: Vertical-beam target station (VBTS), showing (1) the diagnostic chamber on the vertical beamline, (2) the robot-arm for target exchanges, (3) the target transporter terminus, (4) the local radiation shield, (5) inlet and outlet lines for cooling water, (6) the electrified rail for target transport, and (7) the rail on which shielding sectors move when opening the station. The ceiling is 2 m above the floor of the irradiation vault.

- Targets are irradiated outside the vacuum of the cyclotron and beamline. This is a measure to protect the integrity of the vacuum during bombardment. A helium-cooled Havar window isolates the vacuum from the outside atmosphere. The Havar foils are thin, nominally 50 μm, which cause minimal degradation to the incident beam energy.

- The targets are water cooled during bombardment. The connection of the water inlet and outlet lines to a target holder is facilitated with an electro-pneumatically controlled pusher assembly.

2.2 NEUTRON ACTIVATION CHAMBER

The neutron activation chamber constructed for this study is a small holder that encloses the targets/samples when subjected to the secondary neutron flux. In this way the samples become radioactive. The utilization of secondary neutrons behind a VBTS target was not foreseen when this target station was designed and built. Fortunately, there is a cavity in the pusher assembly (the device that places and holds the target in the irradiation position) right behind the VBTS target holder, where a small neutron activation chamber can be accommodated. The pusher assembly is located in the central region of the station, a photograph of which is shown in Fig. 2.2. (Note that this assembly is shown on a workshop bench and not in its final position inside the VBTS).

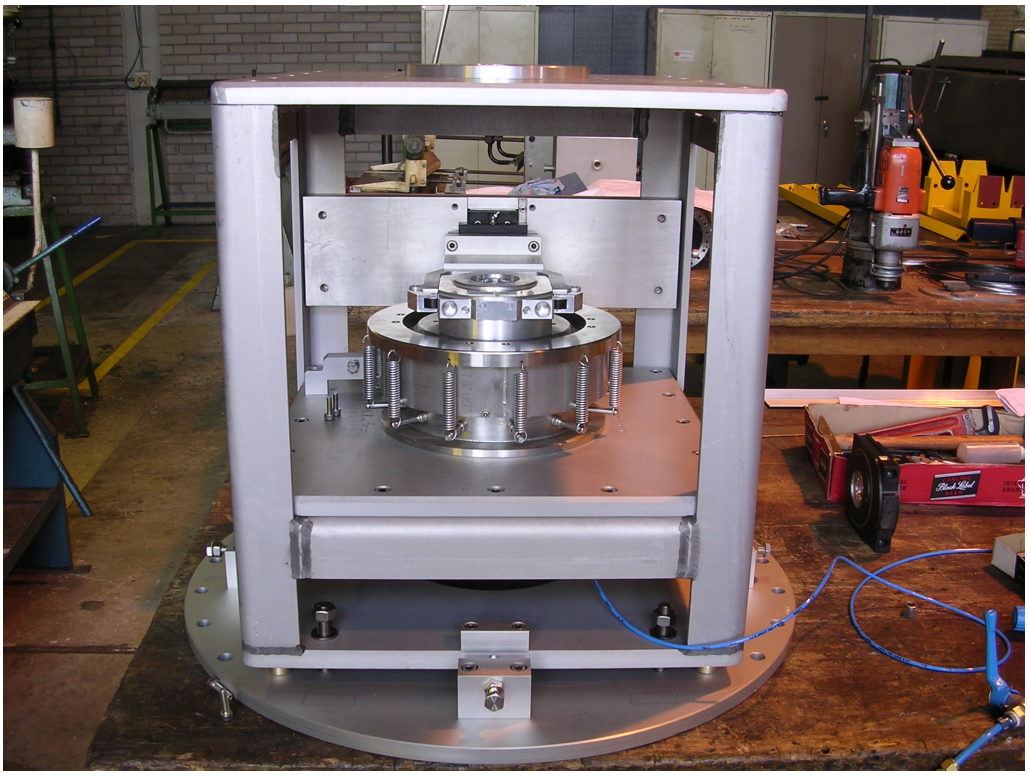


Figure 2.2: Central region of the VBTS. A target holder is shown on top of the pusher assembly.

A spare pusher assembly was available at iThemba LABS. This unit had never been used with beam and was not radioactive, therefore it was ideal for fitting and testing the procedure for loading/unloading the neutron activation chamber. The chamber can be placed inside the pusher assembly by means of a 2 m long rod with a suction cup on one end. Practice runs were performed on the spare pusher assembly before attempting the procedure on the VBTS. The procedure is shown in Fig. 2.3. The inside cavity of this particular chamber has a diameter of 70 mm and 10 mm in height. The chamber was machined out of Polyvinyl Chloride (PVC).

The PVC proved not to be a good material for this purpose. Fortunately, the chamber did survive a 20 000 μAh bombardment but became discoloured and cracked due to radiation damage. Two new chambers were subsequently machined out of aluminium to replace this one for our further studies.

2.3 TARGET COMPOSITION

The 66 MeV proton beam traverses many layers of materials during the bombardment of a VBTS target. In this study, a tandem Rb/Ga target was bombarded in a usual ^{82}Sr/^{68}Ge routine production; the neutron activation being performed in commensalistic mode (i.e. neutrons which were produced as by-products during the routine production were taken advantage of to activate samples but without interfering with the normal production). Table 2.1 shows the material layers of the tandem target. The beam is expected to stop in layer no. 12, namely Ga metal, which will be in a molten state when there is beam on target. A photograph as well as an exploded view of a tandem target is shown in Fig. 2.4.

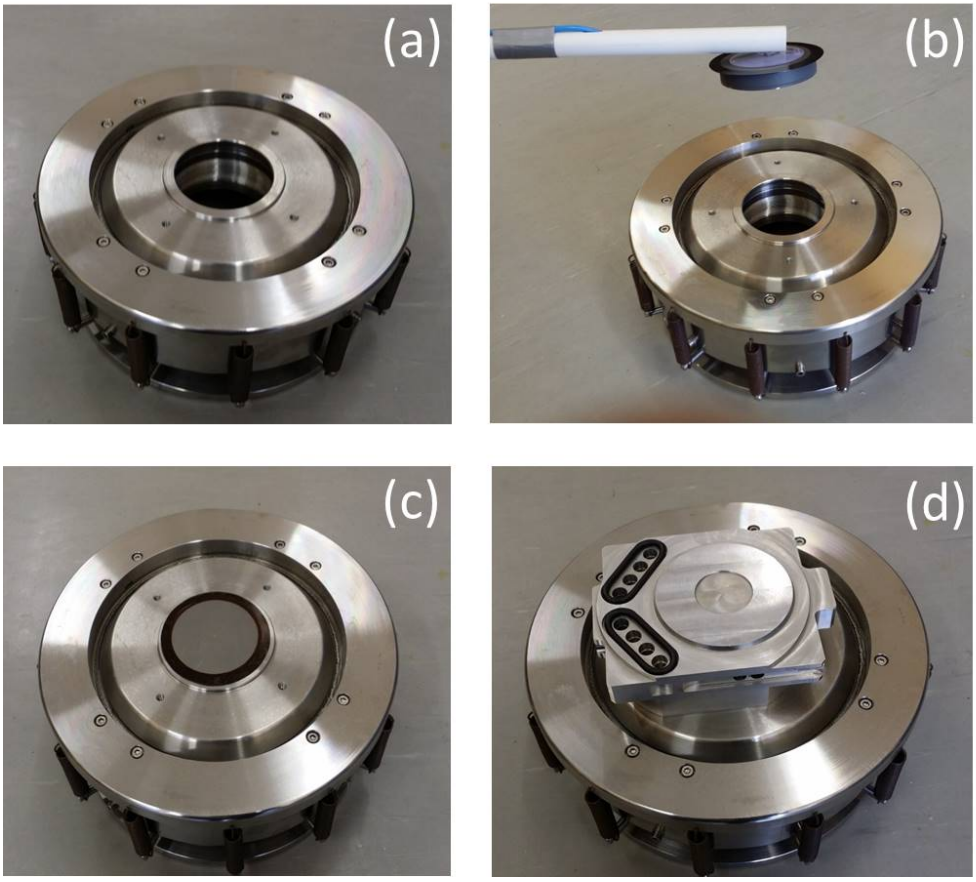


Figure 2.3: Loading the neutron activation chamber into the spare VBTS pusher assembly. (a) Cavity in the centre of the pusher assembly. (b) Neutron activation chamber, located at the end of a 2 m rod with a suction cup, ready to be placed inside the cavity of the pusher assembly. (c) Positioning the chamber. (d) Positioning of target holder over the activation chamber.

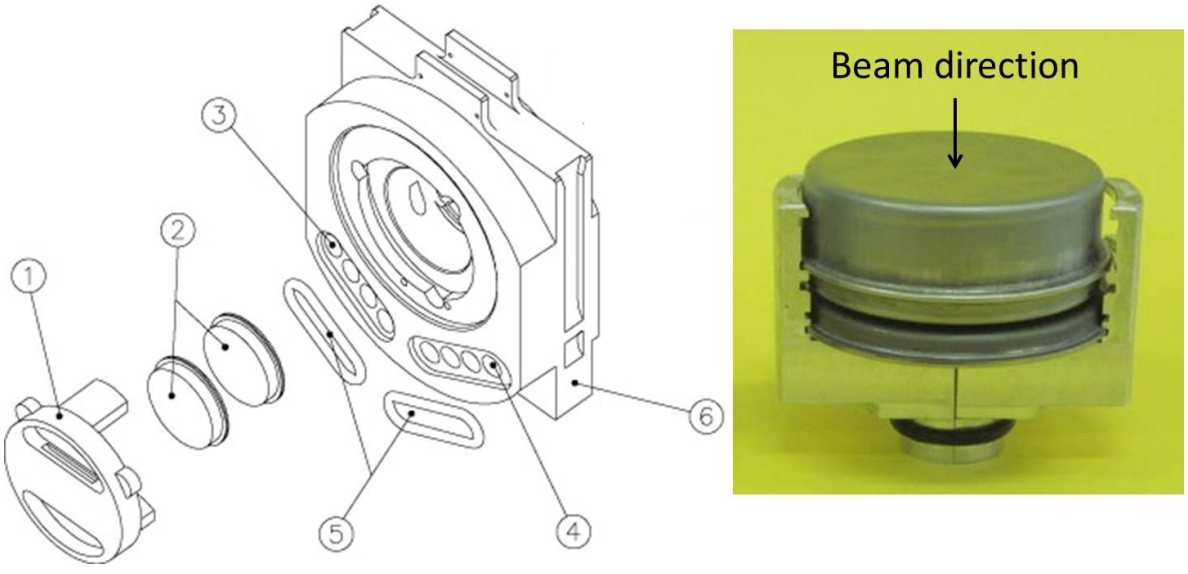


Figure 2.4: Left panel: Exploded view of the target holder and tandem targets, showing (1) aluminium back end (plug) with bayonet fitting, (2) two encapsulated targets, (3) cooling-water inlet ports, (4) cooling-water outlet ports, (5) moulded rubber seals, (6) aluminium body of target holder. Right panel: Tandem target assembly.

Table 2.1: VBTS target-material layers located on the 66 MeV proton-beam axis.

Layer no.	Material	Thickness	Comments
1	Havar	50 μm	50 mm diameter
2	Helium gas	15 mm	High flow-rate coolant between the two Havar foils: 25 °C, 1.25 bar
3	Havar	50 μm	50 mm diameter
4	Air	2 mm	Target holder is bombarded in atmosphere
5	Aluminium	2 mm	Entrance window of target holder
6	H_2O	1.2 mm	Cooling-water layer no. 1
7	Stainless steel (S316)	0.5 mm	Capsule wall
8	Rubidium metal	17 mm	Target material for ^{82}Sr production
9	Stainless steel (S316)	0.5 mm	Capsule wall
10	H_2O	1.2 mm	Cooling-water layer no. 2
11	Niobium metal	0.5 mm	Capsule wall
12	Gallium metal	3.75 mm	Target material for ^{68}Ge production
13	Niobium metal	0.5 mm	Capsule wall
14	H_2O	1.2 mm	Cooling-water layer no. 3
15	Aluminium	10 mm	Back end of target holder

2.4 NEUTRON-ACTIVATED SAMPLES

A list of the samples activated by secondary neutrons is presented in Table 2.2. The majority were single elements but there were also some compounds. All samples had natural isotopic composition, chosen from available stock at iThemba LABS with the main purpose to cover a wide mass region. All samples were made up to fit into small plastic bags, 13 mm by 13 mm after being sealed. The plastic became brittle during the bombardment but survived. The samples had to be handled with extreme care after bombardment until adhesive tape could be applied on both sides, prior to mounting them on counting frames.

2.5 BOMBARDMENT

The samples were activated over several days until the accumulated charge of the proton beam on target reached a value of 20 000 μAh, which is typical for such VBTS production runs. The typical beam current was about 220 μA. Figure 2.5 shows the beam history (i.e. the beam current versus time of the bombardment) and Fig. 2.6 shows the accumulated charge versus time. The bombardment was interrupted at times as the beamtime from the cyclotron is shared with other users. It was therefore crucial to keep a very good record of the beam history. The beam current and accumulated charge values were logged in 1 second intervals into a computer spreadsheet file. During the analysis, a shorter version of the file was created by converting the time scale from seconds to minutes. The values are plotted in Figs. 2.5 and 2.6.

Table 2.2: Targets/samples activated by neutrons behind a VBTS target.

Target material	Z	Mass (g)	Purity (%)	Supplier
^{9}Be	4	0.0104	99.5	Goodfellow, UK
^{23}Na (as NaI)	11	0.609	99.5	Sigma Aldrich, USA
^{nat}Ti	22	0.135	99.999	Goodfellow, UK
^{55}Mn	25	0.835	99.95	Goodfellow, UK
^{59}Co	27	0.983	99.9	Goodfellow, UK
^{nat}Ni	28	0.730	99.98	Goodfellow, UK
^{nat}Br (as CsBr)	35	0.694	99.5	Merck, Germany
^{nat}Rb (as RbCl)	37	0.473	99.8	Sigma Aldrich
^{89}Y	39	0.247	99.9	Goodfellow, UK
^{93}Nb	41	0.577	99.9	Goodfellow, UK
^{103}Rh	45	0.459	98.16	Reactor Experiments, USA
^{nat}Ag	47	0.362	99.95	Goodfellow, UK
^{115}In	49	0.635	99.99	Koch Chemicals
^{127}I (as NaI)	53	0.609	99.5	Sigma Aldrich, USA
^{133}Cs (as CsBr)	55	0.694	99.5	Merck, Germany
^{141}Pr	59	0.363	99.9	Goodfellow, UK
^{nat}Gd (as Gd_2O_3)	64	0.431	99.9	Sigma Aldrich, USA
^{169}Tm (as TmO)	69	0.696	99.9	Fluka, Switzerland
^{181}Ta	73	0.660	99.95	Goodfellow, UK
^{197}Au	79	0.436	99.99	Goodfellow, UK
^{nat}Tl (as TlCl)	81	0.531	>99.0	BDH Chemicals, UK
^{209}Bi	83	0.408	99.97	Goodfellow, UK

2.6 RADIONUCLIDE ASSAYS

The gamma radiation emitted by the neutron-activated samples were qualitatively and quantitatively analysed by means of an analytical technique known as gamma spectrometry. First, the activated samples were removed from the VBTS about 10 hours after the end of bombardment (EOB). They were subsequently mounted onto standardized source frames, which fit onto a movable source holder. A pair of rails that holds the source holder in position forms an integral component of the high-purity germanium (HPGe) detector set-up used for measuring the photon emissions from radioactive sources. The detector set-up and one of the source frames are shown in Fig. 2.7.

The distance between a source frame and the front face of the HPGe detector could be varied from 0 to 2 m. All neutron-activated samples were analysed repeatedly. They were quite radioactive shortly after EOB, thus the first counting session was performed with a source-detector separation of 2 m. The initial live-time was 1000 seconds per source with dead times below 5%; the HPGe system/program automatically displays the value of the dead time when γ-rays are detected. The second counting session commenced about 24 hours later, during

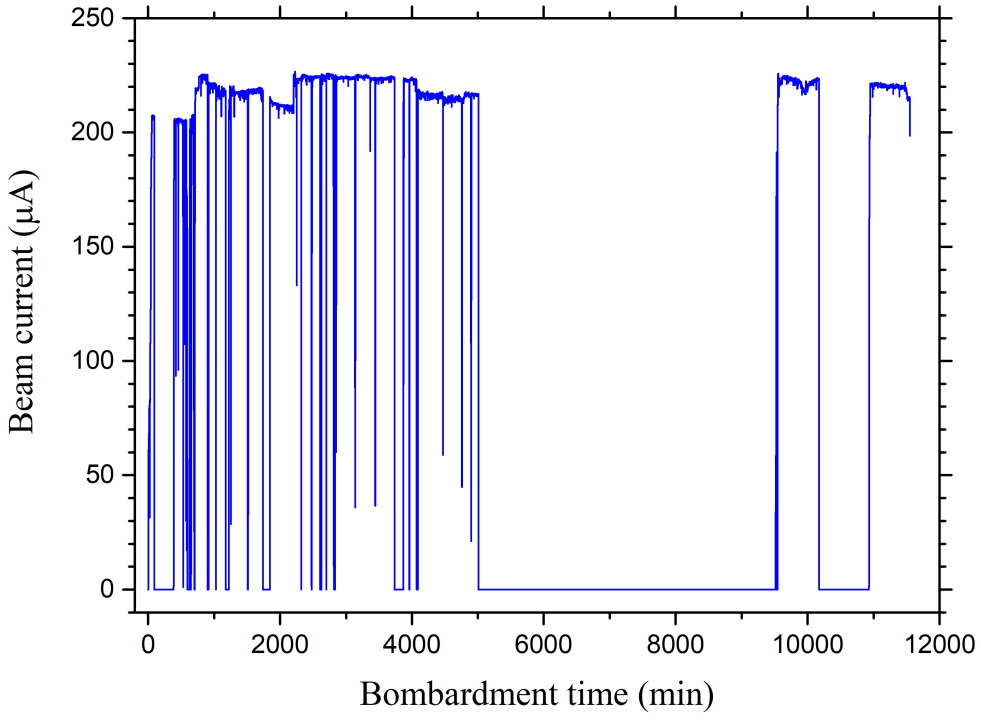


Figure 2.5: Beam current versus time of the bombardment with 66 MeV protons delivered by the separated-sector cyclotron (SSC).

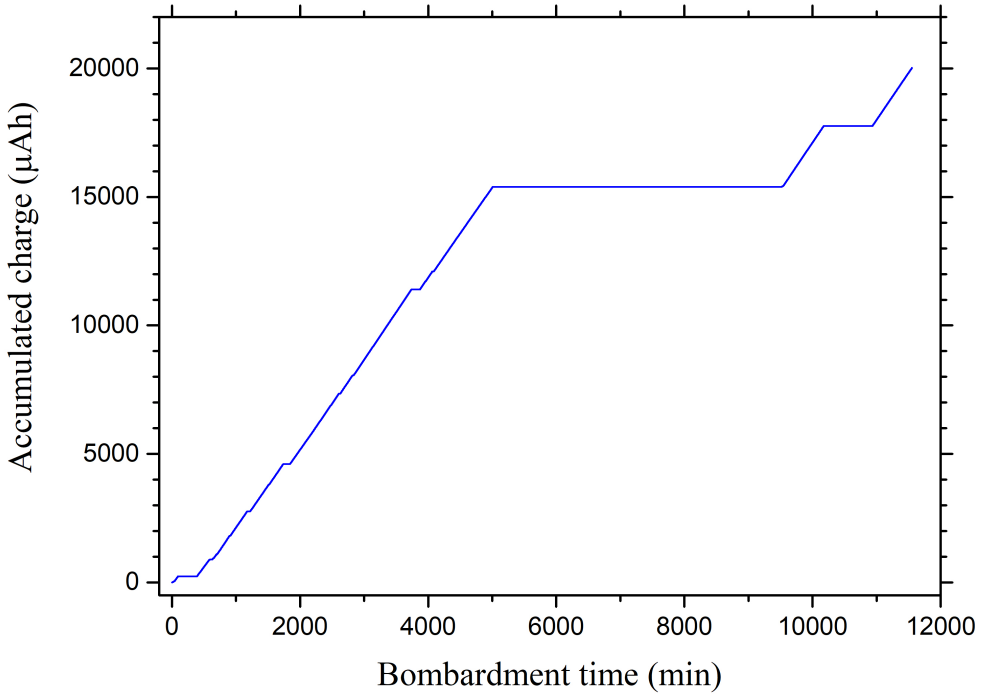


Figure 2.6: Accumulated charge versus bombardment time.

which all sources were counted for 30 min at a source-detector separation of 1 m, except in one case where the dead time (the recovery time during which a detector is inactive after having been subjected to radiation) was too large at 1 m. A third counting session, starting one week later, counted all samples for 8 hours each, also with a source-detector separation of 1 m. A fourth counting session was done a couple of months later, but only for selected samples that

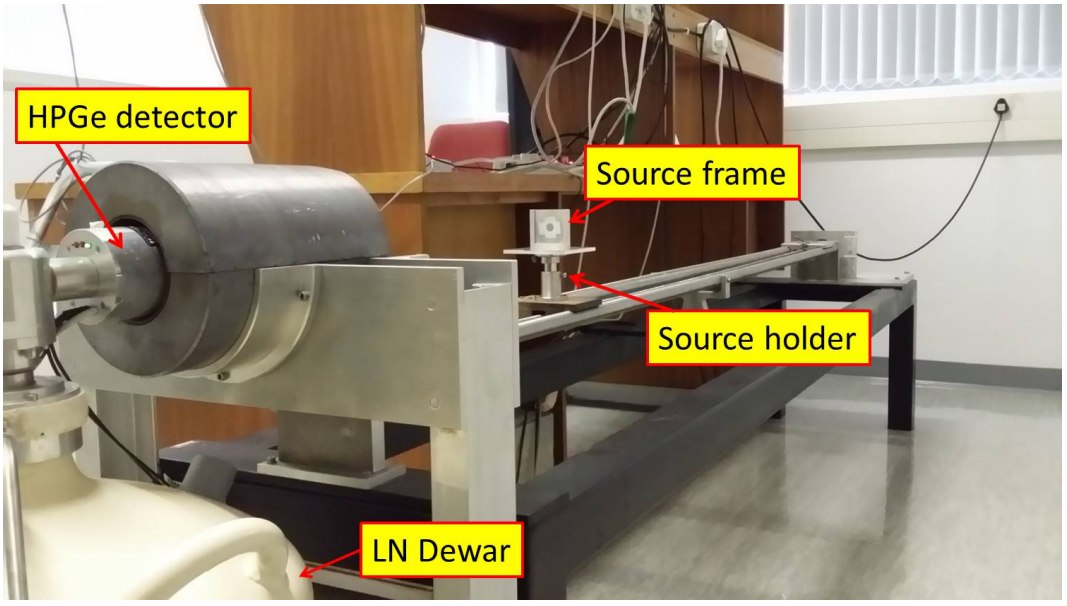


Figure 2.7: The liquid nitrogen (LN)-cooled high-purity germanium (HPGe) detector and other main components of the γ-ray counting set-up.

contained very long-lived radionuclides. The counting times varied but were typically around 24 hours. No counting was done with the sources closer than 1 m to the detector except in the case of the beryllium, as this sample was significantly smaller than the others and had less activity. The Be sample was counted closer to the detector (10 cm and 50 cm, respectively) to obtain sufficient counting statistics in a reasonable time. Source-detector separations smaller than 1 m were mainly avoided because of the deviation from point geometry of the activated samples. In a few cases, larger samples were subdivided into smaller samples and recounted, in order to investigate if self-absorption was a problem. For most reactions, self-absorption corrections were not necessary.

The efficiency calibration was performed with standardized counting sources, traceable to the National Institute of Standards and Technology (NIST) [NIST2018] in the USA. For this purpose, sealed ^{60}Co, ^{133}Ba and ^{152}Eu point sources were used. More information on the detector calibration will be provided in Chapter 4.

Chapter 3

Monte Carlo Simulations

In this chapter, the Monte Carlo simulations required to obtain energy spectra of secondary neutrons emitted from a radionuclide production target, during bombardment with a proton beam, are described. The Monte Carlo method is a recognized tool that has been implemented extensively to simulate the transport of radiation (such as charged particles, neutrons and gamma-rays) in the materials of complex engineered assemblies (such as accelerators, targets and nuclear reactors). The origin of the Monte Carlo method and what it is capable of, especially when combined with relevant physics models, are also briefly discussed.

3.1 OVERVIEW AND HISTORY

As already discussed in the previous chapter, the 66 MeV proton beam relevant to this study is incident onto a complex target that has 15 distinct material layers (see Table 2.1). As the protons traverse the target they are slowed down. About 7% of the protons will eventually induce nuclear reactions, leading to the emission of secondary neutrons. A dominant contribution is the so-called spallation neutrons, which comprise the high-energy component of the neutron spectrum. These neutrons typically have a long range in matter and can end up relatively far from where they are formed, creating more neutrons in further nuclear interactions along their respective paths. It is important to note that unlike charged particles, a well-defined range is not quantifiable for the uncharged neutrons as their trajectories in matter vary greatly due to dependencies on so many variables, including the scattering cross sections and macroscopic absorption. Highly excited nuclei formed in nuclear reactions, predominantly in the target but also in the shielding and other materials in the vault, will eventually de-excite, often leading to additional neutron emission. At the lowest end of the energy scale we have the so-called evaporation neutrons. Their emission is sometimes likened to the emission of atoms or molecules from a hot liquid drop. These neutrons are emitted from excited nuclei that have reached statistical equilibrium, i.e. where the excitation energy has dispersed to all constituent nucleons and their escape from the nucleus has become a purely statistical process. In between the evaporation and high-energy spallation energy scales one gets a neutron spectrum component that is predominantly from so-called preequilibrium (also called precompound) processes. These intermediate energy neutrons are emitted by excited nuclei that de-excite before reaching statistical equilibrium, i.e. earlier on in the evolution of a nuclear reaction. The only feasible way

to determine the complete neutron spectrum at any particular location in a complex system such as an irradiation vault containing a target station, a composite target and incident beam, is by means of Monte Carlo radiation transport calculations in which all the materials and the beam have been modelled with a significant degree of precision.

In this study, the Monte Carlo code MCNP 6.1 was used for modelling the VBTS and generating neutron spectra at the location of the sample chamber. MCNP is an acronym for Monte Carlo N-Particle [GOO2013, PEL2013], a software package mainly developed at the Los Alamos National Laboratory (LANL) in the USA. Monte Carlo codes such as MCNP provide simulation and computational modelling techniques for random sampling and statistical analysis to estimate mathematical functions and/or mimic the operations of complex systems. They are named after the gambling hot spot in Monaco, since chance and random outcomes are central to statistical simulations as much as they are to games of chance [HAR2010].

It is fascinating that Monte Carlo techniques are about as old as the modern computer as it was implemented already on the first generation of electronic computers by the early creators of these methods. In 1947 Enrico Fermi, while at Los Alamos, traced neutron movements through fissionable materials by means of the Monte Carlo method. Many different codes emerged during the 1950s and 1960s, some specialized for neutrons, others for photons, various mergings occurred to account for neutron-photon interactions, and ultimately more general three-dimensional particle transport capability and modelling developed. In 1977 such a merger resulted in the first version of MCNP, which originally stood for Monte Carlo Neutron Photon [GOO2013]. In 1983, MCNP 3 was first released for public distribution to the Radiation Safety Information Computational Centre (RSICC). The change of MCNP to mean Monte Carlo N-Particle was introduced in 1990 when electron transport was added. During the MCNP 4 era there was a split, where developers involved with the Accelerator Production of Tritium (APT) programme required the utility of many-particle transport (also called X-particle or eXtended-particle transport). This led to the separate development of MCNPX and MCNP 4. In the period 2001 to 2002, MCNP 4C was completely rewritten in modern Fortran 90, with support for large-scale parallel processing on multi-core computer systems, leading to MCNP 5. In July 2006, as a result of an insisting LANL management, the two development efforts merged, taking MCNPX 2.6 B and MCNP 5 to their last few individual releases but finally worked together to the single release of MCNP 6 in 2013. At the time of starting the present project, the latest version of the code was MNCP 6.1. In actual fact, the RSICC license and distribution lumped together three versions of the code, namely MCNPX 2.7, MCNP 5 and MCNP 6.1. The latest version was adopted for this work. The MCNP suite of codes is described as a general-purpose, many-particle, continuous-energy, generalized-geometry, time-dependent, Monte Carlo radiation transport code system.

3.2 NUCLEAR MODELS AND PHYSICS SELECTIONS

The MCNP 6.1 code was used to obtain the neutron spectrum in the small activation chamber located in the target pusher assembly (see Chapter 2). The generated neutron flux spectrum obtained from each Monte Carlo run was saved as an individual file, used for the calculation of activities induced in the activated samples but further calculations were strictly performed

outside of the MCNP code.

Physics models are needed to calculate the neutron flux at energies beyond about 20 MeV due to a lack of empirical data at higher energies for most materials [PEL2013, DEL2014]. In other words, "model physics" has to fill the gap where "table physics" (i.e. evaluated measured data) are not available or insufficient. Six different combinations of "physics model selections" were used in this study. Three of these models are conventional intranuclear cascade models, which have to be combined with an appropriate evaporation model in order to achieve the appropriate modelling for this study. Two different models can be invoked in MCNP for the evaporation stage. A fourth model has combined cascade and evaporation stages [PEL2013]. These models are briefly described below.

The basic assumption of the so-called intranuclear cascade (INC) models is that the interactions of high-energy particles with the nucleus can be represented by (or approximately described by) free particle-particle collisions inside the nucleus [ARM1980]. The important justification for this assumption is that the wavelength of the incident particle is of the order of the inter-nucleon distance. This physical process, approximately described by free two-body collisions within the nucleus, is called the cascade. This approximation is valid at sufficiently high excitation energies, typically above 100 MeV [LER2013]. The cascade process is normally followed by other physical processes, such as preequilibrium emission, evaporation, fission or de-excitation by photon emission [FIL2009]. In principle, the intranuclear cascade is a preequilibrium process but it is not usually described as such, since the cascade is usually terminated before equilibrium is reached, therefore another preequilibrium model is required to describe the further evolution of the nuclear reaction as it develops towards equilibrium.

Some of the earlier INC models are the Bertini and ISABEL models, dating back to the early 1960s but having undergone numerous developments and additions over the years. These models are standard options in MCNP. Filges and Goldenbaum [FIL2009], in their Handbook of Spallation Research, describe the Bertini model as the precursor of all modern INC models, including ISABEL, the Liège Intranuclear Cascade Model (INCL) and the Cascade-Exciton Model (CEM). The various INC models differ in their criteria to determine when a particle has left the cascade, i.e. when the first stage or cascade stage has ended. Spallation neutrons are mainly produced by inelastic intranuclear collisions during this stage.

A relatively new edition to the MCNP code is the Liège Intranuclear Cascade Model (INCL), developed by Joseph Cugnon and co-workers at the University of Liège, Belgium [KAI2011, LER2013]. The current version is INCL4. This model is most often used in combination with ABLA, which is a fission and evaporation code [GAI1991]. The alternative to ABLA for modelling the evaporation stage in MCNP 6.1 is usually referred to as Dresner, the originator of an evaporation code with great longevity used in various Monte Carlo codes [FIL2009, KON2011].

The default option in MCNP 6.1 is the Cascade-Exciton Model (CEM) [MAS2002]. The reaction is treated in three distinct stages. The first stage is the intranuclear cascade, in which primary particles can be re-scattered and produce secondary particles. These secondary particles can either be emitted or re-absorbed by the nucleus. The excited residual nucleus that remains after the cascade has a particle-hole configuration that is the starting point of the second stage, which is a preequilibrium stage treated in terms of the Modified Exciton Model

(MEM). The third stage is the evaporative final stage of an equilibrated nucleus. These are all handled by the same CEM model, thus, when this model is selected in the MCNP 6.1 code, the parameter selecting an evaporation-fission model is ignored [GOO2013]. The version implemented in MCNP 6.1 at the time of performing the simulations was CEM3.03.

The selections of physics models employed in this work are listed below:

1. Bertini/ABLA,
2. Bertini/Dresner,
3. CEM,
4. INCL/ABLA,
5. ISABEL/ABLA,
6. ISABEL/Dresner.

These are the same physics selections investigated by Feghhi et al. [FEG2015] in a study of the emission spectra of neutrons from a spallation target.

3.3 GEOMETRY SPECIFICATION

The MCNP Monte Carlo transport code uses a three-dimensional (3D) Cartesian coordinate system to specify or model regions of interest and dimensions are given in centimeters. A 3D model of the VBTS was developed by extensive use of standard macrobodies and surfaces available within the MCNP code [SHU2007, PEL2013]. The input file was developed in an iterative mode through many stages, each stage tested by plotting the geometry after adding a component or a material specification. The plotting was done by running MCNP with the plotting (P) specifier but not executing it (i.e. omitting the X specifier). In this way MCNP provides a visual inspection of the model as it progresses from stage to stage, also giving diagnostics, errors and warnings when mistakes are made. Thus, the model was built up step by step until the VBTS, the irradiation vault, beamline and the activation chamber were sufficiently represented. It was necessary to make some simplifications as it is not feasible to model every nut and bolt within a realistic time frame. In this regard, some judgements had to be made. We are, however, convinced that all the major components have been modelled with sufficient precision and that the bulk of the material budget within the model closely resembles that of the actual VBTS facility.

A number of figures below show the geometry set-up as modelled in MCNP. Figure 3.1 shows the vault and VBTS. Figure 3.2 zooms into the target region of the VBTS, while Fig. 3.3 zooms in further to show the activation chamber and its location relative to the tandem targets in more detail. The input file to generate the simulation is given in Appendix B. Note that the central part of the neutron activation chamber was blocked out so that samples could only be placed in a concentric volume inside the chamber. This was done in an effort to expose all samples to a similar neutron flux, i.e. to ensure that all samples were placed in such a way that they spanned the same azimuthal angular region with respect to the beam axis. This was only for the sake of this particular experiment due to the large number of samples to be activated. In

subsequent experiments, we will use the middle region also. The activation chamber containing the samples was modelled but not the actual samples. The Average Cell Flux Tally (F4 tally) was specified to fill the cavity of the activation chamber, which provided the average neutron flux in that region in units of neutrons/cm^2 per source proton.

3.4 PROTON BEAMS AND PARTICLE HISTORIES

This section describes how the beam was modelled in MCNP 6.1. The phrase "particle histories" refers to the number of primary particles, in this case incident protons, specified in a single Monte Carlo simulation run. Typically, a smaller number of particle histories is chosen when developing and testing a simulation, followed by longer runs with an increased number of particle histories once the input to the code has been fully developed and judged to be correct. A larger number of particle histories leads to improved statistics but at the cost of a longer execution time. It is often necessary to make a compromise between improving the statistics and reducing the execution time as a single run can last many days.

The proton beam was modelled in two ways, namely with uniform and Gaussian intensity profiles. In order to investigate the sensitivity of the generated neutron flux to the beam-spot size on target, several runs with a circular, uniform beam intensity profile were performed in which the beam diameter was systematically varied between 16 mm and 36 mm. Separate

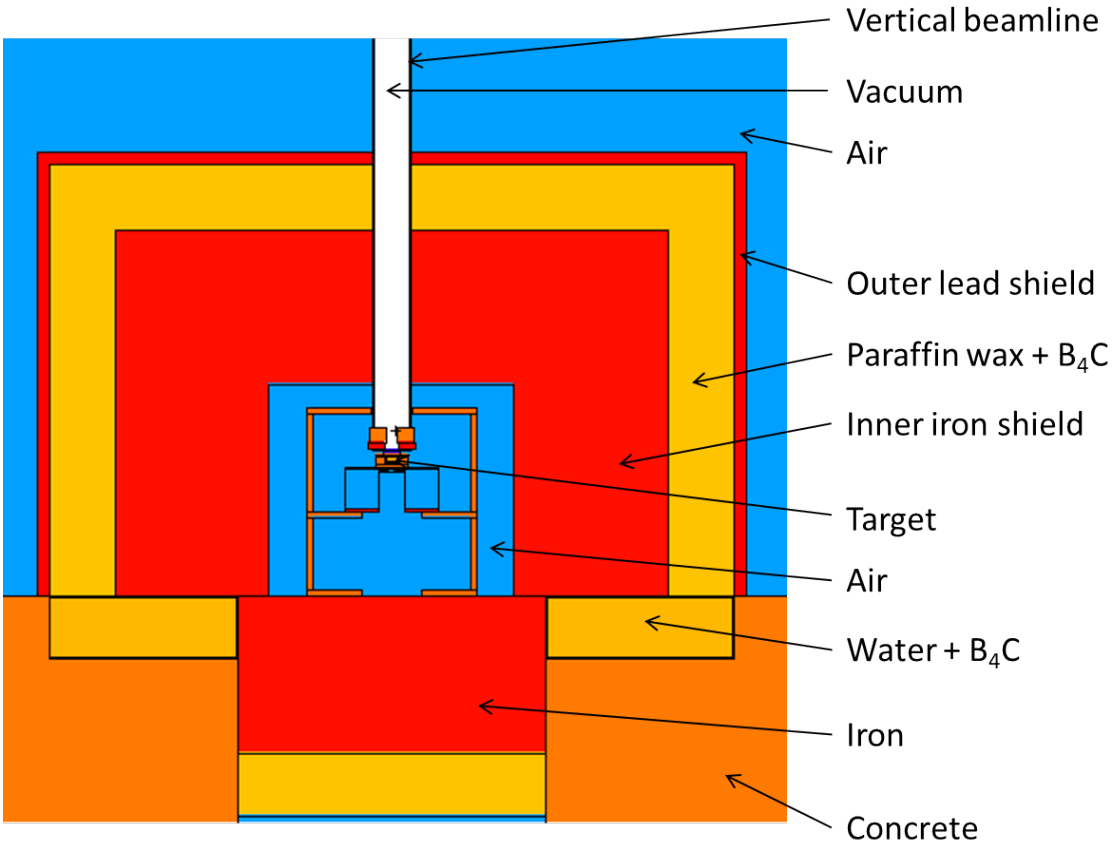


Figure 3.1: The VBTS geometry as generated with the MCNP visual editor. The specification in the visual editor was to assign different colours to different materials. This is a full view of the target station. Figures 3.2 and 3.3 zoom in further to show details of the target region.

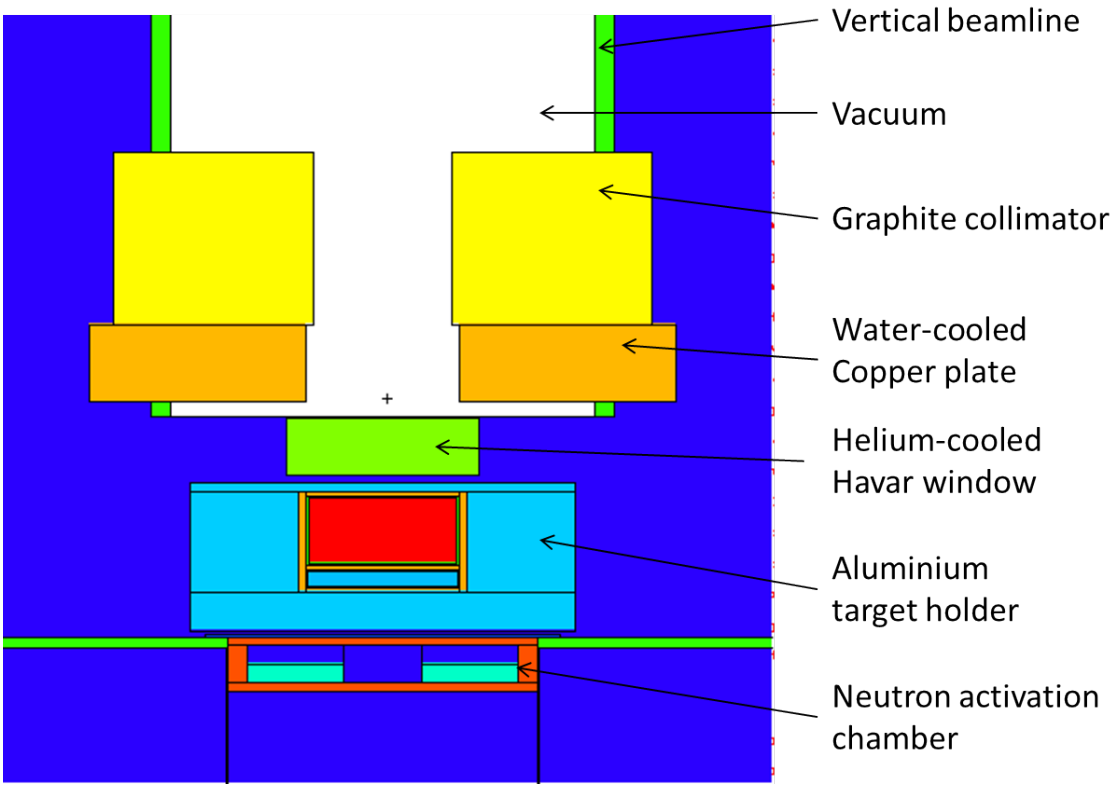


Figure 3.2: The VBTS geometry as generated with the MCNP visual editor. This view zooms in further to show the details of the collimator and target holder.

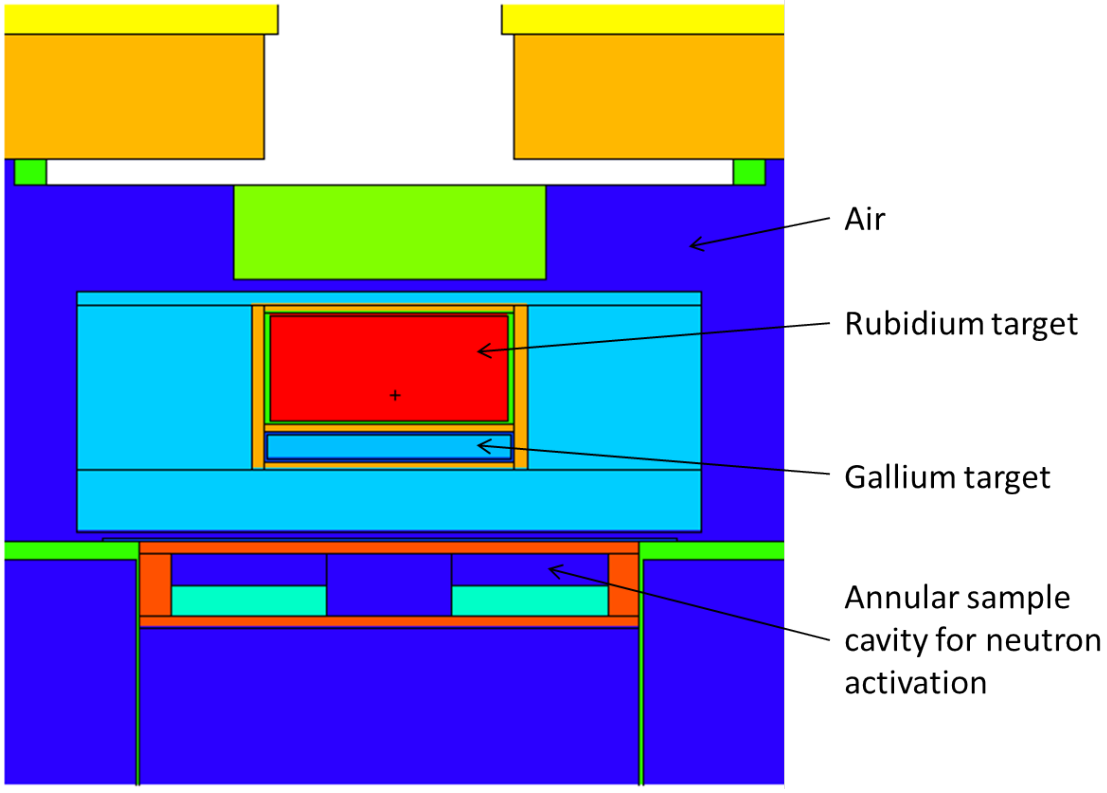


Figure 3.3: The VBTS geometry as generated with the MCNP visual editor. This view zooms in further to show the details of the tandem targets and activation chamber.

simulations were performed with beam diameters of 16, 24, 30 and 36 mm. Runs were also performed with a more realistic beam profile, namely a Gaussian beam displaced from the beam axis in both the x and y directions (where the z-axis is the beam axis), truncated with a so-called "Cooky Cutter Cell" (CCC) to cut off the tails of the Gaussian when they reach the radius of the collimator aperture. The parameters of the Gaussian function, namely the *full-width at half maximum* (FWHM) and the position of the centroid, were derived from a measured VBTS beam intensity profile obtained by means of an autoradiogram. Figure 3.4 shows an example of an analysis performed with the software package DoseLab [DEM2000] on an autoradiogram made on radiochromic film. The values plotted as a histogram were generated by the software, based on the amount of darkening of the film relative to an unexposed film, scans of which were imported into the code as JPEG files. The exposed film was not put directly into the beam. Instead, a flat activated aluminium foil was placed on the film for several minutes after bombardment. This caused the entire film to get some exposure, leading to the non-zero background. There is also a slight asymmetry in the histogram that is not well understood. Nevertheless, the intensity profile of the beam is reproduced satisfactorily by the Gaussian described above, generated with a FWHM of 7.5 mm and centroid at 9 mm relative to the beam axis. This Gaussian approximation is therefore judged to be realistic.

The total number of incident protons was 200 million per run. Such a run takes about one week to complete on a high-end Core-i7 computer. The neutrons traversing the activation

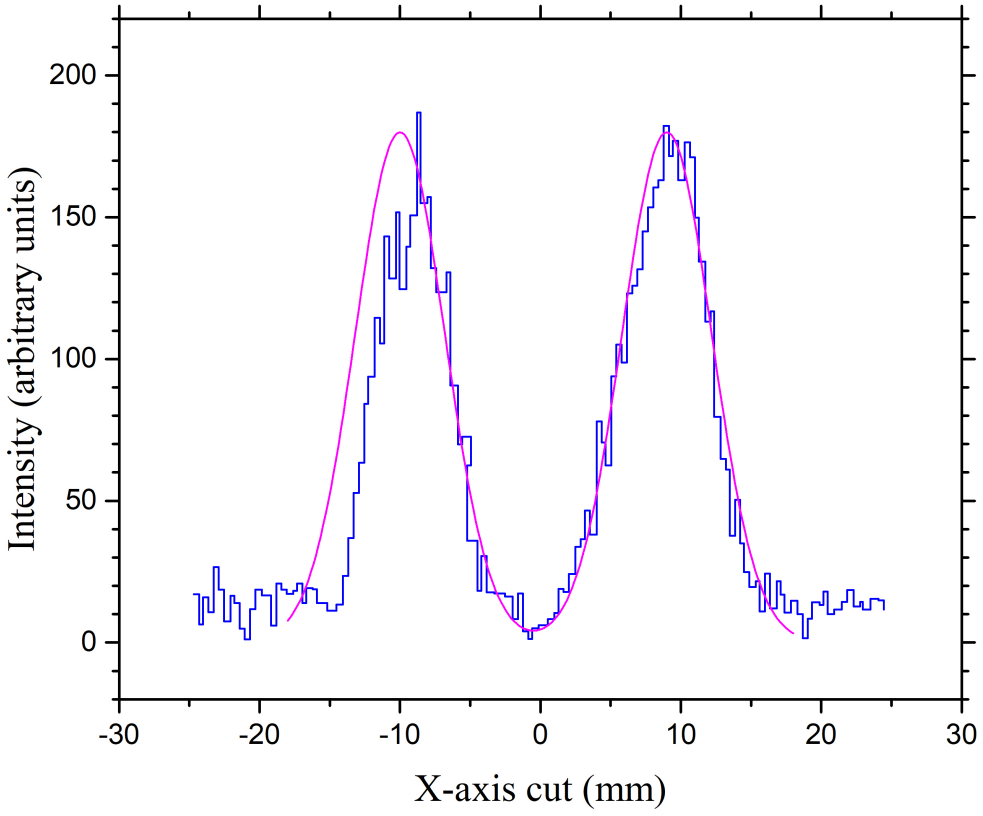


Figure 3.4: Beam profile on target in the VBTS (blue histogram) obtained from an autoradiogram analyzed with the DoseLab software (see text). The curve is a cut through a rotating Gaussian, offset relative to the beam axis and truncated at a radius of 18 mm. The Gaussian FWHM is 7.5 mm and the centroid offset is 9 mm. Two orthogonal dipole magnets provided a circular sweep at a frequency of 3 kHz when the autoradiogram was taken.

chamber were tallied in 117 energy bins/groups, covering the range from thermal to near-beam energies. This energy-group structure will be discussed in more detail in Chapter 4. The output generated using an F4 tally provided the neutron flux in each energy group (neutrons/cm^2 per incident proton) as well as the associated fractional standard deviation (FSD, also referred to as the relative error) in that energy group. With 2×10^8 particle histories, the majority of groups had less than 1% standard deviations, however, towards the highest and lowest energies the statistics were poorer. Fortunately, groups with fewer neutrons (and thus greater uncertainties) would most often contribute less to the activation yield, therefore also limiting their contribution to the total uncertainty.

The results from the beam-spot size investigation are summarized in Table 3.1. The neutron fluxes obtained with uniform beam intensities and various spot sizes are compared to the Gaussian beam results by presenting their respective ratios, summed into broad energy regions. It is evident that the majority of ratios are close to unity, indicating that there is not a large sensitivity to the choice of beam profile. Note that the results of Table 3.1 have been obtained from five individual MCNP runs using the CEM physics selection.

Table 3.1: Test of beam-spot size: Ratios of neutron fluxes in broad energy regions.

Energy region (MeV)	$\frac{\Phi(16\text{ mm})}{\Phi(\text{Gauss})}$	$\frac{\Phi(24\text{ mm})}{\Phi(\text{Gauss})}$	$\frac{\Phi(30\text{ mm})}{\Phi(\text{Gauss})}$	$\frac{\Phi(36\text{ mm})}{\Phi(\text{Gauss})}$
$E < 0.1$	1.03 ± 0.08	1.05 ± 0.08	1.03 ± 0.08	1.03 ± 0.08
$0.1 \leq E < 10$	1.03 ± 0.02	1.03 ± 0.02	1.02 ± 0.02	1.01 ± 0.02
$10 \leq E < 20$	1.03 ± 0.04	1.03 ± 0.04	1.02 ± 0.04	1.00 ± 0.04
$20 \leq E < 30$	1.04 ± 0.05	1.02 ± 0.05	1.01 ± 0.05	0.98 ± 0.05
$30 \leq E < 40$	1.05 ± 0.06	1.03 ± 0.06	1.02 ± 0.06	1.00 ± 0.06
$40 \leq E < 50$	1.02 ± 0.07	1.01 ± 0.07	1.01 ± 0.07	0.99 ± 0.07
$E \geq 50$	1.05 ± 0.16	1.05 ± 0.16	1.04 ± 0.16	1.01 ± 0.16

3.5 NEUTRON SPECTRA

Each physics model selection employed in MCNP provided a neutron spectrum. The different physics selections provided similar spectra, but not identical. The neutron spectrum obtained from the CEM physics selection is shown in Fig. 3.5. With a logarithmic scale on the y-axis, the spectra from all the physics selections were found to look very similar, therefore only one of them is shown here as an example. The maximum beam intensity for 66 MeV protons currently employed in the VBTS is 250 μA, therefore it gives valuable insight to plot the cumulative neutron yield for that intensity, shown in Fig. 3.6. As can be seen from the figure, the total flux is close to 1.0×10^{12} neutrons per cm^2 under such bombardment conditions. About 52% of the neutrons have energies above 1 MeV.

To compare the neutron spectra obtained from the six different physics selections used in the simulations, the relative standard deviation was calculated for each of the 117 energy groups, presented as a histogram in Fig. 3.7. (The relative standard deviation is the standard

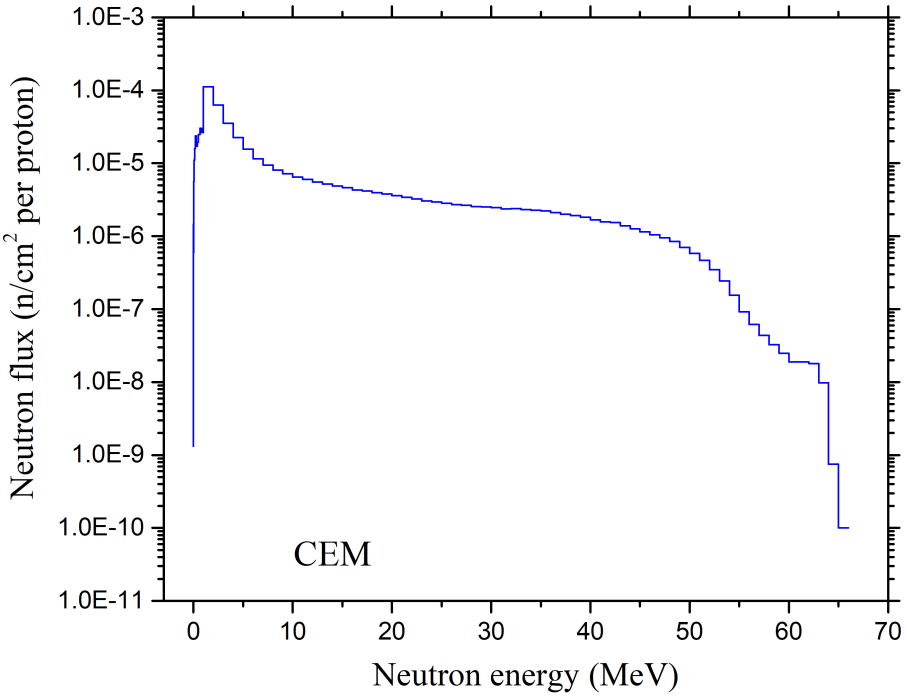


Figure 3.5: Neutron flux (neutrons/cm^2 per proton) versus neutron energy in the activation chamber, as obtained from the Cascade-Exciton Model (CEM) physics selection in MCNP 6.1 with the number of particle histories set at 2×10^8.

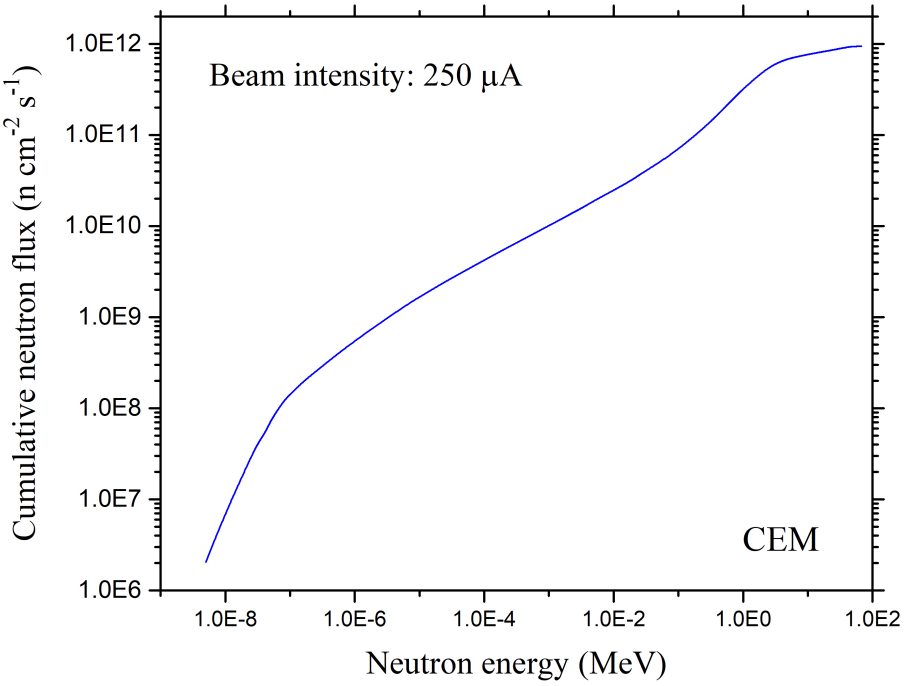


Figure 3.6: Cumulative neutron flux (neutrons cm^{-2} s^{-1}) versus neutron energy in the activation chamber for a proton beam intensity of 250 μA, obtained from the CEM physics selection in MCNP 6.1 with 2×10^8 particle histories.

deviation of a set of values divided by their corresponding average, expressed as a percentage in Fig. 3.7). It is evident that the differences between the resulting neutron fluxes are quite significant for some groups, however, exceeding 30% only for a few groups. Those latter groups are mostly located at the extremities of the spectra.

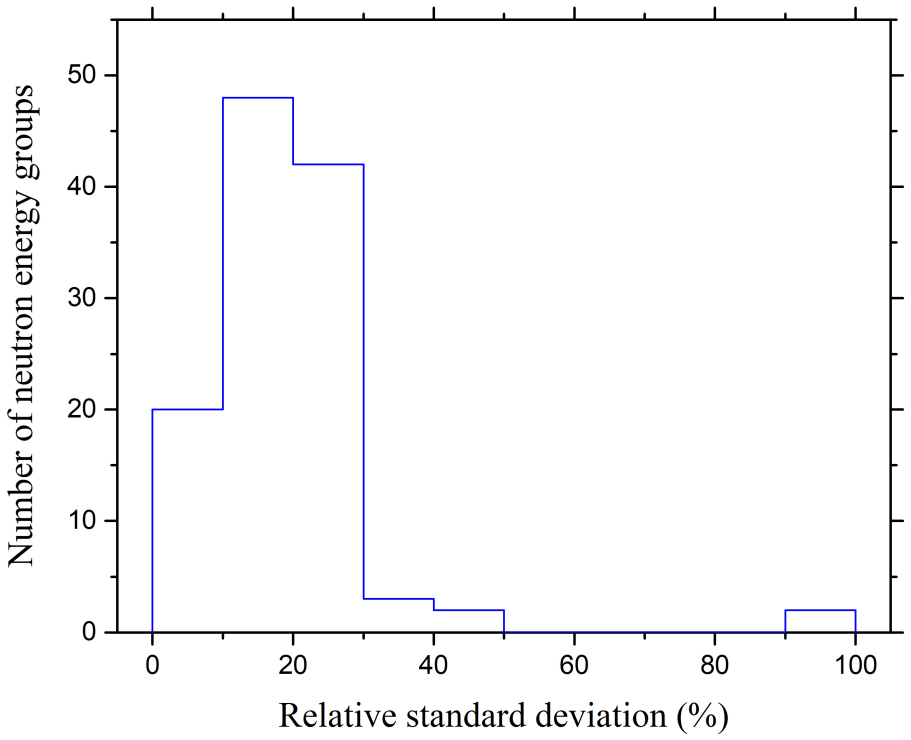


Figure 3.7: Number of neutron energy groups versus the relative standard deviation for all 117 neutron groups obtained from all six physics selections employed in the MCNP 6.1 simulations.

In some calculations, which will be presented in Chapter 4, an average neutron spectrum was employed and the standard deviations of the fluxes in the various groups treated as an uncertainty. These latter values are clearly significantly larger than the uncertainties associated with a possible variation is beam-spot size, which is evident when comparing the values of Table 3.1 with the results from the simulations shown in Fig. 3.7.

To conclude, it was found that the neutron spectra in the region of the activation chamber are rather insensitive to the particular choice of the beam profile. This is reassuring as the experimental beam profile cannot be known exactly and can also vary with time (e.g. due to beam instabilities and/or changing focus conditions during the course of the bombardment), thus we cannot model it precisely in the Monte Carlo simulations. The numerical values of the neutron spectra generated with MCNP have been incorporated into the input data files used in the further analysis activities of this study. These data are ingredients required to make predictions of the physical yields for all the radionuclides observed in this study. The data analysis is discussed in the next chapter.

Chapter 4

Data Analysis

In this chapter, we focus on the procedures which were followed in the analysis of the data, obtained both from measurements and Monte Carlo simulations, in order to produce two sets of results for direct comparison. The first set comprises the experimental physical yields of the neutron-induced activation products in the samples and the second set the corresponding predictions.

4.1 PREDICTED YIELDS

One of the primary objectives of this study is to compare measured physical yields with calculated predictions for a selection of residues formed by neutron-induced reactions, covering a wide range of target nucleus mass. There are various ways to approach this, especially where the calculated predictions are concerned. Ultimately, a particular approach was adopted in this work, a choice amongst several available options, discussed in detail in the paragraphs below. Two basic ingredients are required to calculate physical yields, namely (1) the neutron flux in the location where the samples are activated, and (2) cross sections for the formation of the residues by the relevant neutron-induced reactions. In this study, the neutron flux was obtained from a Monte Carlo simulation (MCNP) and cross sections were taken from the well-known TALYS Evaluated Nuclear Data Library (TENDL) [ROC2017]. Although several processing codes are available, we chose to do the processing with a FORTRAN code that we developed ourselves.

The only feasible way to obtain a full-energy spectrum of emitted neutrons in this kind of study is by means of a Monte Carlo simulation in which the bombardment facility (in this case the VBTS), beam and target are modelled with a significant level of precision. Several well-known Monte Carlo radiation transport codes are available that can in principle be used for this purpose, e.g. FLUKA (see Böhlen et al. [BÖH2014]), Geant (see Allison et al. [ALL2016]), MCNP (see e.g. Konobeyev et al. [KON2011], Goorley et al. [GOO2013], Pelowitz et al. [PEL2013]), etc. The code MCNP 6.1 [GOO2013] was eventually chosen for a number of reasons, as discussed below. Firstly, its main developers are working at the Los Alamos National Laboratory (LANL) where the Los Alamos Neutron Science Center (LANSCE) is located. Thus, MCNP is being developed to support a broad base of neutron research, in addition to many other applications. Secondly, the linac that serves LANSCE with proton beams for its neutron generation also

supplies proton beams of 100 MeV to the Isotope Production Facility (IPF) of LANL. Recent experimental work at the IPF investigated the possibility to utilize the neutron flux directly behind a production target to produce useful radionuclides in a commensalistic mode (see e.g. [ENG2014, MOS2016] and references therein). These last-mentioned studies, which to a large extent prompted the present investigation, likewise made use of MCNP simulations to obtain the neutron spectrum at the locations where the samples were activated.

Cross sections of neutron-induced reactions can be obtained from a number of sources. They can, in principle, be provided by the physics models implemented in MCNP. Measured cross sections are available but only up to about 20 MeV for many reactions. There are also evaluated data for some reactions in so-called ENDF format, but again mostly limited to energies up to about 20 MeV. Towards higher energies, experimental values are very scarce. In this work, cross sections for production of residual nuclides were taken from the TENDL-2015 and TENDL-2017 libraries [ROC2017]. TENDL (an acronym for "TALYS-based evaluated nuclear data library") provides the output of the TALYS nuclear model code system for direct use in both basic physics and applications. The 8^{th} version of the library is TENDL-2015, which is based on both default and adjusted TALYS calculations as well as data from other sources. (Previous releases were in 2008, 2009, 2010, 2011, 2012, 2013 and 2014). TENDL-2015 was released on 18 January 2016 and last updated on 5 October 2016. This was the latest version available at the time when this work commenced. Our analysis was already in an advanced stage when the 9^{th} version, TENDL-2017, was released for general use on 30 December 2017. A full analysis has therefore been performed with both TENDL-2015 and TENDL-2017 data, leading to two sets of results, which in their own right are interesting to compare. The details will be discussed later.

The TENDL data are pointwise data. The neutron flux data obtained from an MCNP 6.1 simulation have been binned in discrete energy groups, which will be explained below. To calculate physical yields, "groupwise" cross sections first have to be determined from the pointwise data, meaning that the cross section, which in general is a variable function of energy, is treated as a constant within any particular energy group.

4.1.1 Energy-group structure

Neutrons in different energy regions exhibit different fluxes, thus it would be wrong to assign the same neutron flux to the entire neutron energy range as that would lead to large errors. Since the energy spectrum of neutrons is continuous, the relevant energy range had to be binned (partitioned) into several smaller energy regions (normally referred to as energy groups), such that the assumption of a constant flux in each energy group would be justified as an acceptable approximation. A choice had to be made amongst the many energy-group structures in general use in Monte Carlo simulations. The so-called LaBauve energy-group structure was adopted in this study, similar to the approach by DeLorme [DEL2014], however, this particular scheme only extends from thermal energies up to 25 MeV. To make provision for tallying neutrons with energies above 25 MeV, it was necessary to extend this energy-group structure to higher energies, as discussed below.

Briefly, the LaBauve energy-group structure is a 63-group structure ranging from 10^{-11} MeV

to 25 MeV, defined by LaBauve for the CINDER'90 code [WIL1993]. Initially developed for activation and burn-up calculations in reactor problems, a later version, CINDER2008, is also suitable for accelerator problems but only up to 20 MeV. Whereas CINDER'90 uses 63 neutron groups up to 25 MeV, CINDER2008 has three reaction libraries, containing a 66-group structure up to 25 MeV, a 321-group flat-weighted structure (based on the 315-group TRIPOLI group structure) and a 175-group fusion-weighted library in the VITAMIN-J group structure. Both the TRIPOLI and VITAMIN-J group structures, which we initially considered, range from 10^{-11} MeV to 20 MeV, thus, like the unmodified LaBauve structure, would have required an extension to higher energies. Finally, it seemed prudent to modify the LaBauve energy-group structure to contain groups up to 67 MeV. The 66-group fission-weighted library of CINDER2008 actually uses the same group structure as the 63-group LaBauve structure except that the lowest group ($E_n < 10^{-9}$ MeV) has been subdivided into 4 groups. This is reassuring as it indicates that the LaBauve structure is not outdated but still relevant.

A modified LaBauve energy-group structure was therefore adopted in this work to tally the neutron flux obtained from the Monte Carlo simulations with the code MCNP 6.1. All the LaBauve groups below 1 MeV were adopted unchanged. The energy group that crosses 1 MeV was truncated at an upper value of 1 MeV. Towards higher energies, all the groups had a constant bin size of 1 MeV in width. The energy-group structure was terminated at 67 MeV. With this approach, one obtains a total of 117 neutron groups, 51 of them below 1 MeV (see Table 4.1).

In this work, we were primarily interested in the threshold reactions, i.e. where particles are emitted by the nucleus after the interaction. These thresholds are almost always above 1 MeV, where the energy groups adopted have a constant width of 1 MeV. The LaBauve energy groups below 1 MeV are mostly needed for the (n,γ) capture reactions, which were also analyzed for the sake of interest.

4.1.2 Pointwise and group-averaged cross sections

As already mentioned, the residue production cross sections were taken from the TENDL-2015 and TENDL-2017 libraries. These pointwise data tables were downloaded as ASCII (text) files for all the relevant reactions. In most cases, the number of TENDL data points are rather few, enough to represent the shape of the excitation function but requiring non-linear interpolation to find the cross-section values at in-between domain points. For this purpose we used cubic spline interpolation, adopting the natural cubic spline routines of the well-known compilation "Numerical Recipes in Fortran 77" [PRE1997]. This mostly worked fine except in a number of cases where noticeable oscillations were observed between sample points, a phenomenon sometimes referred to as Runge's phenomenon. A solution was found by enlarging the pointwise data sets by means of spline filters. These enlarged pointwise data files were then used in the analysis instead of the original TENDL files. The procedure was as follows:

The commercial "curve fitting and equation discovery" package TableCurve 2D [TAB2018] was used to increase the number of representative points of the TENDL excitation functions for the relevant neutron-induced reactions. Each TENDL data file was imported into TableCurve and automatically plotted on screen by the software. The "Digital Spline Filter" option was

Table 4.1: Group boundaries (bins) of the Modified LaBauve neutron multigroup structure.

Gr no	Lower limit (MeV)	Upper limit (MeV)	Gr no	Lower limit (MeV)	Upper limit (MeV)	Gr no	Lower limit (MeV)	Upper limit (MeV)
1	1.000E-11	5.000E-09	40	1.505E-02	1.997E-02	79	2.800E+01	2.900E+01
2	5.000E-09	1.000E-08	41	1.997E-02	2.526E-02	80	2.900E+01	3.000E+01
3	1.000E-08	1.500E-08	42	2.526E-02	4.087E-02	81	3.000E+01	3.100E+01
4	1.500E-08	2.000E-08	43	4.087E-02	6.738E-02	82	3.100E+01	3.200E+01
5	2.000E-08	2.500E-08	44	6.738E-02	1.111E-01	83	3.200E+01	3.300E+01
6	2.500E-08	3.000E-08	45	1.111E-01	1.832E-01	84	3.300E+01	3.400E+01
7	3.000E-08	3.500E-08	46	1.832E-01	3.020E-01	85	3.400E+01	3.500E+01
8	3.500E-08	4.200E-08	47	3.020E-01	3.887E-01	86	3.500E+01	3.600E+01
9	4.200E-08	5.000E-08	48	3.887E-01	4.979E-01	87	3.600E+01	3.700E+01
10	5.000E-08	5.800E-08	49	4.979E-01	6.393E-01	88	3.700E+01	3.800E+01
11	5.800E-08	6.700E-08	50	6.393E-01	8.209E-01	89	3.800E+01	3.900E+01
12	6.700E-08	8.000E-08	51	8.209E-01	1.000E+00	90	3.900E+01	4.000E+01
13	8.000E-08	1.000E-07	52	1.000E+00	2.000E+00	91	4.000E+01	4.100E+01
14	1.000E-07	1.520E-07	53	2.000E+00	3.000E+00	92	4.100E+01	4.200E+01
15	1.520E-07	2.510E-07	54	3.000E+00	4.000E+00	93	4.200E+01	4.300E+01
16	2.510E-07	4.140E-07	55	4.000E+00	5.000E+00	94	4.300E+01	4.400E+01
17	4.140E-07	6.830E-07	56	5.000E+00	6.000E+00	95	4.400E+01	4.500E+01
18	6.830E-07	1.125E-06	57	6.000E+00	7.000E+00	96	4.500E+01	4.600E+01
19	1.125E-06	1.855E-06	58	7.000E+00	8.000E+00	97	4.600E+01	4.700E+01
20	1.855E-06	3.059E-06	59	8.000E+00	9.000E+00	98	4.700E+01	4.800E+01
21	3.059E-06	5.043E-06	60	9.000E+00	1.000E+01	99	4.800E+01	4.900E+01
22	5.043E-06	8.315E-06	61	1.000E+01	1.100E+01	100	4.900E+01	5.000E+01
23	8.315E-06	1.371E-05	62	1.100E+01	1.200E+01	101	5.000E+01	5.100E+01
24	1.371E-05	2.260E-05	63	1.200E+01	1.300E+01	102	5.100E+01	5.200E+01
25	2.260E-05	3.727E-05	64	1.300E+01	1.400E+01	103	5.200E+01	5.300E+01
26	3.727E-05	6.144E-05	65	1.400E+01	1.500E+01	104	5.300E+01	5.400E+01
27	6.144E-05	1.013E-04	66	1.500E+01	1.600E+01	105	5.400E+01	5.500E+01
28	1.013E-04	1.670E-04	67	1.600E+01	1.700E+01	106	5.500E+01	5.600E+01
29	1.670E-04	2.754E-04	68	1.700E+01	1.800E+01	107	5.600E+01	5.700E+01
30	2.754E-04	4.540E-04	69	1.800E+01	1.900E+01	108	5.700E+01	5.800E+01
31	4.540E-04	7.485E-04	70	1.900E+01	2.000E+01	109	5.800E+01	5.900E+01
32	7.485E-04	1.234E-03	71	2.000E+01	2.100E+01	110	5.900E+01	6.000E+01
33	1.234E-03	2.035E-03	72	2.100E+01	2.200E+01	111	6.000E+01	6.100E+01
34	2.035E-03	2.404E-03	73	2.200E+01	2.300E+01	112	6.100E+01	6.200E+01
35	2.404E-03	2.840E-03	74	2.300E+01	2.400E+01	113	6.200E+01	6.300E+01
36	2.840E-03	3.338E-03	75	2.400E+01	2.500E+01	114	6.300E+01	6.400E+01
37	3.338E-03	5.603E-03	76	2.500E+01	2.600E+01	115	6.400E+01	6.500E+01
38	5.603E-03	9.403E-03	77	2.600E+01	2.700E+01	116	6.500E+01	6.600E+01
39	9.403E-03	1.505E-02	78	2.700E+01	2.800E+01	117	6.600E+01	6.700E+01

subsequently used to obtain a smooth curve through the supplied TENDL points, also with on-screen visualization. An output file was then generated containing more points, at least a ten-fold increase to the original TENDL data. The user can choose between a B-spline of order 2 or a NURBS spline with order ranging from 2 to 8 (explained below). In this way one could always find a smooth curve, with the "human eye" a magnificent tool to judge the goodness of fit. The procedure also provided the opportunity to visually inspect every excitation function used in the analysis. The term "B-spline" is short for "basis spline" and is a piecewise polynomial function of degree $n-1$ in the independent variable for a spline function of order n [GOS1990]. NURBS

splines are a specific class of B-splines, the so-called "non-uniform rational basis splines". With TableCurve one can rapidly adjust points in order to improve the fit, however, this was never found to be necessary as the TENDL data are already quite smooth. TableCurve is a highly evolved and intuitive code that offers a very rapid workflow. The most recent version is 5.01 but for this work version 4.0 was used.

There are two basic approaches to using cross sections in calculations, namely "continuous" and "multigroup" [HOD2015]. Where Monte Carlo methods are involved, the latter comes into play as the tallying of emitted particles (in this case neutrons) requires energy intervals or groups. Consequently, cross-section values are required in which the pointwise data have been averaged over these energy groups (so-called "group-averaged cross sections" or "multigroup cross sections"). Multigroup cross sections can be expressed as follows:

$$\sigma_i = \frac{1}{\phi_i} \int_{E_i}^{E_{i+1}} \phi(E)\sigma(E)dE; \quad 1 \leq i \leq N_g, \tag{4.1}$$

where $\phi(E)$ is a weighting function, $\sigma(E)$ is the excitation function (cross-section function) and N_g is the number of discrete energy groups. The integration limits are the boundaries of the group. The quantity ϕ_i is the weighing function integrated over the group:

$$\phi_i = \int_{E_i}^{E_{i+1}} \phi(E)dE. \tag{4.2}$$

Ideally, the weighting function should be the flux of the particles causing the activation but this is not always *inter alia* known within the boundaries of individual groups. (If it was, the Monte Carlo simulations would not have been required.) Prior knowledge of the flux in particular applications and energy regions is often used to establish approximate weighting functions, e.g. flat, $1/E$, Maxwellian thermal, fission spectrum, or velocity exponential fusion. The variation within a single group of the functions $\phi(E)$ and $\sigma(E)$ – relevant to the integrand of Eq. (4.1) – will normally decrease if the total number of groups is increased, reducing the dependence on the weighting. This approach, however, will always be computationally more expensive. Usually in this regard a compromise must be made. Processing codes such as NJOY [MAC2012] are available to produce multigroup cross sections from pointwise cross sections. As already mentioned, we decided not to use an existing processing code but to write our own code.

In the current analysis, we have not attempted to derive multigroup cross sections by means of the above approach, accepting that we might have to do so later (e.g. by performing long Monte Carlo runs with tallying in very narrow energy bins in order to obtain realistic weighting functions for use on a broader group structure). Instead, we used different averaging of the cross section within each group according to the so-called closed-form Newton-Cotes formulae, which will be discussed next. The rationale is that sensitivity to the group structure should be shown by varying the degree of the Newton-Cotes formula. In addition, minima and maxima were determined for the cross section in each group, from which upper and lower limits of the physical yield could be calculated. This information should be sufficient to decide whether (or not) a bigger effort would be required to establish more accurate multigroup cross sections.

4.1.3 The mean formation cross section

One of the ingredients required to calculate the physical yield of an activation product in a sample is the mean formation cross section. This quantity is a weighted averaged of the cross sections in the individual energy groups.

Let Φ_t denote the total neutron flux (neutons/cm^2 per incident proton) in the inner cavity of the activation chamber, as given by the MCNP 6.1 simulation. Let N_g denote the number of neutron groups of the adopted energy-group structure. The following identity then holds:

$$\frac{1}{\Phi_t}\sum_{i=1}^{N_g}\phi_i = 1, \tag{4.3}$$

where ϕ_i is the neutron flux in neutron group i; $1 \leq i \leq N_g$. One can interpret the ratio ϕ_i/Φ_t as the probability that a randomly observed neutron inside the activation cavity belongs to energy-group i. The mean cross section for the formation of a particular radionuclide by neutron activation can be defined as follows:

$$\overline{\sigma}_n = \frac{1}{\Phi_t}\sum_{i=1}^{N_g}\phi_i\sigma_i, \tag{4.4}$$

where σ_i is the formation cross section pertaining to neutron group i, henceforth referred to as the "group cross section". In general, the cross section is a function of the neutron energy, referred to as the *excitation function*. Its value varies continuously over the energy interval of a neutron group. The constant "group cross section" adopted for each neutron group should therefore be evaluated with some care as the variation of the excitation function within a single group may not be negligible. Instead of determining so-called "group-averaged cross sections", in this study the closed-form Newton-Cotes formulae were adopted in order to establish whether there was sensitivity to the discretization of the cross section (which may happen if there is a large variation of the excitation function within a single energy group). This scheme is explained below.

Let a and b denote the lower and higher group boundaries of an arbitrary chosen neutron group, as shown in Fig. 4.1. Let E_j define a set of equispaced neutron energies within the region $a \rightarrow b$ as follows:

$$E_j = a + j(b-a)/n; \quad 0 \leq j \leq n, \tag{4.5}$$

where n is referred to as the "degree" of the scheme. For each neutron group i, the group cross section can be evaluated by applying the closed-form Newton-Cotes formulae of different degrees, as summarized in Table 4.2. In addition, calculations were also performed by adopting for σ_i the cross section at the middle of a neutron group, i.e. the mid value $\sigma_i = \sigma([b+a]/2])$, as well as adopting the minimum and maximum cross sections from the interpolations in each group. In cases where the high-energy part of the neutron spectrum is responsible for the bulk of the yield (e.g. where the excitation function has a threshold above 1 MeV) the various forms for the group cross section in Table 4.2 are not expected to show much difference. In cases where the thermal and epithermal neutrons dominate the production yield (e.g. for capture reactions) the variation can be expected to be larger. This is because the width of the neutron groups become large relative to the energy scale applicable to those groups and the shape of

the excitation function within some of those groups can be complex (e.g. the resonance region) or be a strong function of energy (e.g. the $1/E$ thermal region).

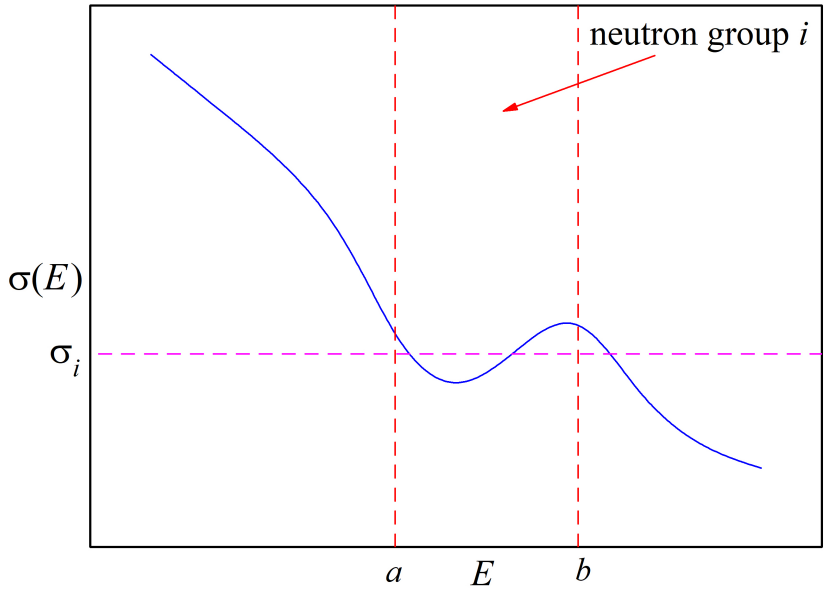


Figure 4.1: Illustration of a neutron group defined on an excitation function (i.e. cross section $\sigma(E)$ versus neutron energy E) to discretize the cross section in that group (energy bin). The variables introduced are also used in the equations listed in Table 4.2.

Table 4.2: The group cross section according to closed-form Newton-Cotes formulae as well as group mid value, minimum and maximum.

Degree	Formula used for σ_i	Common name
1	$\frac{b-a}{2}[\sigma(E_0)+\sigma(E_1)]$	Trapezoid rule
2	$\frac{b-a}{6}[\sigma(E_0)+4\sigma(E_1)+\sigma(E_2)]$	Simpson's rule
3	$\frac{b-a}{8}[\sigma(E_0)+3\sigma(E_1)+3\sigma(E_2)+\sigma(E_3)]$	Simpson's 3/8 rule
4	$\frac{b-a}{90}[7\sigma(E_0)+32\sigma(E_1)+12\sigma(E_2)+32\sigma(E_3)+7\sigma(E_4)]$	Boole's rule
—	$\sigma([b+a]/2])$	Mid value in group
—	$\min[\sigma(E_0),\sigma(E_1),\sigma(E_2),\sigma(E_3),\sigma(E_4)]$	Minimum
—	$\max[\sigma(E_0),\sigma(E_1),\sigma(E_2),\sigma(E_3),\sigma(E_4)]$	Maximum

4.1.4 Accumulated charge

As the experimental yield results have been normalized to the unit of charge μAh, one would like to do the same for the predictions based on the MCNP 6.1 neutron spectra in conjunction with excitation functions from the TENDL libraries. From the simulations, one obtains the neutron flux per incident proton. Consequently, one needs to calculate the number of incident

protons in an accumulated charge of 1 μAh. One proton has a charge of 1.602×10^{-19} C/s. Therefore 6.242×10^{18} protons have a combined charge of 1 C. We also have the following equivalence of units: 1 μAh $\equiv 3.6 \times 10^{-3}$ C. Thus 1 μAh contains 2.247×10^{16} protons, a number that will be denoted Q_p in the subsequent discussion.

4.1.5 Physical yield

The physical yield per unit mass of the sample, or more precisely per unit mass of the fraction of target nuclei of the same isotope in the sample, is given by

$$Y = \Phi_t Q_p \left(\frac{N_A}{A}\right) \lambda \overline{\sigma}_n (1 \times 10^{-27}) \qquad \text{Bq}\,(\mu\text{Ah})^{-1}\,\text{g}^{-1}, \tag{4.6}$$

where N_A is Avogadro's number, A is the atomic mass of the target nuclei in atomic mass units (AMU), λ is the decay constant of the produced radionuclide, and it is assumed that the mean formation cross section has units of millibarn. In cases where the target has a natural composition containing more than one isotope, Eq. (4.6) can be successively applied to each target isotope, weighted with its natural abundance and summed.

4.2 EXPERIMENTAL YIELDS

Measured yields are typically stated for a specific reference time, which is often taken as the end of bombardment (EOB). This is different in the case of the so-called "physical yield". This derived quantity, also called the "instantaneous yield" or "make rate", is independent of the bombardment history as it factors out all decay losses. An expression for this quantity is derived below.

Let the bombardment period be denoted by T_1. The following times are defined:

$t = 0$:	Start of bombardment (SOB),
ΔT :	Time increment of logged beam current integrator values (60 s),
n :	Total number of incremental time intervals in bombardment period,
$t = T_1 = n\Delta T$:	End of bombardment (EOB).

Note that the current integrator values were logged in 1 s intervals but were summed to 1 min intervals for the purposes of the analysis. This was done simply to reduce the number of computations and to reduce the size of the "bombardment history file". The end of each time interval is given by

$$t_i = i\Delta T \qquad \text{for all} \quad 1 \leq i \leq n. \tag{4.7}$$

The start and stop times of the counting system are defined as follows:

$t = T_2$:	Start of counting period,
$t = T_3$:	End of counting period.

The decay time between the EOB and start of counting is $(T_2 - T_1)$ and the real time of counting is $(T_3 - T_2)$. The real time of counting is also given by the sum of the counting live time (τ) and dead time ($\Delta\tau$), thus

$$\tau = (T_3 - T_2) - \Delta\tau. \tag{4.8}$$

Let ΔQ_i be the charge collected during bombardment interval i in units of μAh. Let the activity formed in time interval i be denoted by ΔA_i. Its contribution to the total activity at EOB is given by $\Delta A_i \exp(-\lambda[T_1 - t_i])$. The total activity at EOB is therefore given by

$$A(T_1) = \sum_{i=1}^{n} \Delta A_i \exp(-\lambda[T_1 - t_i]). \tag{4.9}$$

The incremental activity ΔA_i is directly proportional to the charge accumulated in time interval i, thus

$$A(T_1) = R \sum_{i=1}^{n} \Delta Q_i \exp(-\lambda[T_1 - t_i]), \tag{4.10}$$

where R is a proportionality constant that has a physical significance, namely it is the "physical yield", which has units of Bq/μAh in this work. The main aim is to determine this quantity, R, experimentally. Let t_m be the time within the counting period where the instantaneous activity equals the average activity over the entire counting period. Then

$$\begin{aligned} A(T_2)\exp(-\lambda T_m) &= \frac{1}{(T_3 - T_2)} \int_{T_2}^{T_3} A(t)dt \\ &= \frac{1}{(T_3 - T_2)} A(T_2) \int_{T_2}^{T_3} \exp(-\lambda t)dt. \end{aligned} \tag{4.11}$$

After integration and taking the natural logarithm on both sides of the equal sign, one finally gets an equation for T_m:

$$T_m = -\frac{1}{\lambda} \ln \left[\frac{\exp(-\lambda T_2) - \exp(-\lambda T_3)}{-\lambda(T_2 - T_3)} \right]. \tag{4.12}$$

The activity at time $t = T_m$ is given by

$$A(T_m) = \frac{A_p}{\tau \epsilon_\gamma \epsilon_d}, \tag{4.13}$$

where A_p is the area of the full-energy peak of a characteristic γ-ray, ϵ_γ is the branching ratio (intensity) of this γ-ray, and ϵ_d is the detector efficiency at this photon energy. Next, one can apply this expression to obtain the activity at EOB:

$$A(T_1) = \frac{A_p}{\tau \epsilon_\gamma \epsilon_d} \exp(\lambda[T_m - T_1]). \tag{4.14}$$

Equations (4.10) and (4.14) both give the activity at EOB, thus one can substitute Eq. (4.10) into Eq. (4.14) and solve for the quantity R:

$$R = \frac{A_p \exp(\lambda[T_m - T_1])}{\tau \epsilon_\gamma \epsilon_d \sum_{i=1}^{n} \Delta Q_i \exp(-\lambda[T_1 - t_i])}. \tag{4.15}$$

As already mentioned, the physical yield, R, has units of Bq/μAh in this work. However, it is convenient to take into account the size of the sample. Let M be the mass of the sample. The physical yield per unit mass is given by

$$Y = R/M = \frac{A_p \exp(\lambda[T_m - T_1])}{M \tau \epsilon_\gamma \epsilon_d \sum_{i=1}^{n} \Delta Q_i \exp(-\lambda[T_1 - t_i])} \quad \text{Bq}\,(\mu\text{Ah})^{-1}\,\text{g}^{-1}. \tag{4.16}$$

Similar to Eq. (4.6), in cases where the target has a natural composition containing more than one isotope, Eq. (4.16) can likewise be successively applied to each target isotope, weighted with its natural abundance and summed.

4.3 COMPARISON BETWEEN CALCULATED AND EXPERIMENTAL YIELDS

Physical yields of relatively long-lived radionuclides have been derived both by calculations based on physical models (discussed in section 3.2) as well as from experimental measurements, for more than 100 reactions or nuclear processes. These cover a wide range of atomic and mass numbers (Z ranging from 4 to 83 and A ranging from 7 to 208). The question is how to display such a large set of results in a way that gives a visual insight of the overall level of agreement between the calculated and measured values. First, we established a unique index or "reaction identification number" for each case. This numbering scheme runs in order of increasing Z as the first condition, followed by increasing A as a second condition. This index can be displayed on, say, the x-axis of a graph in order to show the trend of a quantity as a function of increasing atomic charge and mass. We produced several types of plots in this way, where the quantity on the y-axis is related to both the calculated and experimental physical yields. While this is conceptually simple, it took us a while to find the best approach.

Let i denote the reaction identification (ID) number, Y_{CALC} the calculated physical yield and Y_{EXP} the measured physical yield. As a first attempt, we plotted the ratio of the yields versus the reaction ID number, which can be expressed formally as follows:

$$H_0(Y_{CALC}(i), Y_{EXP}(i)) = \frac{Y_{CALC}(i)}{Y_{EXP}(i)}; \quad 1 \leq i \leq N_r, \tag{4.17}$$

where N_r is the total number of reactions for which physical yields could be extracted in the analysis. The reason for this particular notation will become apparent soon.

It was quickly realized that plots made by means of Eq. (4.17) were not particularly useful, the reason being that the "ratio" as a function of two positive numbers as its arguments is extremely asymmetric. The value of such a ratio would always be compressed between 0 and 1 when the numerator is smaller than the denominator and unconstrained when the numerator is larger than the denominator. It became clear that the differences between calculated and experimental values must be used in a way that is symmetrical. Thus, we had to learn how statisticians and economists handle such differences (or changes) in similar problems. Unfortunately, there are several approaches in which this is done and the resulting quantities, while simple in formalism, are not always self explanatory. Finally, we found an article by Törnqvist et al. [TOR1985] that provided the insight required. It is useful to develop this topic more formally before discussing the approach adopted in this study.

4.3.1 Indicators of relative difference

Unlike absolute difference, which is a simple substraction of one value from another, relative difference takes into account the magnitudes of the quantities being compared.

Let x and y denote two positive quantities determined on the same ratio scale. (By definition, a "ratio scale" is an interval scale on which quantities are expressed with respect to a rational zero, i.e. a zero that is independent of the current data.) An indicator of the relative difference between x and y (or alternatively the relative change from x to y, whichever is the most appropriate description) is defined as a real-valued function $C(x, y)$ that has the following properties [TOR1985]:

1. $C(x, y) = 0$, if and only if $x = y$.
2. $C(x, y) > 0$, if and only if $x > y$.
3. $C(x, y) < 0$, if and only if $x < y$.
4. $C(x, y)$ is a continuous and increasing function of y when x is fixed.
5. $C(x, y) = C(ax, ay)$ for any values of $a > 0$.

Item 5 in the list is a requirement that the values of an indicator of relative difference must be independent of the unit of measurement. From the above it is clear that $H_0(x, y) = x/y$ as defined in Eq. (4.17) is not an indicator of relative difference. However, it can easily be shown that any indicator $C(x, y)$ of relative difference is a unique function of the ratio x/y alone. By setting $a = 1/y$ in property 5 above, one gets that $C(x, y) = C(x/y, 1)$, which proves this point. The following functions are all indicators of relative difference:

$$H_1(x, y) = \frac{x - y}{x}.$$

$$H_2(x, y) = \frac{x - y}{y}.$$

$$H_3(x, y) = \frac{x - y}{\min(x, y)}.$$

$$H_4(x, y) = \frac{x - y}{\max(x, y)}.$$

$$H_5(x, y) = \frac{x - y}{\left(\frac{x + y}{2}\right)}.$$

$$H_6(x, y) = \frac{x - y}{\sqrt{xy}}.$$

$$H_7(x, y) = \frac{x - y}{\left(\frac{[x^{-1} + y^{-1}]^{-1}}{2}\right)}.$$

$$H_8(x, y) = \frac{x - y}{\left(\frac{[x^k + y^k]^{1/k}}{2}\right)}.$$

$$H_9(x, y) = \frac{x - y}{K(x, y)}. \tag{4.18}$$

In $H_1(x,y)$ and $H_2(x,y)$, the absolute difference $x-y$ is compared to either the first or the second of the arguments, both being asymmetric. An indicator of relative difference is defined to be symmetric if and only if

$$H(x,y) = -H(y,x). \tag{4.19}$$

The lack of symmetry in $H_1(x,y)$ and $H_2(x,y)$ can be rectified by choosing in the denominator either the minimum or the maximum of the two arguments, as in $H_3(x,y)$ and $H_4(x,y)$. These four choices all have some problems for the present study. The asymmetry seen in the ratio, $H_0(x,y) = x/y$, has already been identified as problematic for purposes of comparing x with y. Likewise, $H_1(x,y)$ and $H_2(x,y)$ both suffer from the same problem. The problem with $H_3(x,y)$ and $H_4(x,y)$ is that, in the present application, the "point of comparison" (as represented by the denominator) is shifted from an experimental value to a calculated value or vice versa, in a rather *ad hoc* way. One would like the denominator to be a consistent quantity for all comparisons, not sometimes a measured value but at other times a calculated value, in a mixed fashion. In all the other cases of Eq. (4.18) the denominator is a mean value of x and y, in which case they are treated equally (thus symmetrically). In $H_5(x,y)$ the denominator is the arithmetic mean. In $H_6(x,y)$ it is the geometric mean. In $H_7(x,y)$ it is the harmonic mean. In $H_8(x,y)$ it is the moment mean of order k. In $H_9(x,y)$, the denominator $K(x,y)$ denotes any mean of x and y, thus $H_5(x,y)$ through $H_8(x,y)$ are all special cases of $H_9(x,y)$. There are other types of means used in statistics and economics, e.g. the Thiel mean, the Sato mean, the Vartia mean, etc., which are not of importance for the present work. There is one other mean that is of significance, however, and this is the so-called "logarithmic mean". Before discussing it, it is insightful to state, in a formal way, what a "mean" is. The properties of a mean of two numbers are given below:

1. $\min(x,y) \le K(x,y) \le \max(x,y)$.
2. $K(x,y)$ must be continuous.
3. $K(ax,ay) = aK(x,y)$ for all $a > 0$.
4. $K(x,y) = K(y,x)$.

Conditions 3 and 4 above are called the "homogeneity" and "symmetry" properties of the mean, respectively.

4.3.2 The logarithmic mean

The logarithmic mean of two positive numbers x and y is defined by [CAR1972]

$$L(x,y) = \frac{x-y}{\ln(x) - \ln(y)} = \frac{x-y}{\ln(x/y)}, \quad \text{for} \quad x \neq y,$$
$$L(x,x) = x. \tag{4.20}$$

The function $L(x,y)$ is symmetric and homogeneous in x and y and continuous at $x = y$. It is a legitimate mean as it satisfies all four conditions of a mean as expressed above. The logarithmic mean has values between the arithmetic and geometric means for al $x \neq y$:

$$\sqrt{xy} \le L(x,y) \le \frac{x+y}{2}, \tag{4.21}$$

with strict inequalities when $x \neq y$. Its significance will be discussed below.

4.3.3 Indicator of relative difference using the logarithmic mean

In the same way as in Eq. (4.18), one can define an indicator of relative difference in terms of the logarithmic mean as follows:

$$H_{10}(x,y) = \frac{x-y}{L(x,y)}. \tag{4.22}$$

Substitution of Eq (4.20) into Eq (4.22) gives the rather surprisingly simple result:

$$H_{10}(x,y) = \ln\left(\frac{x}{y}\right). \tag{4.23}$$

The problem with all the quantities defined in Eq (4.18) is that they are not additive – they are all so-called "non-additive indicators of relative difference". In contrast, $H_{10}(x,y)$ is the only one that has the property that it is additive. As an example, consider a ratio-scale quantity that undergoes change in stages, e.g. as evidenced by having different values when measured at different times. Let $\{x_1,\ x_2,\ x_3\ \ldots\ x_n\}$ denote such a set of measurements. The additive property holds, thus $H_{10}(x_1,x_n) = H_{10}(x_1,x_2) + H_{10}(x_2,x_3) + \ldots + H_{10}(x_{n-1},x_n)$.

In the context of the predictive power of nuclear models, Konobeyev et al. [KON2011] commented that an overestimation and underestimation of predicted cross sections compared to corresponding experimental values by the same factor in a large collection of data, should be considered as the "equal deficiency" of the models. This is reflected by symmetric indicators of relative difference but not by the those that are asymmetric.

It is standard practice to express relative differences as percentages, in which case they are normally referred to as "percentage differences". Törnqvist et al. [TOR1985] proposed the phrase "log percentage difference" for the quantity $H_{10}(x,y)$ when it is expressed as a percentage (i.e. when multiplied by 100), indicated with the symbol L% rather than % in order to avoid confusion. They also proposed the use of the term "log percent" for L% in order to clearly distinguish it from other percentages. They argued that all the other indicators of relative difference should disappear and that only the $H_{10}(x,y)$ form should be retained. They expressed the hope that all the asymmetric and non-additive "percentage difference" formalisms will eventually be regarded as "outdated concepts". There is no real difference between L% and %. It is simply an aid, introduced because Eq. (4.23) is often viewed with suspicion as it does not look like an indicator of relative difference to the untrained eye, unlike the more familiar form of Eq. (4.22).

4.3.4 Percentage difference of physical yields

For completeness, the exact formulations of the "percentage difference" between calculated and measured physical yields used in this work are summarized below.

$$H_1(Y_{CALC}(i), Y_{EXP}(i)) = 100\left[\frac{Y_{CALC}(i) - Y_{EXP}(i)}{Y_{CALC}(i)}\right];\quad 1 \leq i \leq N_r, \tag{4.24}$$

where N_r is the total number of reactions.

$$H_5(Y_{CALC}(i), Y_{EXP}(i)) = 100 \left[\frac{Y_{CALC}(i) - Y_{EXP}(i)}{\left(\frac{Y_{CALC}(i) + Y_{EXP}(i)}{2} \right)} \right]; \quad 1 \leq i \leq N_r. \tag{4.25}$$

The asymmetric function $H_1(Y_{CALC}(i), Y_{EXP}(i))$ is constrained at a maximum value of 100% when $Y_{CALC}(i) > Y_{EXP}(i)$ and unconstrained when $Y_{CALC}(i) < Y_{EXP}(i)$. In contrast, the symmetric function $H_5(Y_{CALC}(i), Y_{EXP}(i))$ is constrained in both directions (minimum and maximum limits of -200% and 200%, respectively).

4.3.5 Log percentage difference of physical yields

The symmetric function $H_{10}(Y_{CALC}(i), Y_{EXP}(i))$ is unconstrained and is expressed as:

$$H_{10}(Y_{CALC}(i), Y_{EXP}(i)) = 100 \ln \left(\frac{Y_{CALC}(i)}{Y_{EXP}(i)} \right); \quad 1 \leq i \leq N_r. \tag{4.26}$$

The values of this function are denoted by the symbol L% (log percent) instead of the usual % simply to uniquely distinguish it from the other formulations, as already alluded to. This is just a notation and the "log percent" should not be confused with the "log of a percentage".

It is not foreseen that the difference between any measured and corresponding calculated physical yield will exceed an order of magnitude. (Hopefully the agreement will be significantly better than that.) The ratio x/y ($x \geq y$) versus the relative difference $H(x, y) = (x - y)/K(x, y)$ (expressed as a percentage difference) for different forms of the mean $K(x, y)$ are shown in Fig. 4.2 up to a ratio of 10. The curve given by the logarithmic mean is located in between the curves obtained from the geometric and arithmetic means, in agreement with expectations based on Eq. (4.21).

4.4 EFFECTIVE CROSS SECTIONS AND UNCERTAINTIES

As already mentioned in Section 4.1, two sets of predicted physical yields were derived, one set based on TENDL-2015 cross sections and the other on the more recent TENDL-2017 cross sections. Each of these sets contains six subsets of results, one subset for each physics selection used in MCNP 6.1 to calculate the neutron flux. The six physics selections are Bertini/ABLA, Bertini/Dresner, CEM, INCL/ABLA, ISABEL/ABLA and ISABEL/Dresner. Thus, for each of the 104 reactions on which experimental yields could be extracted from the measured photon spectra, six predicted values based on TENDL-2015 and six predicted values based on TENDL-2017 are available. It also seems useful to calculate the predicted average yields to reduce the data. This was done separately for the TENDL-2015 and TENDL-2017 sets. For each isotope, the arithmetic mean of the 6 predicted yields was calculated, assuming that these 6 values constitute a discrete population of equal probability. Associated with this mean the standard deviation was also calculated. The values have been designated the following notation: The predicted average (mean) physical yield and its standard deviation are denoted by $\langle Y \rangle_{CALC}$ and

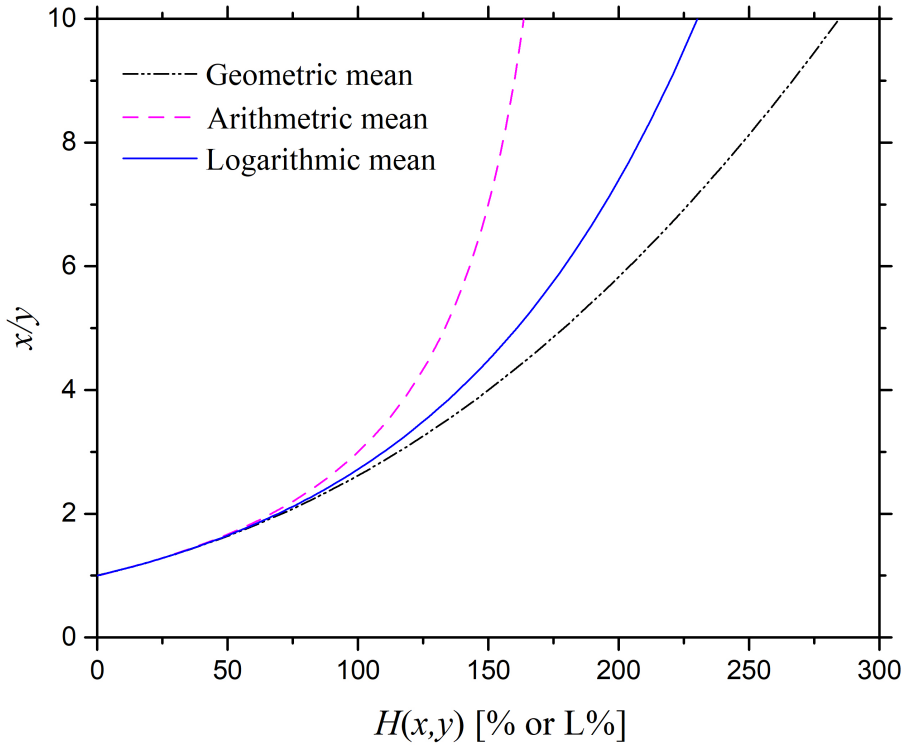


Figure 4.2: Fraction of two values x and y versus their percentage difference evaluated with different types of mean, as indicated.

S_{CALC}, respectively. The associated measured value is denoted by Y_{EXP} and its statistical uncertainty by ΔY_{STAT}.

The mean cross section for the formation of a particular radionuclide by neutron activation, $\overline{\sigma}_n$, has already been introduced and is given by Eq. (4.4). Within a TENDL data set, one can again average these values over the 6 physics selections, a quantity that we will denote by $\langle\overline{\sigma}_n\rangle$. This symbol represents the "average predicted formation cross section" for a particular radionuclide – averaged over all neutron energy groups (weighted by the neutron spectrum) and averaged over the 6 physics selections, all six considered to be equally probable.

It is also interesting to renormalize the above average predicted cross sections to the experimental values, assuming that the measurements better reflect reality than the predictions. For all 104 reactions studied in this work, such "average normalized formation cross sections" were calculated as follows:

$$\langle\overline{\sigma}\rangle = \langle\overline{\sigma}_n\rangle \frac{Y_{EXP}}{\langle Y\rangle_{CALC}}. \tag{4.27}$$

The uncertainty $\langle\overline{\Delta\sigma}\rangle$ associated with Eq. (4.27) was calculated by summing the individual uncertainties in quadrature. These include the experimental statistical uncertainty arising from the measured full-energy peak area (ΔY_{STAT}), the Monte Carlo statistical uncertainty associated with the neutron flux, estimated/assumed uncertainty in the beam current measurement (6%), detector efficiency (3%), decay corrections (2%), sample mass (1%), and finally the standard deviation arising from the 6 physics selections (S_{CALC}). We adopted S_{CALC} as an uncertainty since it does represent a spread in predicted values, of which we calculated the mean. In the case of the neutron flux, the statistical uncertainty introduced by the Monte Carlo process is sub-percent for the majority of reactions and in only three of the 104 reactions did

it exceed 3% – it never exceeded 5%.

To conclude, it should be mentioned that averages and standard deviations of the percentage differences and log percentage differences were calculated over all the 104 reactions observed. These will also be presented, for each physics selection, in Chapter 5. All the mathematical expressions presented in this chapter have been coded in Fortran. These codes needed the output from the Monte Carlo simulations as well as the raw data measured with the HPGe detector as input for further analysis. The final results are predicted and measured physical yields of the observed radionuclides induced by neutrons, as well as indicators of relative difference to facilitate an overall comparison between the predictions and the measurements.

Chapter 5

Results and Discussion

The final results after completion of the data analysis are presented here. First, all the activation products that could be uniquely identified and quantified as well as the relevant nuclear reactions for their formation are listed. Next, an investigation on the sensitivity of capture reactions to the neutron energy-group structure is discussed. This is followed by the experimental and predicted physical yields and associated cross sections. Next, an extensive discussion on the dependence of the predicted yields on the MCNP physics selections as well as a comparison with experimental data is presented. Finally, the differences between yield predictions based on the TENDL-2015 and TENDL-2017 cross sections are discussed.

5.1 NEUTRON-INDUCED ACTIVATION PRODUCTS

A total of 104 neutron-induced reactions or processes were uniquely identified from the measured spectra of gamma-rays emitted by their activation products. Processes with multiple channels to produce the final observed radionuclide were considered as a sum of all contributing reaction channels, e.g. where a target element with natural isotopic composition has more than one stable isotope. Care was also taken to properly include contributions from precursor decay. To have confidence in the results, any reaction whose identification was questionable was discarded, e.g. where a conflict was observed in results from the different counting sessions or where there was a lack of sufficiently strong photon emissions. Such cases, however, were relatively few. In general the measured spectra were of high quality and very clean. The observed reactions, their assigned identification numbers and the decay data used for their identification are presented in Table 5.1. The decay data are from NuDat 2.7 [SON2018].

The lightest identified reaction product is ^{7}Be (ID = 1) and the heaviest is ^{207}Bi (ID = 104). Due to the relatively long bombardment time and the fairly complex beam history, we were somewhat concerned about radionuclides with half-lives shorter than one day. Nevertheless, those cases where at least two counting sessions produced a physical yield with reasonable statistics and without any conflicts, were retained. At the other end of the scale, it was surprising to see ^{207}Bi so clearly, taking into consideration that its half-life is longer than 31 years. In cases where the half-life measured in years, we performed an extra counting session four months after the bombardment, when most short-lived radionuclides would have decayed significantly. This ensured a lower background in the spectra.

Table 5.1: Target nuclides, neutron-induced reactions and the decay data of observed residues used for their identification and quantification.

Target	ID	Reaction	Half-life (d)	γ-ray (keV)	Intensity (%)
^{9}Be	1	^{9}Be(n,3n)^{7}Be	53.22	477.6035	10.44
^{23}Na	2	^{23}Na(n,2n)^{22}Na	950.287	1274.537	99.940
	3	^{23}Na(n,γ)^{24}Na	0.624875	1368.626	99.9936
^{nat}Ti	4	^{nat}Ti(n,x)^{47}Ca	4.536	1297.09	67.0
	5	^{nat}Ti(n,x)^{44m}Sc	2.44208	271.241	86.7
	6	^{nat}Ti(n,x)^{46}Sc	83.79	889.277	99.9840
	7	^{nat}Ti(n,x)^{47}Sc	3.3492	159.381	68.3
	8	^{nat}Ti(n,x)^{48}Sc	1.81958	983.526	100.0
^{55}Mn	9	^{55}Mn(n,x)^{48}V	15.9735	983.525	99.98
	10	^{55}Mn(n,x)^{51}Cr	27.704	320.0824	9.910
	11	^{55}Mn(n,4n)^{52}Mn	5.591	744.233	90.0
	12	^{55}Mn(n,2n)^{54}Mn	312.20	834.848	99.9760
^{59}Co	13	^{59}Co(n,x)^{52}Mn	5.591	1434.092	100.0
	14	^{59}Co(n,x)^{54}Mn	312.20	834.848	99.9760
	15	^{59}Co(n,p)^{59}Fe	44.495	1099.245	56.5
	16	^{59}Co(n,4n)^{56}Co	77.236	846.770	99.9399
	17	^{59}Co(n,3n)^{57}Co	271.74	122.06065	85.60
	18	^{59}Co(n,2n)^{58}Co	70.86	810.7593	99.450
	19	^{59}Co(n,γ)^{60}Co	1925.28	1332.492	99.9826
^{nat}Ni	20	^{nat}Ni(n,x)^{51}Cr	27.704	320.0824	9.910
	21	^{nat}Ni(n,x)^{52}Mn	5.591	1434.092	100.0
	22	^{nat}Ni(n,x)^{54}Mn	312.20	834.848	99.9760
	23	^{nat}Ni(n,x)^{59}Fe	44.495	1099.245	56.5
	24	^{nat}Ni(n,x)^{56}Co	77.236	846.770	99.9399
	25	^{nat}Ni(n,x)^{57}Co	271.74	122.06065	85.60
	26	^{nat}Ni(n,x)^{58}Co	70.86	810.7593	99.450
	27	^{nat}Ni(n,x)^{60}Co	1925.28	1332.492	99.9826
	28	^{nat}Ni(n,xn)^{56}Ni	6.075	158.38	98.8
	29	^{nat}Ni(n,xn)^{57}Ni	1.4833	1377.63	81.7
^{nat}Br	30	^{nat}Br(n,x)^{75}Se	119.78	264.6576	58.9
	31	^{nat}Br(n,x)^{74}As	17.77	595.83	59.0
	32	^{nat}Br(n,xn)^{77}Br	2.3765	238.98	23.1
	33	^{81}Br(n,γ)^{82}Br	1.47008	776.517	83.4
^{nat}Rb	34	^{nat}Rb(n,x)^{82}Br	1.47008	776.517	83.4
	35	^{nat}Rb(n,xn)^{83}Rb	86.2	520.3991	45.0

Table 5.1: Target nuclides, neutron-induced reactions and the decay data of observed residues used for their identification and quantification (continuing from previous page).

Target	ID	Reaction	Half-life (d)	γ-ray (keV)	Intensity (%)
^{nat}Rb	36	^{nat}Rb(n,xn)^{84}Rb	32.82	881.6041	68.9
	37	^{nat}Rb(n,x)^{86}Rb	18.642	1077.0	8.64
^{89}Y	38	^{89}Y(n,x)^{83}Rb	86.2	520.3991	45.0
	39	^{89}Y(n,x)^{84}Rb	32.82	881.6041	68.9
	40	^{89}Y(n,x)^{86}Rb	18.642	1077.0	8.64
	41	^{89}Y(n,4n)^{86}Y	0.614167	1076.63	82.5
	42	^{89}Y(n,3n)^{87}Y	3.325	484.805	89.8
	43	^{89}Y(n,3n)^{87m}Y	0.55708	380.79	78.05
	44	^{89}Y(n,2n)^{88}Y	106.627	898.042	93.7
^{93}Nb	45	^{93}Nb(n,x)^{87}Y	3.325	484.805	89.8
	46	^{93}Nb(n,x)^{88}Y	106.627	898.042	93.7
	47	^{93}Nb(n,x)^{89}Zr	3.26708	909.15	99.04
	48	^{93}Nb(n,4n)^{90}Nb	0.60833	1129.224	92.7
	49	^{93}Nb(n,3n)^{91m}Nb	60.86	1204.67	2.0
	50	^{93}Nb(n,2n)^{92m}Nb	10.15	934.44	99.15
^{103}Rh	51	^{103}Rh(n,x)^{96}Tc	4.28	778.22	99.760
	52	^{103}Rh(n,p)^{103}Ru	39.247	497.085	91.0
	53	^{103}Rh(n,5n)^{99g}Rh	16.1	353.05	34.5
	54	^{103}Rh(n,4n)^{100}Rh	0.8667	539.512	80.6
	55	^{103}Rh(n,3n)^{101g}Rh	1205.3	127.226	68.0
	56	^{103}Rh(n,3n)^{101m}Rh	4.34	306.857	81.0
	57	^{103}Rh(n,2n)^{102g}Rh	207.3	468.58	2.90
	58	^{103}Rh(n,2n)^{102m}Rh	1366.77	631.29	56.0
^{nat}Ag	59	^{nat}Ag(n,x)^{105}Rh	1.4733	318.9	19.1
	60	^{nat}Ag(n,xn)^{105}Ag	41.29	344.52	41.4
	61	^{nat}Ag(n,xn)^{106m}Ag	8.28	1045.83	29.6
	62	^{nat}Ag(n,x)^{110m}Ag	249.83	657.7600	95.61
^{nat}In	63	^{nat}In(n,x)^{110m}Ag	249.83	657.7600	95.61
	64	^{115}In(n,p)^{115m}Cd	44.56	933.838	2.0
	65	^{nat}In(n,xn)^{111}In	2.8047	245.35	94.1
	66	^{nat}In(n,x)^{114m}In	49.51	190.27	15.56
^{127}I	67	^{127}I(n,x)^{120m}Sb	5.76	1171.7	100.0
	68	^{127}I(n,x)^{122}Sb	2.7238	564.24	70.67
	69	^{127}I(n,x)^{124}Sb	60.20	602.7260	97.8
	70	^{127}I(n,x)^{123m}Te	119.2	159.00	84.0

Table 5.1: Target nuclides, neutron-induced reactions and the decay data of observed residues used for their identification and quantification (continuing from previous page).

Target	ID	Reaction	Half-life (d)	γ-ray (keV)	Intensity (%)
^{127}I	71	^{127}I(n,5n)^{123}I	0.550979	158.97	83.3
	72	^{127}I(n,4n)^{124}I	4.1760	602.73	62.9
	73	^{127}I(n,2n)^{126}I	12.93	388.633	35.6
^{133}Cs	74	^{133}Cs(n,5n)^{129}Cs	1.33583	371.918	30.6
	75	^{133}Cs(n,2n)^{132}Cs	6.480	667.714	97.59
	76	^{133}Cs(n,γ)^{134}Cs	754.314	604.721	97.62
^{141}Pr	77	^{141}Pr(n,x)^{139}Ce	137.641	165.8575	80.0
	78	^{141}Pr(n,p)^{141}Ce	32.511	145.4433	48.4
	79	^{141}Pr(n,γ)^{142}Pr	0.7967	1575.6	3.7
^{nat}Gd	80	^{nat}Gd(n,x)^{156}Eu	15.19	811.77	9.7
	81	^{nat}Gd(n,x)^{157}Eu	0.6325	410.723	17.8
	82	^{nat}Gd(n,xn)^{151}Gd	123.9	174.70	2.96
	83	^{nat}Gd(n,x)^{153}Gd	240.4	103.18012	21.1
	84	^{nat}Gd(n,x)^{159}Gd	0.76996	363.5430	11.78
	85	^{160}Gd(n,γ)^{161}Gd $\rightarrow^{161}$Tb	6.89	74.56669	10.2
^{169}Tm	86	^{169}Tm(n,5n)^{165}Tm	1.2525	242.917	35.5
	87	^{169}Tm(n,3n)^{167}Tm	9.25	531.54	1.61
	88	^{169}Tm(n,2n)^{168}Tm	93.1	815.989	50.95
^{181}Ta	89	^{181}Ta(n,p)^{181}Hf	42.39	482.18	80.5
	90	^{181}Ta(n,5n)^{177}Ta	2.3567	112.9	7.2
	91	^{181}Ta(n,γ)^{182}Ta	114.74	1121.290	35.24
^{197}Au	92	^{197}Au(n,x)^{192}Ir	73.829	316.50618	82.86
	93	^{197}Au(n,4n)^{194}Au	1.58417	328.464	60.4
	94	^{197}Au(n,3n)^{195}Au	186.01	98.857	11.21
	95	^{197}Au(n,2n)^{196}Au	6.1669	355.73	87.0
	96	^{197}Au(n,γ)^{198g}Au	2.6941	411.80205	95.62
^{nat}Tl	97	^{nat}Tl(n,x)^{203}Hg	46.594	279.1952	81.56
	98	^{nat}Tl(n,xn)^{200}Tl	1.0875	367.942	87.0
	99	^{nat}Tl(n,xn)^{201}Tl	3.0421	167.43	10.00
	100	^{nat}Tl(n,xn)^{202}Tl	12.31	439.510	91.5
^{209}Bi	101	^{209}Bi(n,6n)^{204}Bi	0.4675	899.15	99.0
	102	^{209}Bi(n,5n)^{205}Bi	15.31	703.45	31.1
	103	^{209}Bi(n,4n)^{206}Bi	6.243	803.10	99.0
	104	^{209}Bi(n,3n)^{207}Bi	11523.6	569.698	97.75

5.2 SENSITIVITY OF CAPTURE REACTIONS ON GROUP STRUCTURE

As mentioned in Subsection 4.1.3, group cross sections were assigned for all neutron energy groups by applying the closed-form Newton-Cotes formulae to the pointwise TENDL data and not by calculating the group-averaged cross sections by means of weighting functions. We were confident that this would not be a problem for threshold reactions but less confident in the case of capture reactions as the widths of the groups below 1 MeV become increasingly larger relative to their respective energy scales. In particular, at very low energies where capture cross sections are high and have a $1/E$ relationship, some underestimation within those groups can be expected.

The several different ways investigated for assigning cross sections to the neutron energy groups are expected to produce different physical-yield results. The question is by how much do they differ? This is shown in Table 5.2 for one selected capture reaction (^{23}Na(n,γ)^{24}Na) and one selected threshold reaction (^{nat}Ti(n,x)^{46}Sc). These are typical cases – the other reactions show very similar behaviour.

Table 5.2: Physical yields for a capture reaction and a threshold reaction, utilizing different strategies to determine group cross sections from the pointwise TENDL-2017 data. Upper and lower limits are also shown, determined from interpolated minimum and maximum values.

Method[a]	Physical yield (Bq μAh^{-1} g^{-1})	
	^{23}Na(n,γ)^{24}Na	^{nat}Ti(n,x)^{46}Sc
Mid-value of group	2350.11	214.99
Newton-Cotes of degree 1	2403.32	215.28
Newton-Cotes of degree 2	2367.85	215.09
Newton-Cotes of degree 3	2363.90	215.02
Newton-Cotes of degree 4	2360.68	214.94
Minimum value in group	2015.67	202.04
Maximum value in group	2833.09	228.52

[a]Neutron spectrum according to CEM physics selection in MCNP 6.1

It is clear from Table 5.2 that the variation of the yields with respect to interpolation method is indeed small for the threshold reaction, with only a 0.16% difference between results obtained with Newton-Cotes of degrees 1 and 4, respectively. The lowest and highest tabled values differ by only about 13% in this case. The variation is larger for the capture reaction, with a 1.8% difference between results obtained with Newton-Cotes of degrees 1 and 4. In this case the lowest and highest tabled values differ by about 40%. The Newton-Cotes result of order 4 is about 20% lower than the upper limit. Thus, since one would expect an underestimation, it is highly unlikely to be more than 20%. Taking into consideration that the interpolated maximum cross section in each group will never be realistically chosen to represent the entire group, one knows that the upper limit is a rather severe limit. Consequently, the actual error introduced by the group structure will certainly be significantly lower than 20%. As will be shown later,

the variation between the different physics selections is larger. The conclusion is that there are no concerns for the threshold reactions in terms of the interpolation method and perhaps a few percent underestimation in the case of the capture reactions, but never exceeding 20%.

It provides insight to compare the excitation functions for the above two reactions, shown in Fig. 5.1, as obtained from the TENDL-2017 library. It is necessary to plot the capture reaction on a log-log scale in order to display the low-energy data, while a linear-linear scale works better for the threshold reaction. The $1/E$ relationship is evident for the ^{23}Na(n,γ)^{24}Na reaction in the low-energy region as well as averaging over the resonance region in TENDL.

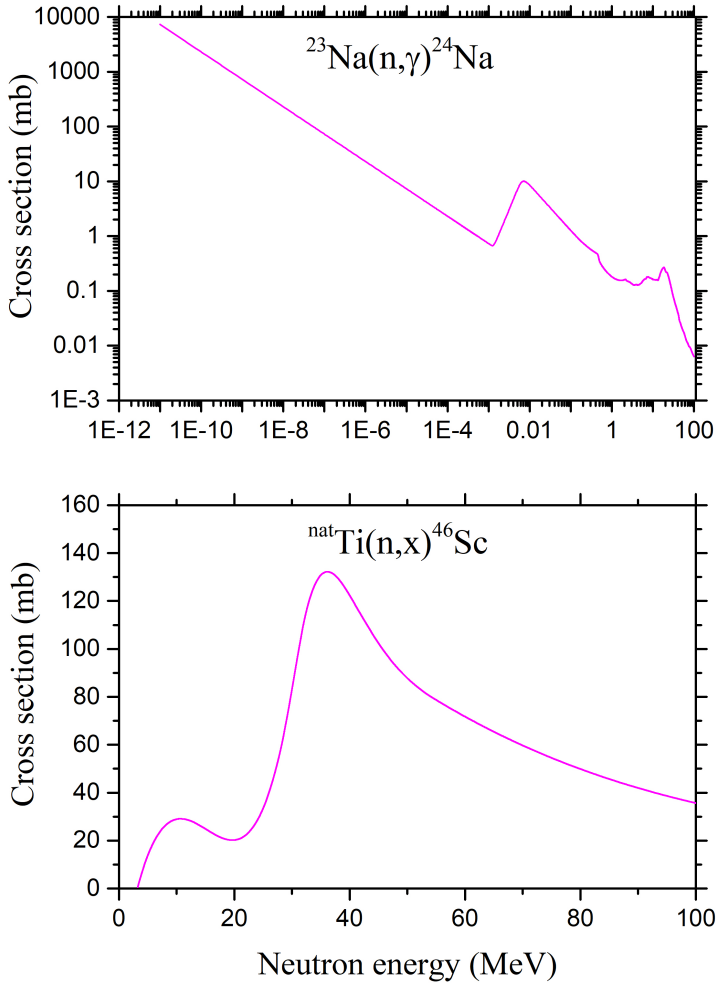


Figure 5.1: Excitation functions (i.e. cross sections versus energy) for the capture reaction ^{23}Na(n,γ)^{24}Na and the threshold reaction ^{nat}Ti(n,x)^{26}Sc. The data are from the TENDL-2017 library.

5.3 PHYSICAL YIELDS

The physical yields (see Section 4.1) calculated using TENDL-2015 and TENDL-2017 cross sections, for the different physics selections used to calculate the neutron flux with MCNP 6.1, are shown in Tables C.1 and D.1 in Appendices C and D, respectively. Note that we moved these results to the Appendices as they are rather numerous, however, figures of all results will be shown below. Here we will only present the numerical averages and standard deviations as well as a comparison with the experimental results of this study. The experimental and calculated

physical yields will be compared by means of the "log percentage difference" formulation of Eq. (4.26), namely $H_{10}(Y_{CALC}, Y_{EXP})$. One case was selected, however, to illustrate also the ratio and other forms of the "percentage difference", as given by equations (4.17), (4.24) and (4.25), respectively.

Figure 5.2 shows the results obtained with the TENDL-2017 cross sections and the CEM physics selection for the neutron flux calculation with MCNP 6.1. The tiles indicated (a) and (b) show the asymmetric quantities $H_0(Y_{CALC}, Y_{EXP})$ and $H_1(Y_{CALC}, Y_{EXP})$, respectively, expressed as percentages. Similarly, tiles (c) and (d) show the symmetric quantities $H_5(Y_{CALC}, Y_{EXP})$ and $H_{10}(Y_{CALC}, Y_{EXP})$, respectively. For the purposes of the present work, both the symmetric forms will suffice, however, we chose $H_{10}(Y_{CALC}, Y_{EXP})$ as it does not saturate, as discussed at length in Chapter 4. It is immediately clear from Fig. 5.2 that there is a significant spread in the results, with the calculations more often overpredicting the measured physical yields but significant underpredictions are also not rare. The dashed lines in tiles (c) and (d) give an indication of scale. A factor of 2 is equivalent to values of ±66.67% and ±69.31L% for $H_5(Y_{CALC}, Y_{EXP})$ and $H_{10}(Y_{CALC}, Y_{EXP})$, respectively, indicated by the red dashed lines. A factor of 3 is equivalent to values of ±100% and ±109.86L% for $H_5(Y_{CALC}, Y_{EXP})$ and $H_{10}(Y_{CALC}, Y_{EXP})$, respectively, indicated by the blue dashed lines. In tile (d) is also shown a log percentage difference equiva-

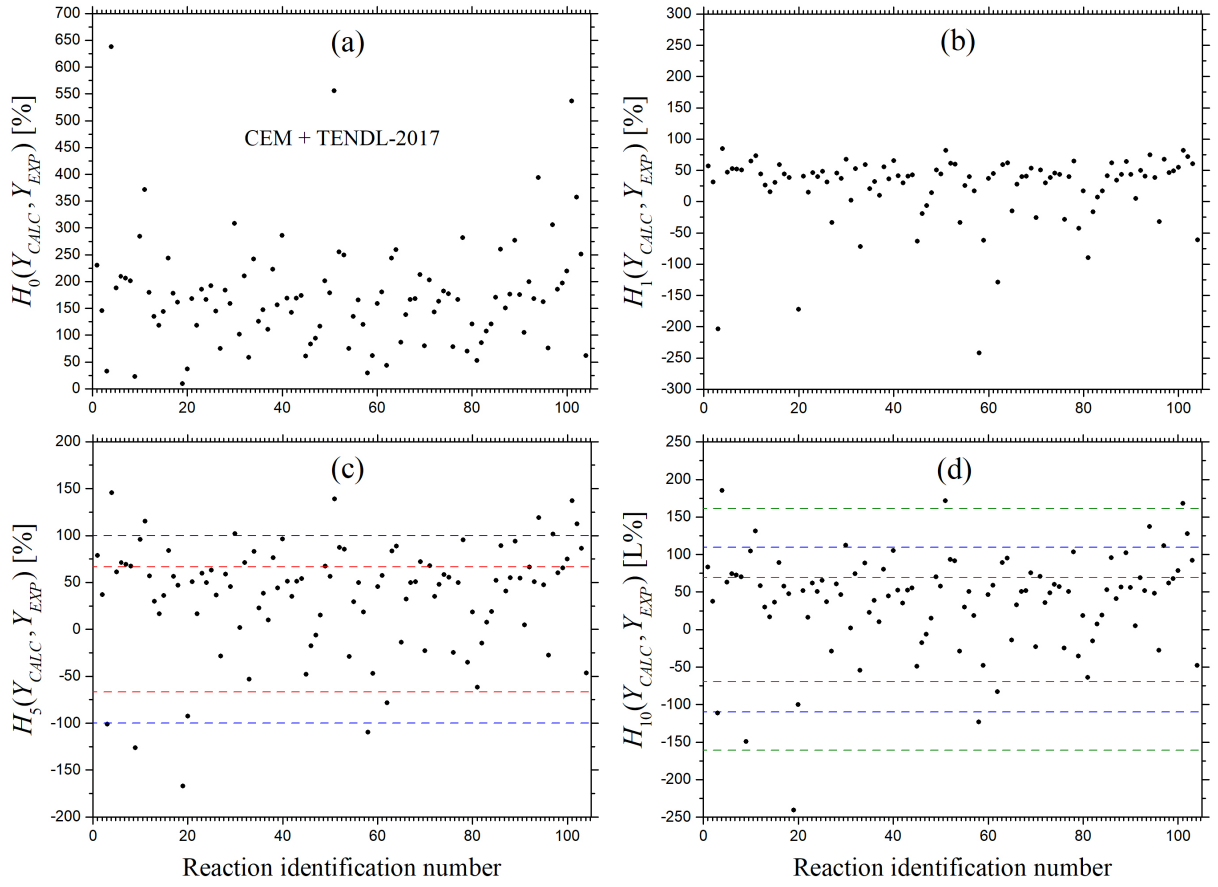


Figure 5.2: Percentage differences between calculated and measured physical yields (solid symbols), plotted versus the reaction identification number (see Table 5.1) according to different indicators of relative difference, as indicated. Tiles (a) and (b) show asymmetric cases (see Eq. 4.18). In the symmetric cases shown in tiles (c) and (d), the red dashed lines correspond to a factor of 2 actual difference between the two yield values that are compared, while the blue dashed lines indicate a factor of 3 actual difference. In tile (d), the green dashed lines indicate a factor of 5 actual difference.

lent to a factor of 5, namely ± 160.94L%, indicated by the green dashed lines. The rather large body of results will be presented next.

The calculated average physical yields based on cross sections from the TENDL-2015 and TENDL-2017 libraries as well as the corresponding experimental values are shown in Tables 5.3 and 5.4, respectively. The experimental yields have been calculated as described in Section 4.2 and Eq. (4.16) specifically. For each reaction, the value obtained from the counting session that yielded the best counting statistics (i.e. the smallest statistical uncertainty) has been included in the tables. In the case of the calculated physical yields, the values obtained from the Newton-Cotes formula of order 4 (see Tables 4.2 and 5.2) have been adopted. The data analysis pertaining to the average calculated yields, effective cross sections and uncertainties are described in Section 4.4.

5.3.1 Dependence on physics selection

Figures 5.3 and 5.4 show the log percentage differences of calculated and measured physical yields, plotted versus reaction ID number, for all the MCNP 6.1 physics selections in conjunction with the TENDL-2015 and TENDL-2017 cross sections, respectively. The six physics selections are Bertini/ABLA, Bertini/Dresner, CEM, INCL/ABLA, ISABEL/ABLA and ISABEL/Dresner (see also Chapters 3 and 4). While the overall trends are similar, there clearly are differences between the various data sets, both with respect to the physics selection and the choice of TENDL library used. As before, the dashed red, blue and green lines indicate differences of factor 2, 3 and 5, respectively.

It is useful to project the data of Figs. 5.3 and 5.4 onto the y-axis, plotted as histograms. This was done for the absolute values of the log percentage difference, shown in Figs. 5.5 and 5.6, respectively. From an overview perspective, the TENDL-2015 and TENDL-2017 versions look quite similar. It is immediately evident that the distributions do not peak at the lowest bins, with INCL/ABLA having a maximum closest to zero. One might also make an early statement concerning the CEM physics selection, namely that it appears to be shifted towards lower values than the physics choices which include the Bertini and ISABEL internuclear cascade options. Based solely on Figs. 5.5 and 5.6, the INCL/ABLA selection seems to be superior, followed by CEM, with Bertini/ABLA, Bertini/Dresner, ISABEL/ABLA and ISABEL/Dresner selections leading to larger differences between the calculated predictions and the measured values, thus poorer overall agreement.

Another way to look at these distributions quantitatively is to calculate their means and standard deviations, which are presented in Table 5.5. As expected, the INCL/ABLA selection displays a significantly smaller average than the other physics selections, followed by CEM. The overall result is an overprediction by the calculations. The standard deviations are quite large in all cases and rather similar in magnitude. The averages obtained with TENDL-2017 cross sections are marginally smaller than obtained with TENDL-2015 values but the standard deviations are somewhat larger, indicating a somewhat larger spread in the case of the newer library. From an overview perspective, one cannot really say which library (i.e. TENDL-2015 or TENDL-2017) gives the better results. The two sets of results are very similar.

Table 5.3: Predicted average physical yields (TENDL-2015 + MCNP 6.1) as well as corresponding measurements and associated cross sections.

		Physical yield (Bq μAh^{-1} g^{-1})				Cross section (mb)
ID	Reaction	$\langle Y \rangle_{\mathrm{CALC}}$	S_{CALC}	Y_{EXP}	ΔY_{STAT}	$\langle \overline{\sigma} \rangle \pm \langle \overline{\Delta\sigma} \rangle$
1	^{9}Be(n,3n)^{7}Be	53.91	5.71	22.53	0.22	0.147 ± 0.019
2	^{23}Na(n,2n)^{22}Na	54.55	11.63	23.81	0.31	7.05 ± 1.58
3	^{23}Na(n,γ)^{24}Na	2878.55	413.48	7177.74	259.56	1.40 ± 0.23
4	^{nat}Ti(n,x)^{47}Ca	38.11	7.50	22.86	1.61	0.0673 ± 0.0148
5	^{nat}Ti(n,x)^{44m}Sc	213.64	24.47	109.36	4.18	0.174 ± 0.024
6	^{nat}Ti(n,x)^{46}Sc	272.21	37.63	102.45	0.36	5.58 ± 0.87
7	^{nat}Ti(n,x)^{47}Sc	10883.75	2061.82	3851.23	9.86	8.37 ± 1.69
8	^{nat}Ti(n,x)^{48}Sc	5403.92	1041.94	2325.18	22.65	2.74 ± 0.56
9	^{55}Mn(n,x)^{48}V	0.41	0.05	1.09	0.16	0.0131 ± 0.0027
10	^{55}Mn(n,x)^{51}Cr	14.97	0.73	5.09	0.41	0.106 ± 0.013
11	^{55}Mn(n,4n)^{52}Mn	262.31	18.54	90.72	0.54	0.380 ± 0.038
12	^{55}Mn(n,2n)^{54}Mn	423.75	93.37	191.73	0.15	44.52 ± 10.30
13	^{59}Co(n,x)^{52}Mn	0.82	0.09	0.80	0.13	0.00363 ± .00076
14	^{59}Co(n,x)^{54}Mn	8.31	1.11	7.60	0.08	1.90 ± 0.29
15	^{59}Co(n,p)^{59}Fe	238.90	39.40	136.03	0.27	4.84 ± 0.87
16	^{59}Co(n,4n)^{56}Co	19.48	1.44	7.75	0.09	0.481 ± 0.050
17	^{59}Co(n,3n)^{57}Co	109.14	19.95	51.94	0.07	11.29 ± 2.21
18	^{59}Co(n,2n)^{58}Co	1714.84	374.69	855.64	0.32	48.38 ± 11.10
19	^{59}Co(n,γ)^{60}Co	18.79	3.26	72.69	0.11	111.65 ± 21.01
20	^{nat}Ni(n,x)^{51}Cr	2.71	0.38	5.48	1.24	0.121 ± 0.033
21	^{nat}Ni(n,x)^{52}Mn	26.05	1.03	15.81	0.27	0.0710 ± 0.0060
22	^{nat}Ni(n,x)^{54}Mn	9.48	1.90	6.25	0.06	1.55 ± 0.33
23	^{nat}Ni(n,x)^{59}Fe	6.15	1.20	3.25	0.11	0.115 ± 0.024
24	^{nat}Ni(n,x)^{56}Co	132.02	20.64	70.70	0.12	4.35 ± 0.75
25	^{nat}Ni(n,x)^{57}Co	354.95	75.78	154.69	0.11	33.41 ± 7.51
26	^{nat}Ni(n,x)^{58}Co	1868.86	158.21	1123.45	0.43	63.56 ± 6.99
27	^{nat}Ni(n,x)^{60}Co	3.43	0.59	3.89	0.05	5.96 ± 1.11
28	^{nat}Ni(n,xn)^{56}Ni	27.50	3.64	14.07	0.61	0.0682 ± 0.0107
29	^{nat}Ni(n,xn)^{57}Ni	5121.77	1067.63	2686.46	15.69	3.26 ± 0.72
30	^{nat}Br(n,x)^{75}Se	2.39	0.10	0.86	0.29	0.112 ± 0.039
31	^{nat}Br(n,x)^{74}As	37.36	4.92	29.10	0.76	0.562 ± 0.085
32	^{nat}Br(n,xn)^{77}Br	7790.70	1428.81	3223.99	90.15	8.30 ± 1.65
33	^{81}Br(n,γ)^{82}Br	54406.39	10841.36	84363.84	319.85	134.05 ± 28.45
34	^{nat}Rb(n,x)^{82}Br	938.57	161.84	300.75	10.61	0.513 ± 0.097
35	^{nat}Rb(n,xn)^{83}Rb	292.57	55.04	203.30	0.46	20.31 ± 4.08

Table 5.3: Predicted average physical yields (TENDL-2015 + MCNP 6.1) as well as corresponding measurements and associated cross sections (continuing from previous page).

		Physical yield (Bq μAh^{-1} g^{-1})				Cross section (mb)
ID	Reaction	$\langle Y \rangle_{\mathrm{CALC}}$	S_{CALC}	Y_{EXP}	ΔY_{STAT}	$\langle \overline{\sigma} \rangle \pm \langle \overline{\Delta\sigma} \rangle$
36	^{nat}Rb(n,xn)^{84}Rb	2715.07	585.00	1344.75	0.96	51.08 ± 11.58
37	^{nat}Rb(n,x)^{86}Rb	3931.96	665.58	3173.59	5.22	68.43 ± 12.57
38	^{89}Y(n,x)^{83}Rb	3.18	0.13	1.23	0.11	0.129 ± 0.016
39	^{89}Y(n,x)^{84}Rb	33.98	3.67	14.89	0.36	0.592 ± 0.078
40	^{89}Y(n,x)^{86}Rb	89.14	18.27	25.33	3.38	0.569 ± 0.145
41	^{89}Y(n,4n)^{86}Y	7188.90	498.28	4040.72	219.38	3.01 ± 0.34
42	^{89}Y(n,3n)^{87}Y	10233.95	1851.50	5956.05	12.05	23.89 ± 4.64
43	^{89}Y(n,3n)^{87m}Y	47020.20	8428.17	23104.23	429.87	15.53 ± 3.00
44	^{89}Y(n,2n)^{88}Y	960.06	214.74	457.41	0.52	58.69 ± 13.76
45	^{93}Nb(n,x)^{87}Y	55.64	2.57	96.12	2.35	0.406 ± 0.036
46	^{93}Nb(n,x)^{88}Y	7.81	1.03	9.14	0.09	1.23 ± 0.18
47	^{93}Nb(n,x)^{89}Zr	143.29	5.71	157.24	1.44	0.653 ± 0.054
48	^{93}Nb(n,4n)^{90}Nb	8565.94	808.81	7175.02	75.49	5.52 ± 0.65
49	^{93}Nb(n,3n)^{91m}Nb	150.07	28.63	63.71	1.86	4.88 ± 1.00
50	^{93}Nb(n,2n)^{92m}Nb	4059.46	850.62	1880.49	1.12	24.01 ± 5.31
51	^{103}Rh(n,x)^{96}Tc	117.27	6.07	27.27	0.29	0.164 ± 0.015
52	^{103}Rh(n,p)^{103}Ru	79.63	13.30	25.81	0.22	1.41 ± 0.26
53	^{103}Rh(n,5n)^{99g}Rh	25.89	1.22	10.34	0.31	0.234 ± 0.021
54	^{103}Rh(n,4n)^{100}Rh	4874.72	636.31	5854.79	12.27	7.10 ± 1.05
55	^{103}Rh(n,3n)^{101g}Rh	7.14	1.57	4.24	0.13	7.13 ± 1.67
56	^{103}Rh(n,3n)^{101m}Rh	7916.71	1710.89	3843.71	1.90	23.25 ± 5.28
57	^{103}Rh(n,2n)^{102g}Rh	206.94	44.11	138.80	0.98	40.09 ± 9.00
58	^{103}Rh(n,2n)^{102m}Rh	34.04	7.42	93.39	0.18	177.82 ± 40.70
59	^{nat}Ag(n,x)^{105}Rh	543.27	103.62	854.91	112.52	1.84 ± 0.45
60	^{nat}Ag(n,xn)^{105}Ag	579.48	115.75	288.04	0.52	17.39 ± 3.68
61	^{nat}Ag(n,xn)^{106m}Ag	3171.25	626.54	1593.24	3.21	19.28 ± 4.04
62	^{109}Ag(n,γ)^{110m}Ag	47.09	7.10	113.20	0.25	41.34 ± 6.94
63	^{nat}In(n,x)^{110m}Ag	1.84	0.26	0.73	0.03	0.286 ± 0.046
64	^{115}In(n,p)^{115m}Cd	30.01	6.15	9.58	0.84	0.664 ± 0.155
65	^{nat}In(n,xn)^{111}In	749.06	128.27	746.55	2.34	3.26 ± 0.60
66	^{nat}In(n,x)^{114m}In	1987.23	397.07	1100.08	0.70	84.66 ± 17.94
67	^{127}I(n,x)^{120m}Sb	3.51	0.20	1.98	0.05	0.0198 ± 0.0019
68	^{127}I(n,x)^{122}Sb	92.24	13.18	49.77	8.23	0.234 ± 0.054
69	^{127}I(n,x)^{124}Sb	4.60	0.86	1.70	0.02	0.176 ± 0.035
70	^{127}I(n,x)^{123m}Te	2.73	0.10	1.98	0.05	0.410 ± 0.035

Table 5.3: Predicted average physical yields (TENDL-2015 + MCNP 6.1) as well as corresponding measurements and associated cross sections (continuing from previous page).

		Physical yield (Bq μAh^{-1} g^{-1})				Cross section (mb)
ID	Reaction	$\langle Y \rangle_{\mathrm{CALC}}$	S_{CALC}	Y_{EXP}	ΔY_{STAT}	$\langle \bar{\sigma} \rangle \pm \langle \overline{\Delta\sigma} \rangle$
71	^{127}I(n,5n)^{123}I	7112.71	354.98	2821.89	162.73	2.69 ± 0.28
72	^{127}I(n,4n)^{124}I	3837.63	510.46	2074.24	3.21	14.95 ± 2.25
73	^{127}I(n,2n)^{126}I	7054.59	1511.46	3524.25	1.74	78.30 ± 17.66
74	^{133}Cs(n,5n)^{129}Cs	2497.96	132.62	1427.20	193.97	3.46 ± 0.56
75	^{133}Cs(n,2n)^{132}Cs	14459.82	3068.29	6197.98	3.43	72.27 ± 16.16
76	^{133}Cs(n,γ)^{134}Cs	259.70	48.25	281.50	0.25	381.92 ± 76.83
77	^{141}Pr(n,x)^{139}Ce	327.10	66.64	168.37	0.13	44.25 ± 9.54
78	^{141}Pr(n,p)^{141}Ce	47.17	9.75	13.90	0.14	0.862 ± 0.188
79	^{141}Pr(n,γ)^{142}Pr	32484.61	6043.67	46179.77	913.85	70.19 ± 14.13
80	^{nat}Gd(n,x)^{156}Eu	76.10	11.99	53.46	1.20	1.73 ± 0.30
81	^{nat}Gd(n,x)^{157}Eu	1851.98	293.05	3164.81	251.38	4.27 ± 0.81
82	^{nat}Gd(n,xn)^{151}Gd	9.57	1.04	11.62	1.59	3.08 ± 0.58
83	^{nat}Gd(n,x)^{153}Gd	47.66	8.20	39.15	0.82	20.09 ± 3.76
84	^{nat}Gd(n,x)^{159}Gd	47915.50	6945.50	36248.00	94.08	59.45 ± 9.61
85	^{160}Gd(n,γ)^{161}Gd ^{161}Gd$\rightarrow^{161}$Tb	3228.74	568.23	1940.23	22.51	28.46 ± 5.44
86	^{169}Tm(n,5n)^{165}Tm	6806.73	588.33	2582.15	5.98	7.45 ± 0.83
87	^{169}Tm(n,3n)^{167}Tm	5428.18	1195.15	2923.23	18.64	61.85 ± 14.30
88	^{169}Tm(n,2n)^{168}Tm	939.52	187.58	435.92	0.39	92.87 ± 19.66
89	^{181}Ta(n,p)^{181}Hf	14.98	3.04	4.51	0.31	0.469 ± 0.106
90	^{181}Ta(n,5n)^{177}Ta	6051.01	694.85	3281.67	47.79	19.05 ± 2.58
91	^{181}Ta(n,γ)^{182}Ta	2865.03	520.48	2351.63	9.05	660.78 ± 130.36
92	^{197}Au(n,x)^{192}Ir	1.07	0.14	0.64	0.12	0.126 ± 0.030
93	^{197}Au(n,4n)^{194}Au	13540.35	2428.86	7071.54	40.49	29.94 ± 5.77
94	^{197}Au(n,3n)^{195}Au	255.33	58.10	52.17	1.00	25.87 ± 6.18
95	^{197}Au(n,2n)^{196}Au	11710.38	2355.78	5867.86	2.52	96.54 ± 20.57
96	^{197}Au(n,γ)^{198g}Au	72030.64	13147.64	90171.43	36.47	647.77 ± 127.81
97	^{nat}Tl(n,x)^{203}Hg	28.96	4.57	9.13	0.10	1.181 ± 0.205
98	^{nat}Tl(n,xn)^{200}Tl	5285.46	567.44	2897.74	17.57	8.77 ± 1.13
99	^{nat}Tl(n,xn)^{201}Tl	5468.66	897.03	2537.86	20.40	21.42 ± 3.83
100	^{nat}Tl(n,xn)^{202}Tl	3328.60	636.88	1305.70	0.68	44.53 ± 9.08
101	^{209}Bi(n,6n)^{204}Bi	5284.10	246.42	1081.13	83.81	1.45 ± 0.17
102	^{209}Bi(n,5n)^{205}Bi	766.51	69.89	210.97	0.52	9.20 ± 1.06
103	^{209}Bi(n,4n)^{206}Bi	4037.56	720.06	1396.62	1.55	24.72 ± 4.74
104	^{209}Bi(n,3n)^{207}Bi	4.09	0.93	5.28	0.02	172.02 ± 41.14

Table 5.4: Predicted average physical yields (TENDL-2017 + MCNP 6.1) as well as corresponding measurements and associated cross sections.

		Physical yield (Bq μAh^{-1} g^{-1})				Cross section (mb)
ID	Reaction	$\langle Y \rangle_{\mathrm{CALC}}$	S_{CALC}	Y_{EXP}	ΔY_{STAT}	$\langle \overline{\sigma} \rangle \pm \langle \overline{\Delta\sigma} \rangle$
1	^{9}Be(n,3n)^{7}Be	53.91	5.71	22.53	0.22	0.147 ± 0.019
2	^{23}Na(n,2n)^{22}Na	42.52	9.33	23.81	0.31	7.04 ± 1.63
3	^{23}Na(n,γ)^{24}Na	2782.29	454.62	7177.74	259.56	1.40 ± 0.25
4	^{nat}Ti(n,x)^{47}Ca	159.87	23.01	22.86	1.61	0.0675 ± 0.0118
5	^{nat}Ti(n,x)^{44m}Sc	217.35	25.51	109.36	4.18	0.174 ± 0.025
6	^{nat}Ti(n,x)^{46}Sc	247.20	34.01	102.45	0.36	5.58 ± 0.863
7	^{nat}Ti(n,x)^{47}Sc	9551.10	1850.23	3851.23	9.86	8.37 ± 1.72
8	^{nat}Ti(n,x)^{48}Sc	5670.77	1080.58	2325.18	22.65	2.74 ± 0.56
9	^{55}Mn(n,x)^{48}V	0.22	0.03	1.09	0.16	0.0131 ± 0.0027
10	^{55}Mn(n,x)^{51}Cr	13.37	0.52	5.09	0.41	0.106 ± 0.012
11	^{55}Mn(n,4n)^{52}Mn	331.47	22.15	90.72	0.54	0.380 ± 0.037
12	^{55}Mn(n,2n)^{54}Mn	424.93	93.24	191.73	0.15	44.52 ± 10.26
13	^{59}Co(n,x)^{52}Mn	0.96	0.11	0.80	0.13	0.00363 ± 0.00076
14	^{59}Co(n,x)^{54}Mn	9.70	1.32	7.60	0.08	1.90 ± 0.29
15	^{59}Co(n,p)^{59}Fe	237.41	39.34	136.03	0.27	4.84 ± 0.87
16	^{59}Co(n,4n)^{56}Co	18.79	1.39	7.75	0.09	0.481 ± 0.050
17	^{59}Co(n,3n)^{57}Co	107.19	19.58	51.94	0.07	11.29 ± 2.21
18	^{59}Co(n,2n)^{58}Co	1702.92	371.95	855.64	0.32	48.38 ± 11.10
19	^{59}Co(n,γ)^{60}Co	7.61	1.28	72.69	0.11	111.67 ± 20.51
20	^{nat}Ni(n,x)^{51}Cr	2.19	0.29	5.48	1.24	0.121 ± 0.033
21	^{nat}Ni(n,x)^{52}Mn	24.57	0.97	15.81	0.27	0.0710 ± 0.0060
22	^{nat}Ni(n,x)^{54}Mn	8.70	1.69	6.25	0.06	1.55 ± 0.32
23	^{nat}Ni(n,x)^{59}Fe	7.25	1.47	3.25	0.11	0.115 ± 0.025
24	^{nat}Ni(n,x)^{56}Co	130.56	20.26	70.70	0.12	4.35 ± 0.74
25	^{nat}Ni(n,x)^{57}Co	363.77	77.50	154.69	0.11	33.41 ± 7.50
26	^{nat}Ni(n,x)^{58}Co	1901.34	160.87	1123.45	0.43	63.56 ± 6.98
27	^{nat}Ni(n,x)^{60}Co	3.53	0.60	3.89	0.05	5.97 ± 1.09
28	^{nat}Ni(n,xn)^{56}Ni	27.84	3.69	14.07	0.61	0.0682 ± 0.0107
29	^{nat}Ni(n,xn)^{57}Ni	5175.19	1080.51	2686.46	15.69	3.26 ± 0.72
30	^{nat}Br(n,x)^{75}Se	2.42	0.10	0.86	0.29	0.112 ± 0.039
31	^{nat}Br(n,x)^{74}As	31.85	4.13	29.10	0.76	0.562 ± 0.084
32	^{nat}Br(n,xn)^{77}Br	7869.25	1441.62	3223.99	90.15	8.30 ± 1.65
33	^{81}Br(n,γ)^{82}Br	57491.52	11363.90	84363.84	319.85	134.05 ± 28.25
34	^{nat}Rb(n,x)^{82}Br	823.82	134.61	300.75	10.61	0.513 ± 0.093
35	^{nat}Rb(n,xn)^{83}Rb	298.73	56.28	203.30	0.46	20.31 ± 4.09

Table 5.4: Predicted average physical yields (TENDL-2017 + MCNP 6.1) as well as corresponding measurements and associated cross sections (continuing from previous page).

		Physical yield (Bq μAh^{-1} g^{-1})				Cross section (mb)
ID	Reaction	$\langle Y \rangle_{\mathrm{CALC}}$	S_{CALC}	Y_{EXP}	ΔY_{STAT}	$\langle \overline{\sigma} \rangle \pm \langle \overline{\Delta\sigma} \rangle$
36	^{nat}Rb(n,xn)^{84}Rb	2431.06	524.80	1344.75	0.96	51.07 ± 11.60
37	^{nat}Rb(n,x)^{86}Rb	4207.67	707.01	3173.59	5.22	68.43 ± 12.50
38	^{89}Y(n,x)^{83}Rb	2.54	0.10	1.23	0.11	0.129 ± 0.016
39	^{89}Y(n,x)^{84}Rb	24.19	2.53	14.89	0.36	0.592 ± 0.076
40	^{89}Y(n,x)^{86}Rb	86.36	17.09	25.33	3.38	0.569 ± 0.142
41	^{89}Y(n,4n)^{86}Y	6723.49	463.19	4040.72	219.38	3.01 ± 0.34
42	^{89}Y(n,3n)^{87}Y	9760.08	1743.48	5956.05	12.05	23.89 ± 4.59
43	^{89}Y(n,3n)^{87m}Y	44686.74	7895.39	23104.23	429.87	15.53 ± 2.97
44	^{89}Y(n,2n)^{88}Y	988.75	220.86	457.41	0.52	58.69 ± 13.75
45	^{93}Nb(n,x)^{87}Y	56.01	2.52	96.12	2.35	0.406 ± 0.036
46	^{93}Nb(n,x)^{88}Y	8.21	1.06	9.14	0.09	1.23 ± 0.18
47	^{93}Nb(n,x)^{89}Zr	135.79	5.49	157.24	1.44	0.653 ± 0.055
48	^{93}Nb(n,4n)^{90}Nb	8512.20	799.50	7175.02	75.49	5.52 ± 0.65
49	^{93}Nb(n,3n)^{91m}Nb	150.33	28.65	63.71	1.86	4.88 ± 1.00
50	^{93}Nb(n,2n)^{92m}Nb	4116.27	861.47	1880.49	1.12	24.01 ± 5.30
51	^{103}Rh(n,x)^{96}Tc	136.86	6.98	27.27	0.29	0.164 ± 0.015
52	^{103}Rh(n,p)^{103}Ru	79.64	13.30	25.81	0.22	1.41 ± 0.26
53	^{103}Rh(n,5n)^{99g}Rh	24.47	1.15	10.34	0.31	0.234 ± 0.021
54	^{103}Rh(n,4n)^{100}Rh	4692.46	613.54	5854.79	12.27	7.10 ± 1.06
55	^{103}Rh(n,3n)^{101g}Rh	7.01	1.55	4.24	0.13	7.13 ± 1.67
56	^{103}Rh(n,3n)^{101m}Rh	7776.27	1680.79	3843.71	1.90	23.25 ± 5.29
57	^{103}Rh(n,2n)^{102g}Rh	206.15	43.93	138.80	0.98	40.09 ± 9.00
58	^{103}Rh(n,2n)^{102m}Rh	33.83	7.37	93.39	0.18	177.82 ± 40.73
59	^{nat}Ag(n,x)^{105}Rh	621.10	119.31	854.91	112.52	1.84 ± 0.45
60	^{nat}Ag(n,xn)^{105}Ag	544.91	109.77	288.04	0.52	17.39 ± 3.71
61	^{nat}Ag(n,xn)^{106m}Ag	3462.34	702.80	1593.24	3.21	19.28 ± 4.14
62	^{109}Ag(n,γ)^{110m}Ag	57.96	10.06	113.20	0.25	41.30 ± 7.79
63	^{nat}In(n,x)^{110m}Ag	1.94	0.27	0.73	0.03	0.286 ± 0.046
64	^{115}In(n,p)^{115m}Cd	30.01	6.15	9.58	0.84	0.664 ± 0.155
65	^{nat}In(n,xn)^{111}In	741.90	128.10	746.55	2.34	3.26 ± 0.61
66	^{nat}In(n,x)^{114m}In	1870.03	370.62	1100.08	0.70	84.67 ± 17.81
67	^{127}I(n,x)^{120m}Sb	2.96	0.17	1.98	0.05	0.0198 ± 0.0019
68	^{127}I(n,x)^{122}Sb	91.11	12.94	49.77	8.23	0.234 ± 0.054
69	^{127}I(n,x)^{124}Sb	4.32	0.86	1.70	0.02	0.176 ± 0.037
70	^{127}I(n,x)^{123m}Te	1.47	0.05	1.98	0.05	0.410 ± 0.035

Table 5.4: Predicted average physical yields (TENDL-2017 + MCNP 6.1) as well as corresponding measurements and associated cross sections (continuing from previous page).

		Physical yield (Bq μAh^{-1} g^{-1})				Cross section (mb)
ID	Reaction	$\langle Y \rangle_{\mathrm{CALC}}$	S_{CALC}	Y_{EXP}	ΔY_{STAT}	$\langle \bar{\sigma} \rangle \pm \langle \overline{\Delta\sigma} \rangle$
71	^{127}I(n,5n)^{123}I	5454.69	266.26	2821.89	162.73	2.69 ± 0.28
72	^{127}I(n,4n)^{124}I	3168.71	408.46	2074.24	3.21	14.95 ± 2.20
73	^{127}I(n,2n)^{126}I	7054.88	1504.55	3524.25	1.74	78.30 ± 17.58
74	^{133}Cs(n,5n)^{129}Cs	2495.58	129.62	1427.20	193.97	3.46 ± 0.56
75	^{133}Cs(n,2n)^{132}Cs	13471.23	2861.71	6197.98	3.43	72.27 ± 16.17
76	^{133}Cs(n,γ)^{134}Cs	257.48	47.91	281.50	0.25	381.92 ± 76.51
77	^{141}Pr(n,x)^{139}Ce	332.91	66.63	168.37	0.13	44.26 ± 9.39
78	^{141}Pr(n,p)^{141}Ce	47.32	9.77	13.90	0.14	0.862 ± 0.188
79	^{141}Pr(n,γ)^{142}Pr	37573.27	6915.20	46179.77	913.85	70.20 ± 14.00
80	^{nat}Gd(n,x)^{156}Eu	71.54	10.88	53.46	1.20	1.73 ± 0.29
81	^{nat}Gd(n,x)^{157}Eu	1857.41	287.84	3164.81	251.38	4.28 ± 0.80
82	^{nat}Gd(n,xn)^{151}Gd	10.44	1.09	11.62	1.59	3.08 ± 0.57
83	^{nat}Gd(n,x)^{153}Gd	48.66	8.62	39.15	0.82	20.08 ± 3.85
84	^{nat}Gd(n,x)^{159}Gd	52189.16	7710.27	36248.00	94.08	59.45 ± 9.75
85	^{160}Gd(n,γ)^{161}Gd ^{161}Gd$\rightarrow^{161}$Tb	3837.59	681.99	1940.23	22.51	28.46 ± 5.49
86	^{169}Tm(n,5n)^{165}Tm	6786.34	586.58	2582.15	5.98	7.45 ± 0.83
87	^{169}Tm(n,3n)^{167}Tm	5420.62	1193.39	2923.23	18.64	61.85 ± 14.30
88	^{169}Tm(n,2n)^{168}Tm	939.32	187.54	435.92	0.39	92.87 ± 19.66
89	^{181}Ta(n,p)^{181}Hf	14.98	3.04	4.51	0.31	0.469 ± 0.106
90	^{181}Ta(n,5n)^{177}Ta	6035.61	693.15	3281.67	47.79	19.05 ± 2.58
91	^{181}Ta(n,γ)^{182}Ta	2915.95	529.23	2351.63	9.05	660.77 ± 130.26
92	^{197}Au(n,x)^{192}Ir	1.37	0.19	0.64	0.12	0.126 ± 0.031
93	^{197}Au(n,4n)^{194}Au	13649.98	2464.83	7071.54	40.49	29.94 ± 5.81
94	^{197}Au(n,3n)^{195}Au	255.70	58.26	52.17	1.00	25.87 ± 6.19
95	^{197}Au(n,2n)^{196}Au	11655.06	2335.41	5867.86	2.52	96.54 ± 20.50
96	^{197}Au(n,γ)^{198g}Au	80292.29	14818.68	90171.43	36.47	647.73 ± 129.02
97	^{nat}Tl(n,x)^{203}Hg	31.21	4.86	9.13	0.10	1.181 ± 0.202
98	^{nat}Tl(n,xn)^{200}Tl	5584.78	580.68	2897.74	17.57	8.77 ± 1.11
99	^{nat}Tl(n,xn)^{201}Tl	5644.75	929.32	2537.86	20.40	21.42 ± 3.84
100	^{nat}Tl(n,xn)^{202}Tl	3416.30	661.94	1305.70	0.68	44.53 ± 9.18
101	^{209}Bi(n,6n)^{204}Bi	5263.39	245.72	1081.13	83.81	1.45 ± 0.17
102	^{209}Bi(n,5n)^{205}Bi	765.85	69.91	210.97	0.52	9.20 ± 1.06
103	^{209}Bi(n,4n)^{206}Bi	4028.77	718.45	1396.62	1.55	24.72 ± 4.74
104	^{209}Bi(n,3n)^{207}Bi	4.08	0.93	5.28	0.02	172.02 ± 41.14

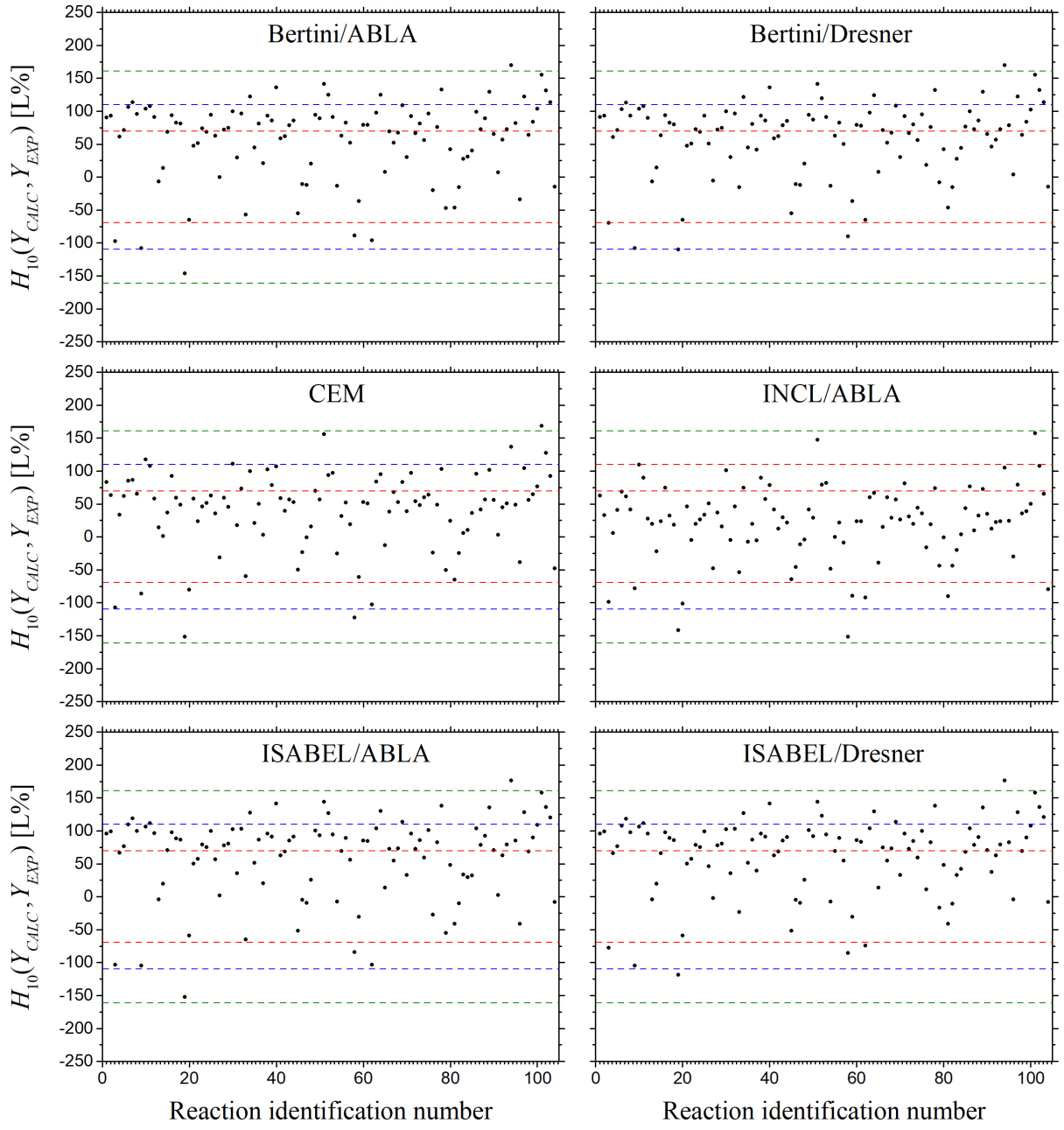


Figure 5.3: Logarithmic percentage difference between calculated and measured physical yields (solid symbols), plotted versus the reaction ID number, for the different MCNP 6.1 physics selections used in calculating the neutron flux. The cross sections were taken from the TENDL-2015 library. The horizontal lines indicate factors of 2, 3 and 5 actual difference between the two yields. See also caption to Fig. 5.2.

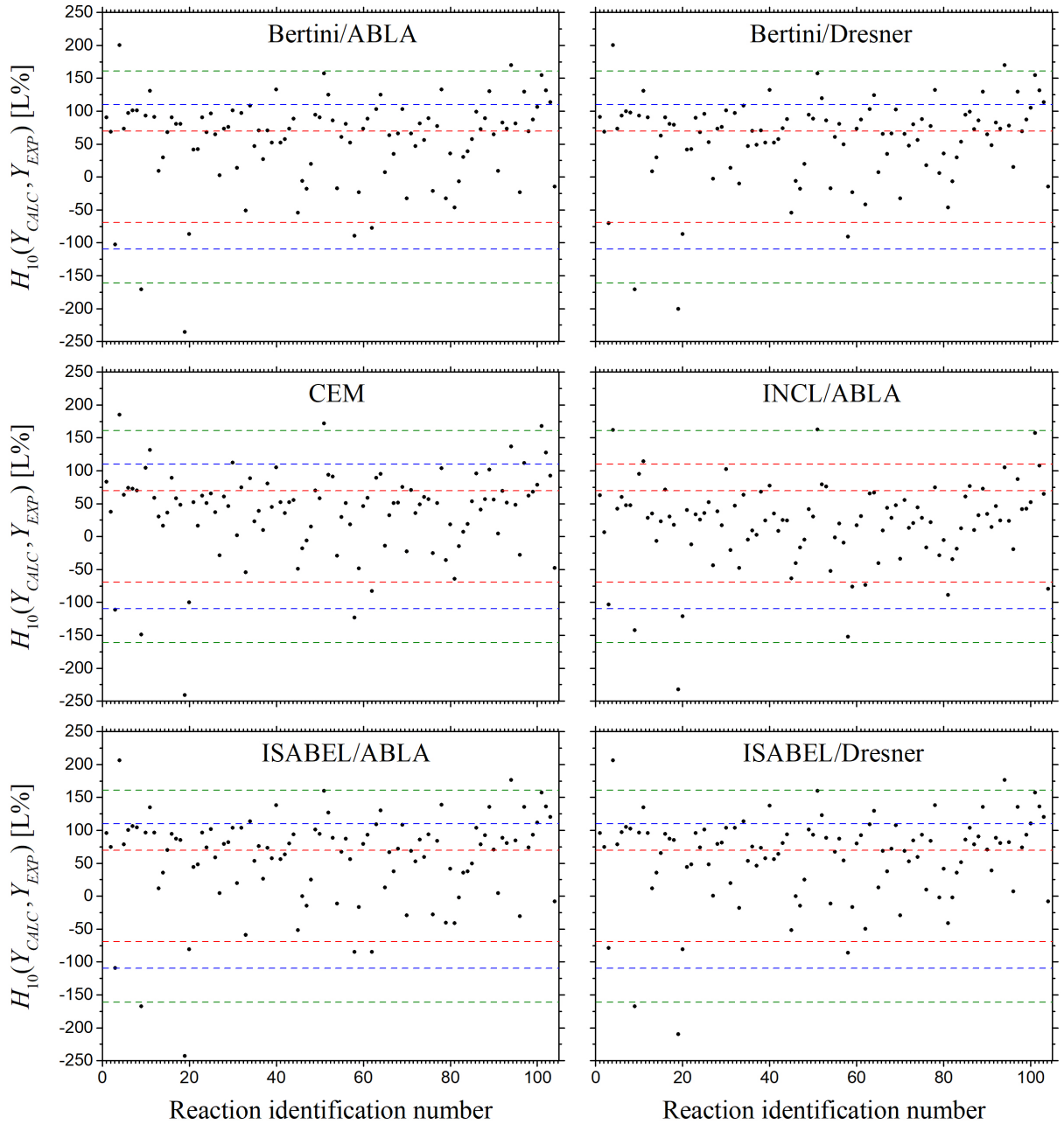


Figure 5.4: Logarithmic percentage difference between calculated and measured physical yields (solid symbols), plotted versus the reaction ID number, for the different MCNP 6.1 physics selections used in calculating the neutron flux. The cross sections were taken from the TENDL-2017 library. The horizontal lines indicate factors of 2, 3 and 5 actual difference between the two yields. See also caption to Fig. 5.2.

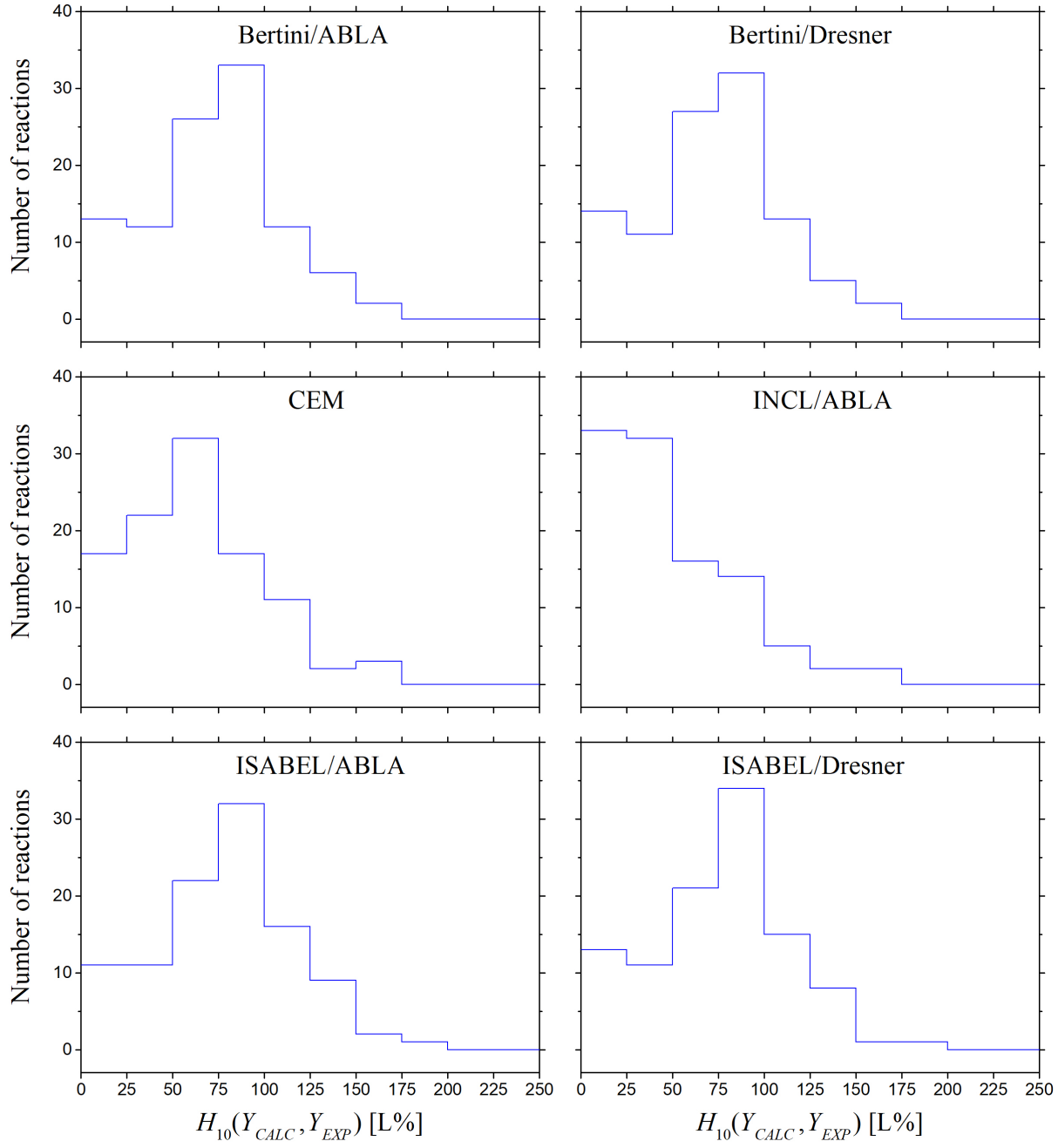


Figure 5.5: Number of reactions versus the absolute value of the logarithmic percentage difference between calculated and measured physical yields, plotted as a histogram, for the different MCNP 6.1 physics selections used in calculating the neutron flux. The cross sections used in the calculations were taken from the TENDL-2015 library.

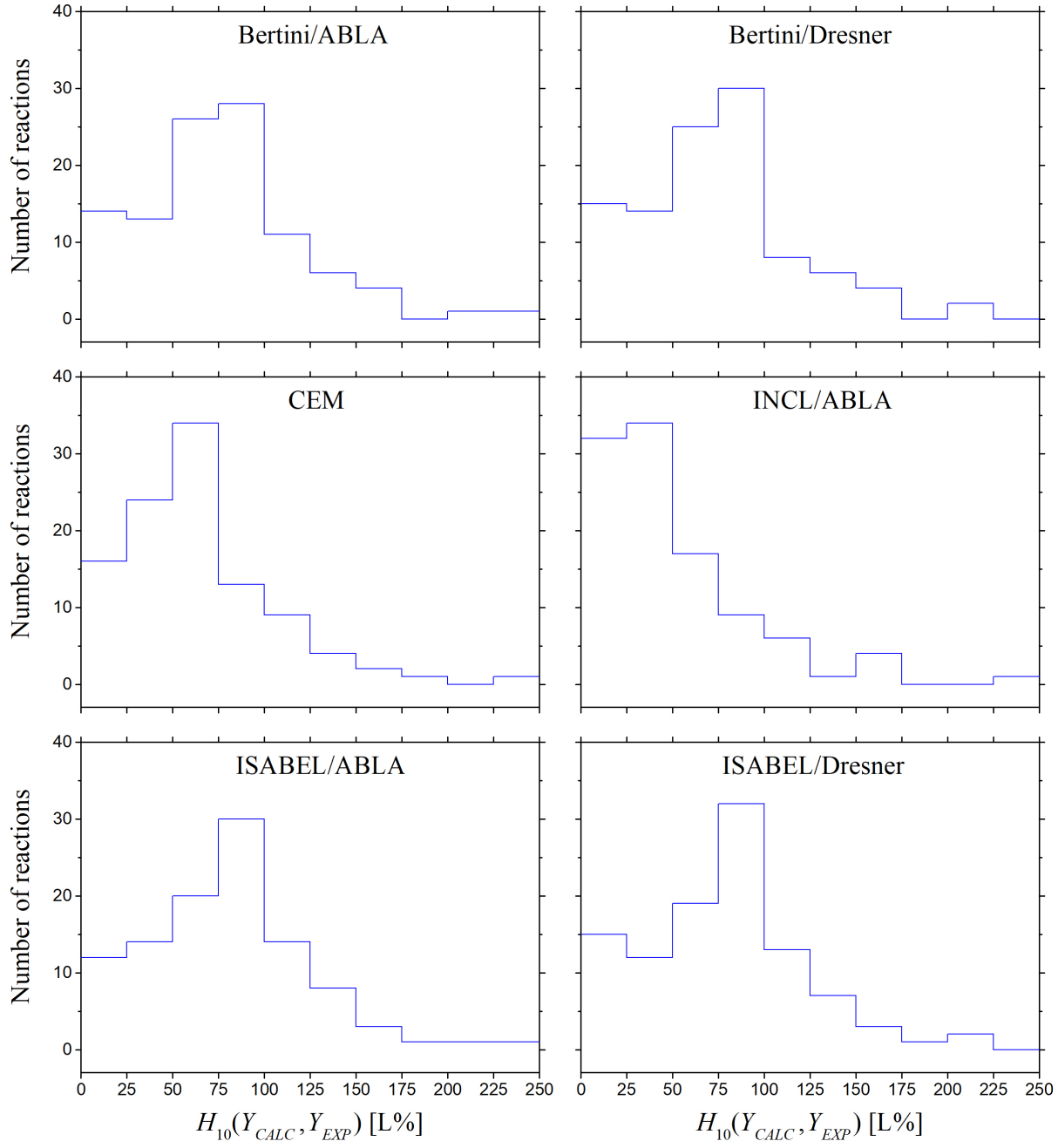


Figure 5.6: Number of reactions versus the absolute value of the logarithmic percentage difference between calculated and measured physical yields, plotted as a histogram, for the different MCNP 6.1 physics selections used in calculating the neutron flux. The cross sections used in the calculations were taken from the TENDL-2017 library.

Table 5.5: Average (of all 104 reactions) percentage difference, log percentage difference and their associated standard deviations of calculated and measured physical yields, for each MCNP 6.1 physics selection, utilizing cross sections from the TENDL-2015 and TENDL-2017 libraries, respectively.

	:::::: TENDL-2015 ::::::			
Physics selection	$H_5(Y_{CALC}, Y_{EXP})$		$H_{10}(Y_{CALC}, Y_{EXP})$	
	Average (%)	Standard deviation (%)	Average (L%)	Standard deviation (L%)
Bertini/ABLA	51.50	55.64	55.58	61.17
Bertini/Dresner	54.21	51.36	58.47	56.30
CEM	37.53	54.12	39.76	59.14
INCL/ABLA	19.76	51.51	20.43	55.84
ISABEL/ABLA	54.54	56.98	59.21	63.05
ISABEL/Dresner	57.27	52.54	62.15	57.97

	:::::: TENDL-2017 ::::::			
Physics selection	$H_5(Y_{CALC}, Y_{EXP})$		$H_{10}(Y_{CALC}, Y_{EXP})$	
	Average (%)	Standard deviation (%)	Average (L%)	Standard deviation (L%)
Bertini/ABLA	50.55	58.62	54.28	67.62
Bertini/Dresner	53.24	55.05	57.27	63.08
CEM	36.75	56.72	38.64	64.98
INCL/ABLA	19.08	54.37	19.39	61.53
ISABEL/ABLA	53.58	59.81	57.90	69.42
ISABEL/Dresner	56.31	56.02	60.95	64.65

Table 5.6 shows the actual numbers of reactions where the calculated predictions are within a factor of either 2, 3 or 5 from the corresponding measured values. For the sake of argument, we will assume the sample size of 104 reactions to be large enough to make some statements on the predictive power of the methods used. Roughly, one can say that with Bertini/ABLA, Bertini/Dresner, ISABEL/ABLA and ISABEL/Dresner it seems that less than 50% of predictions can be expected to be within a factor of 2. At least, this will be our expectation until a larger sample proves otherwise. In contrast, with the CEM physics selection about 2 out of 3 yield predictions can be expected to be within a factor of 2 and with INCL/ABLA these numbers are 3 out of 4. With both INCL/ABLA and CEM one can expect a prediction within a factor of 3 most of the time, while differences larger than a factor of 5 are very rare.

In future studies on neutron activation of samples behind a VBTS target (bombarded with a 66 MeV proton beam) we will likely only use the CEM and INCL/ABLA physics selections for calculating the neutron spectrum, for use in prior predictions of the physical yields.

Table 5.6: Number of reactions having differences between calculated and measured physical yields smaller than the factor indicated, for each MCNP 6.1 physics selection, utilizing cross sections from the TENDL-2015 and TENDL-2017 libraries, respectively.

Physics selection	TENDL-2015			TENDL-2017		
	< factor 2	< factor 3	< factor 5	< factor 2	< factor 3	< factor 5
Bertini/ABLA	45	90	103	45	89	100
Bertini/Dresner	44	91	103	45	89	100
CEM	69	96	103	68	92	100
INCL/ABLA	77	100	104	79	96	101
ISABEL/ABLA	39	88	103	39	87	100
ISABEL/Dresner	40	88	103	40	87	100
Average	53	92	104	57	90	101

5.3.2 Average neutron spectrum and yield outliers

The amount of physical yield data generated in this study is quite extensive. It proved to be complicated to get a complete overview of 104 reactions at the same time, especially if there are 12 such data sets (from 6 physics selections and 2 cross-section data libraries). Also, one would like to look more closely at the outliers in order to see whether there are perhaps any patterns, e.g. whether the same type of reactions shows an over or underestimation, whether some mass region appears more problematic than others, etc. It is already clear that the INCL/ABLA and CEM physics selections give a better overall agreement than the others. In other words, these two selections have fewer outliers. One can therefore argue that from an outlier point of view, one should rather study the worst case. Alternatively, one can study the average case. In fact, we looked at several such scenarios. What we chose to present next is a closer look at the outliers obtained when using the average neutron spectrum (i.e. the average of the 6 neutron spectra obtained from all 6 physics selections) in the calculated predictions, focusing initially only on those cases where the differences between calculated and measured physical yields exceed a factor of 3. This was done separately for the TENDL-2015 and TENDL-2017 data sets of this work. Before looking at these results, however, it also makes sense to compare the TENDL-2015 and TENDL-2017 predictions directly with each other.

Figure 5.7 shows the log percentage differences between physical yields derived from the TENDL-2015 and TENDL-2017 cross sections, using the average neutron spectrum in the respective calculations. It is clear that the general agreement is quite reasonable but there are some exceptional cases, in particular the reactions with numbers 4, 9, 19, and 70, which show a log percentage difference larger than 50L%. For these cases we scrutinized the TENDL data and our calculations to make sure that there were not errors in the analysis. Suffice it to say that whatever errors found have been fixed but the above four reactions remained outliers. Reaction no. 4 is ^{nat}Ti(n,x)^{47}Ca, in which case quite large differences are evident between TENDL-2015 and TENDL-2017 cross sections for the target nucleus ^{48}Ti. Reaction no. 9 is ^{55}Mn(n,x)^{48}V, where the TENDL-2015 and TENDL-2017 excitation functions have similar

shapes but peak at different maxima. Reaction no. 19 is the capture reaction ^{59}Co(n,γ)^{60}Co. In this case the TENDL-2015 and TENDL-2017 cross sections are similar at most of the listed energies except in the thermal region, where up to an order of magnitude difference is observed. Reaction no. 70 is ^{127}I(n,x)^{123m}Te, where once again the observed differences are related to differences in the two TENDL libraries. The average log percentage difference of all the values shown in Fig. 5.7 is only 1.2L%, i.e. rather close to zero. This is a small value, thus from an overall perspective, the average overprediction relative to the measured data is similar for the two libraries.

Figures 5.8 and 5.9 show the log percentage differences between calculated average and measured physical yields, pertaining to the TENDL-2015 and TENDL-2017 libraries, respectively. With the TENDL-2015 data, there are 12 outliers exceeding a factor of 3 (reactions with ID numbers 19, 34, 40, 51, 52, 64, 78, 89, 94, 97, 101 and 102). With the TENDL-2017 data, there are 14 such outliers (reactions with ID numbers 4, 9, 11, 19, 40, 51, 52, 64, 78, 89, 94, 97, 101 and 102). These values represent almost the entire mass region of the study. One cannot distinguish any region in mass where one can say with certainty that the agreement is notably better or notably worse. Eleven of the outliers are common to the TENDL-2015 and TENDL-2017 data sets. Of these, four are (n,p) reactions. There are only five (n,p) reactions in this study, all of them overpredicted. There is only one (n,γ) reaction amongst these outliers, which is somewhat of a surprise. In fact, there are twelve (n,γ) reactions in this study or cases where an (n,γ) reaction notably contributes to the yield. In ten of these cases the predictions are reasonable. One also cannot identify particular target nuclei for which the predicted residue

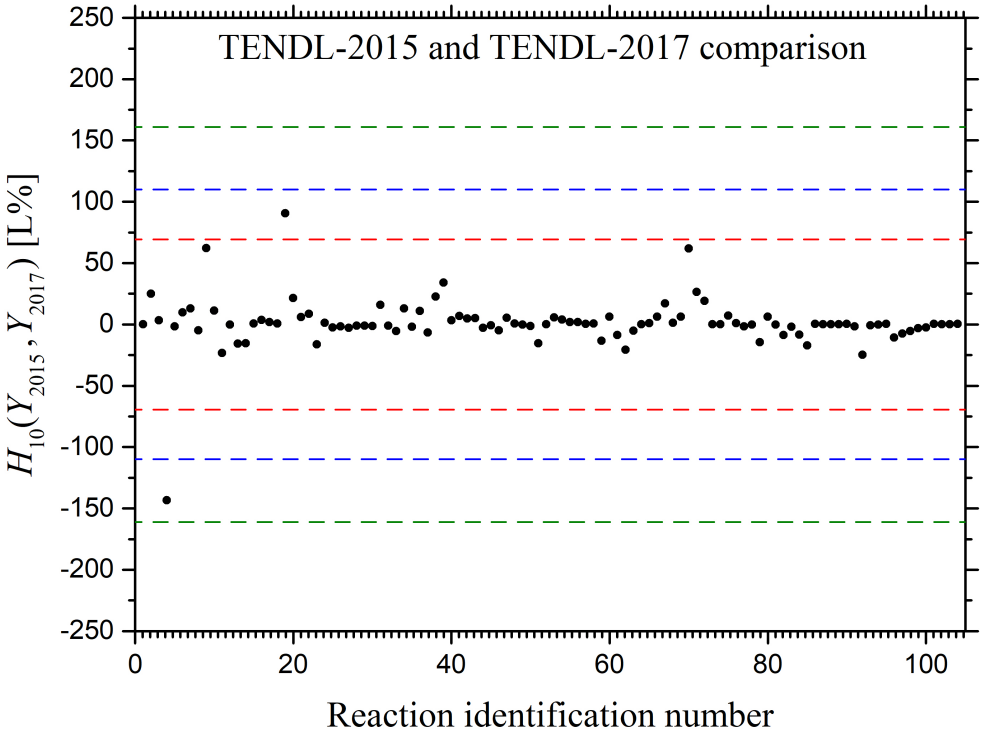


Figure 5.7: Logarithmic percentage difference between calculated physical yields according to the TENDL-2015 and TENDL-2017 cross sections, plotted versus the reaction ID number, for the case where an average spectrum has been adopted for the neutron flux. The horizontal lines indicate factors of 2, 3 and 5 of actual difference between the two yields. See also caption to Fig. 5.2.

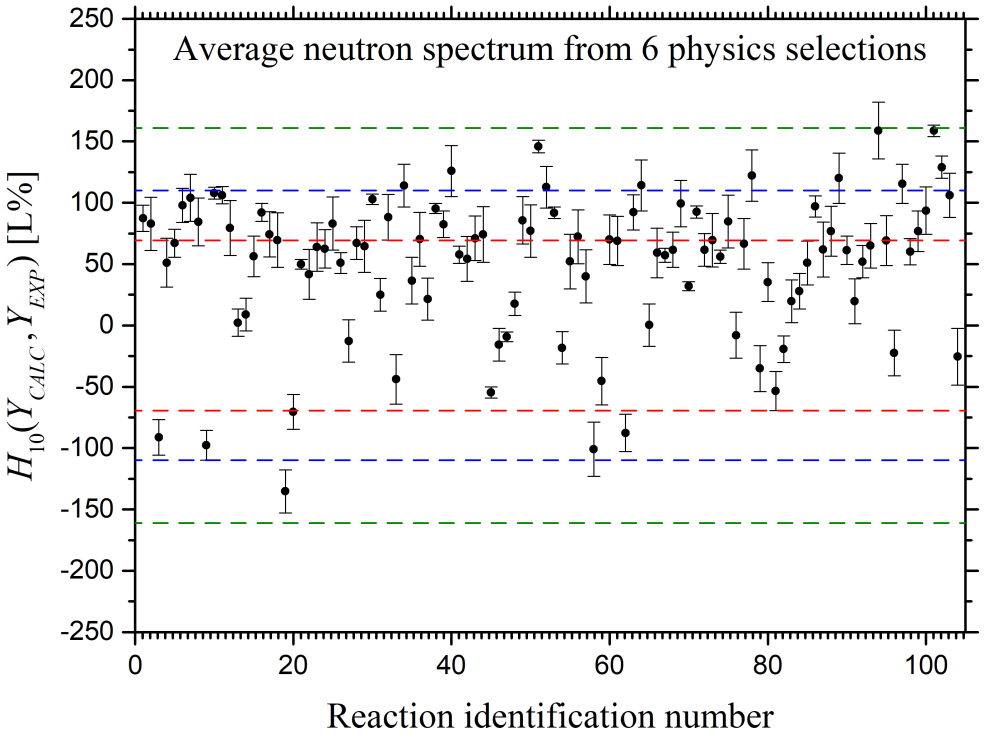


Figure 5.8: Logarithmic percentage difference between calculated and measured physical yields, the former derived from TENDL-2015 cross sections, plotted versus the reaction ID number, for the case where an average spectrum has been adopted for the neutron flux. The horizontal lines indicate factors of 2, 3 and 5 actual difference between the two yields. See also caption to Fig. 5.2.

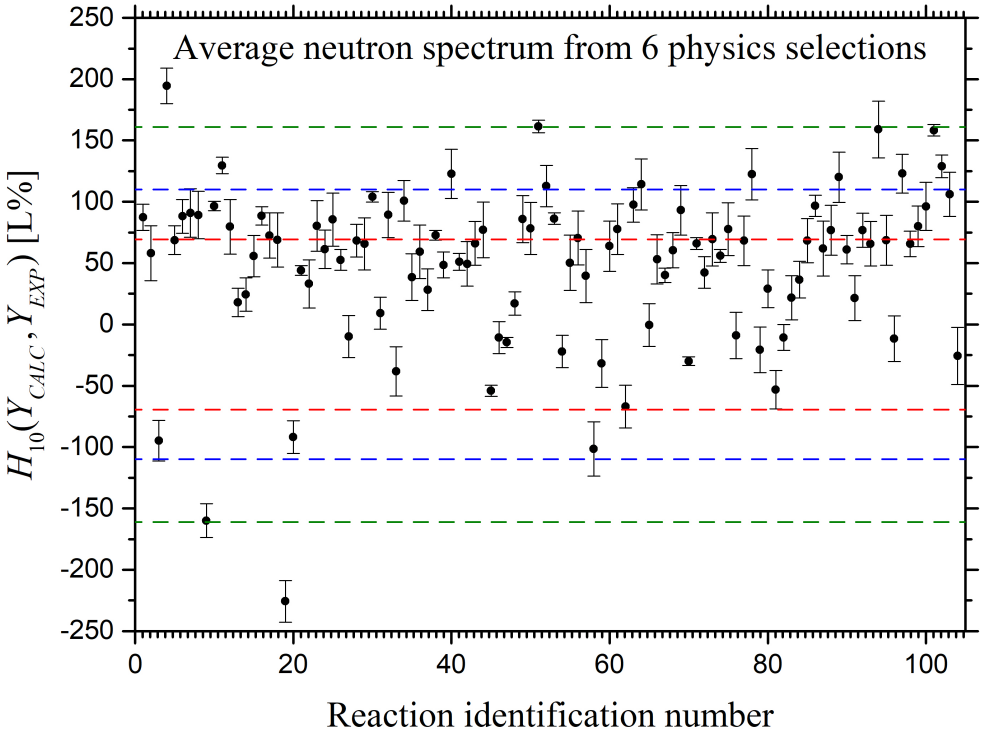


Figure 5.9: Logarithmic percentage difference between calculated and measured physical yields, the former derived from TENDL-2017 cross sections, plotted versus the reaction ID number, for the case where an average spectrum has been adopted for the neutron flux. The horizontal lines indicate factors of 2, 3 and 5 the actual difference between the two yields. See also caption to Fig. 5.2.

yields seem particularly problematic. One observes reasonable predictions for other residues on those targets that contain outliers.

This study has shown that the neutron flux behind a VBTS target is generally too low for producing the observed radionuclides on a commercial scale. Several radionuclides, however, can be successfully produced for research-scale applications, e.g. for chemical labeling studies and *in vitro* radiobiology investigations. It is worth identifying those radionuclides that have application potential and can be successfully produced with secondary neutrons. Here one will typically look at those that have a different atomic species than the activated materials, in order for them to be chemically separable from the targets. Their half-lives should ideally be several days to several tens of days as these targets can be in a bombardment station for several days. Furthermore, the typical yield should be at least several milli-Curie to several tens of milli-Curie per production. Several of the radionuclides investigated in this work have such premises. Six of them were selected to look at more closely, namely ^{46}Sc, ^{59}Fe, ^{103}Ru, ^{141}Ce, ^{161}Tb and ^{203}Hg. In Appendix A their current-day uses are discussed briefly.

Chapter 6

Summary and Conclusions

The thesis described a small activation chamber that was specially built for this study, which could be located in the pusher assembly of the vertical-beam target station (VBTS) at iThemba LABS. This allowed a set of samples to be activated with secondary neutrons directly behind a VBTS production target. The experiment was performed in a commensalistic mode in conjunction with a routine radionuclide production bombardment, during which the target received an accumulated charge of 20 000 μAh at a nominal beam current of 220 μA. The 66 MeV proton beam, which was not continuous but intermittent, was logged in 1 second intervals. As the bombardment stretched over several days, the focus was on the production of relatively long-lived radionuclides. The activated samples covered a large mass region and consisted of 22 different materials ranging from ^{7}Be to ^{209}Bi. After bombardment, the samples were assayed for their gamma-ray emissions by means of an HPGe detector. Physical yields were subsequently derived for 104 identified reaction products.

Predictions of the physical yields required a knowledge of the neutron flux in the activation chamber. This was obtained from Monte Carlo simulations with the well-known radiation transport code MNCP 6.1, utilizing 6 different physics selections. Yield predictions were based on evaluated cross sections for neutron-induced reactions according to the TENDL-2015 and TENDL-2017 nuclear data libraries, in conjunction with the neutron flux values obtained from the MCNP simulations. The differences in the yield results obtained with the different physics selections were treated as an additional source of uncertainty in the effective cross sections derived for the observed reaction products.

It proved non-trivial to compare the experimental yields of 104 reaction products with the predictions based on 6 different physics selections and cross sections from two different nuclear data libraries, especially in a graphical way. It proved useful to assign an identification number (ID number) to each of the 104 reactions (or nuclear processes) and to plot various "indicators of relative difference" versus this ID number. The logarithmic percentage difference was found to be most useful for the purpose of comparing the relatively large body of measured yields with the various predicted values. A quite lengthy discussion was presented to motivate this choice amongst other possibilities. While there clearly are differences between results based on the TENDL-2015 and TENDL-2017 libraries, the overall level of agreement that the two sets of predictions showed with the experimental values was found to be rather similar.

With the Bertini/ABLA, Bertini/Dresner, ISABEL/ABLA and ISABEL/Dresner physics se-

lections, it seems like less than 50% of predictions can be expected to be within a factor of 2 of the measured values. With the CEM physics selection, the situation improves to about 2 out of every 3 predictions to be within a factor of 2. With the INCL/ABLA choice, the number further improves to about 3 out of 4. From the point of view of the present study, the INCL/ABLA physics selection gives the best agreement. When looking at outliers beyond a factor of 3 from the measured values, 12 cases were found in the TENDL-2015 data set and 14 in the TENDL-2017 data set. Eleven cases were common to both sets. Outliers beyond a factor of 5 difference seem to be very rare. It is possible, however, that the sample of 104 reaction products may be too small to make very firm statements concerning the predictive power in general. There seems to be an indication that (n,p) reactions are more often over-predicted than more complex reactions but the sample size needs to be enlarged to prove this convincingly. It should be stressed that the sometimes large differences between predictions and measurements cannot be ascribed to deficiencies in the TENDL libraries only as there are many uncertainties, e.g. in the Monte Carlo simulations and also the measurements. We simply report our findings, realizing that more extensive experimental results are required to make better judgements. Activation studies with quasi-monoenergetic neutrons (QMN) may be very useful but unfortunately such facilities are few in this energy region. iThemba LABS is fortunate that it has such a facility and future studies with QMN are in fact planned.

Several of the radionuclides observed in the neutron-activated samples have proven value in various applications. A selection of them have been discussed, namely ^{46}Sc, ^{59}Fe, ^{103}Ru, ^{141}Ce, ^{161}Tb and ^{203}Hg. While the production rates are generally low, it is clear that sufficient quantities can be produced to support the needs of some experimental projects. Laboratory scale production rather than semi-commercial or commercial-scale production therefore seems to be more realistic with the available secondary neutron flux at a 70 MeV cyclotron facility.

Appendix A

Selected Applications

Six radionuclides of general interest in the radio-medical community are discussed here from a non-historical perspective, taking into account only the most recent directions in those fields. This is to show why research on the exploitation of secondary neutrons is beneficial for mankind and should be pursued.

A.1 SCANDIUM-46

The radionuclide ^{47}Sc was proposed as a potential therapeutic partner to the PET radionuclide ^{44}Sc (see e.g. [MÜL2014, DOM2017] and references therein). Its incorporation into peptide-based targeting ligands with a relatively fast blood clearance as well as its use in radioimmunotherapy has been proposed. Unfortunately, both ^{44}Sc and ^{47}Sc have limited availability at the present time. The longer-lived ^{46}Sc ($T_{1/2}$ = 80.3 d) is more readily available and has been reported to be ideal for assessing the chemistry, stability and biodistribution of labeled antibody conjugates [MOG2012] as well as labeled macrocyclic ligands [SET2018].

Scandium-46 has also found application in *radioactive particle tracking* experiments (the so-called RPT technique) by being incorporated into microspheres. These can be either scandium oxide (Sc_2O_3) microspheres [BIS2016] or glass microspheres [REH1999]. It has emerged as a powerful noninvasive technique for flow visualization of solid and liquid phases in multiphase flow systems, for example those found at large chemical engineering plants. Fluidized beds are important in many other industries too, e.g. hydrometallurgy, food technology, biochemical processing, water treatment, etc. Radionuclide particle tracking with microspheres offers a quantitative technique to study hydrodynamic characteristics in such systems.

A.2 IRON-59

The hematopoietic system is the system of organs and tissues, including the bone marrow, spleen, thymus and lymph nodes, involved in the production of cellular blood components. The heme group in hemoglobin contains iron in its molecular structure, through which ionic bonding with oxygen provides the means to transport oxygen from the lungs to all other cells in the body. The radioisotope ^{59}Fe has been used extensively as a tracer for the purpose of studying the ferrokinetics in red blood cells and the diagnosis of a variety of hematologic

disorders. *In vivo* studies with ^{59}Fe on humans were widespread in the 1950s and 1960s and even into the 1970s. These investigations did not only involve people with disease but also healthy individuals, in order to study the bioavailability and uptake of iron in nutrition and the many complex processes involved with iron metabolism in the body. A 1970 article by Palmer et al. [PAL1970] on a new dedicated whole-body counting system for ^{59}Fe summarizes this era beautifully, stating in the first sentence of their Introduction that "During the past two decades, ^{59}Fe has been used extensively to measure body iron exchange in man".

The attitudes and practice surrounding *in vivo* diagnostic investigations on humans using long-lived radionuclides, such as ^{59}Fe, have changed over the years. A 1994 International Atomic Energy Agency (IAEA) Bulletin [PAR1994] makes the following two statements: (1) "Isotope techniques provide the only direct way for measuring iron uptake and bioavailability and are correctly regarded as as a kind of 'gold standard' for iron studies in humans"; (2) "More recently, in some countries, the use of stable isotopes (iron-54, -57 and -58) measured by mass spectrometry has come to be regarded as a preferable technique because of the absence of a radiation dose, which therefore permits studies to be made on children and pregnant women." At the turn of the century, an overview of the field of hematology was published by Lichtman et al. [LIC2000]: "Hematology: Landmark Papers of the Twentieth Century". On page 787 of that work one can find the rather curious statement: "The use of radiolabeled iron for ferrokinetics or marrow imaging is now unfortunately only of historical interest since iron-59 is no longer available for clinical use." This statement was probably made in the context of the USA and not the whole world, nevertheless, it does communicate a clear shift in procedure.

The use of ^{59}Fe for *in vitro* human studies and both *in vivo and in vitro* animal studies has remained important, however. One can also find plentiful examples of its use in agriculture, drug discovery and nutrition in the literature. Some recent examples include ^{59}Fe use in anti-tumour drug studies in rats [WAN2014] and as a tracer to study iron uptake in sorghum [DAD2013]. In the context of dual-imaging modalities, Hoffman et al. [HOF2014] investigated intrinsically radiolabeled [^{59}Fe]iron oxide nanoparticles for dual *single photon emission computed tomography* and *magnetic resonance imaging* (SPECT/MRI) in a proof-of-concept study. Superparamagnetic iron oxide nanoparticles (SPIONs) are established MRI contrast agents because of their magnetic properties and low toxicity. Combined with a gamma-emitting radioisotope of iron, SPECT is possible at the same time. In this regard, we would like to comment that ^{52}Fe may be more favourable for *in vivo* human studies due to its shorter half-life ($T_{1/2} = 8.27$ h). This was, in fact, suggested by Medvedev et al. [MED2012] but in the context of dual PET/MRI, however, ^{52}Fe also has a gamma-ray of 168.69 keV (99.1%), very suitable for SPECT.

It is interesting to return again to the matter of ^{59}Fe use in *in vivo* studies on humans. In spite of objections in recent years in some countries, such studies still happen in others. A 2016 study by Pizarro et al. [PIZ2016] investigated non-heme iron uptake in 45 women aged between 35 and 45 years, in which beef products were labeled with both ^{55}Fe and ^{59}Fe before being consumed. In this case, approval was given by the Bioethics Committee of the Institute of Nutrition and Food Technology of the University of Chile as well as the Bioethics Advisory Committee of the National Fund for Science and Technology of Chile. All subjects gave their written consent. In another 2016 study, the intravenous iron pharmaceuticals Monofer and

Cosmofer, used in the treatment of anaemia, were labeled with ^{59}Fe for the purpose of tracing iron absorption *in vivo* [JEN2016].

To conclude this discussion on ^{59}Fe, one should keep in mind that literally thousands of different enzymes require iron for its biochemical functionality. One can therefore expect that this radionuclide will remain important in research, particularly in animal studies, agriculture and various *in vitro* procedures, taking into account how vital iron is is in all forms of life.

A.3 RUTHENIUM-103

In recent years, a large international effort is underway to develop the field of targeted radiotherapy, with the aim to exploit specific radiopharmaceuticals that can selectively transport suitable radionuclides to tumoral cells while sparing healthy cells. This requires suitable bioconjugates that target specific receptors which are overexpressed on the cancer cells. By labeling these biomolecules with suitable radionuclides, one can design radioconjugates suitable for cancer treatment [PER2017].

Low-energy electron emitters have potential in the treatment of cancer with metastatic spread and/or the treatment of small tumours. Auger/Coster-Kronig electrons have low energy and short ranges (on the nanometer scale) in tissue [MAS2017], which is typically less than the diameter of a cell. It is therefore important that the targeting agent is internalized by the malignant cell. The decay of a suitable Auger emitter inside a cell has the potential to induce double strand breaks (DSB) in the DNA, rendering the cell unable to repair the damage. Double strand breaks normally lead to cell death.

Bernhardt et al. [BER2001] performed the first systematic study to identify the most suitable Auger emitters for the treatment of very small tumours. Based on a range of selection criteria that they formulated, only five radionuclides were found that fulfill all the criteria, namely ^{58m}Co, ^{103m}Rh, ^{119}Sb, ^{161}Ho and ^{189m}Os. Only one of these can be provided by a generator, namely ^{103m}Rh. The radionuclide ^{103}Ru ($T_{1/2}$ =39.247 d) is therefore important as it is the precursor of ^{103m}Rh ($T_{1/2}$ =56.12 min) with the longest half-life. Ruthenium-103 is normally reactor produced [KNA2016], however, Mastren et al. [MAS2017] reported the production of ^{103}Ru as a by-product in the bombardment of ^{232}Th targets for ^{225}Ac production with a 100 MeV proton beam. These authors chemically separated the fission-produced ^{103}Ru and found its quality to be sufficient for ^{103}Ru/^{103m}Rh generators.

A.4 CERIUM-141

Cerium oxide nanoparticles (CONP) is becoming increasingly important in the emerging field of nanomedicine. Yang et al. [YAN2013] make the statement that nanomedicine platforms can enable targeted delivery of imaging agents and therapeutic agents (thernostics) to cancerous tissue, thus serving as effective “drug delivering vehicles” with the potential of site-specific drug release. These authors also report that a potential application of CONP is to quench *reactive oxygen species* (ROS) in biological systems, thus it has unique properties as a free radical scavenger. It therefore has the potential to protect healthy cells against oxidative damage, e.g. during chemotherapy or other treatments, with a possible future application to provide

in vivo radio-protection during radiotherapy. The regenerative free radical scavenging properties of CONP is provided by its large surface area with an abundance of free oxygen vacancies [SOL2015]. In addition to its potent antioxidant activity, CONP is also a promising sunscreen component due to its ability to block broad-spectrum UV radiation.

Nanoparticles, in general, lack *in vivo* detection capability and quantitative and/or tomographic imaging, unless they are labeled with a suitable radionuclide. Consequently, ^{141}Ce is regularly used to label CONP for *in vivo* studies on rats or other animals [MOL2014], in particular for studies of CONP bioavailability, biodistribution, cell uptake, pharmacokinetics, toxicology, etc. Its 145.4 keV (48.4%) γ-ray is ideal for SPECT.

Cerium-141 is normally produced via the reaction ^{140}Ce(n,γ)^{141}Ce at a nuclear reactor. A no-carrier-added and much purer product can be obtained with the ^{141}Pr(n,p)^{141}Ce reaction but requires fast neutrons.

A.5 TERBIUM-161

The importance of ^{161}Tb can only be described by discussing another radionuclide first, namely ^{177}Lu. Lutetium-177 has become an important radionuclide in a particular branch of targeted radionuclide therapy, namely *peptide receptor radionuclide therapy* (PRRT). PRRT has already been an established clinical modality for the treatment of so-called *neuroendocrine tumours* (NETs) for more than a decade. Neuroendocrine cells are distributed throughout the body but about 75% of NETs develop in the gastroenteropancreatic system [BAU2015]. These tumours are very heterogeneous in nature and lack therapeutic options. Fortunately, most tumorous neuroendocrine cells exhibit an overexpression of the so-called somatostatin receptors on the cell surface and can be preferentially targeted with certain peptides that accumulate at these receptor sites. The basis of PRRT is receptor-mediated internalization and intercellular retention of radiolabeled peptides, utilizing radionuclides with low-energy β^- emissions that can deliver a fatal radiation dose on a cellular scale. Amongst the possible candidates, ^{177}Lu has been described as the "rising star for therapy" [KÖS2017]. Lutetium-177 is produced in nuclear reactors by means of the ^{176}Yb(n,γ)^{177}Yb$\rightarrow$^{177}Lu nuclear process on a commercial scale, with high specific activity and chemical purity [LEH2011]. Thus, ^{177}Lu-labeled radiopharmaceuticals have become important in clinical nuclear oncology and an active area of research.

An important investigation was performed by Lehenberger and co-workers [LEH2011] on ^{161}Tb as an alternative to ^{177}Lu for targeted radionuclide therapy. They pointed out that ^{161}Tb is very similar to ^{177}Lu with respect to half-life, beta energy and chemical properties, however, ^{161}Tb also emits a significant amount of low-energy conversion and Auger electrons. Greater therapeutic effect can therefore be expected in comparison to ^{177}Lu. In addition, ^{161}Tb has a suitable γ-line of 75 keV for SPECT imaging. Furthermore, the large-scale production of high-purity ^{161}Tb is less costly than in the case of ^{177}Lu, utilizing the ^{160}Gd(n,γ)^{161}Gd$\rightarrow$^{161}Tb nuclear process in a reactor. Subsequent pre-clinical trails have produced very encouraging results.

Concerning the radionuclides of terbium, an interesting article was published by CERN in the January 2013 issue of the CERN Courier [CERN2013]. The title was 'Terbium: a new "Swiss army knife" for nuclear medicine. The article explained the importance of "matched pairs" of diagnostic and therapeutic radionuclides of the same element, in the prior diagnostic

preparation and subsequent treatment, using radiopharmaceuticals that are absorbed and distributed in identical ways in the body. Terbium is unique as it is the only element in the periodic table to offer not just a pair but a quadruplet of clinically interesting radionuclides with complementary characteristics covering all the options for nuclear medicine: ^{152}Tb for PET, ^{155}Tb for SPECT, ^{149}Tb for alpha-particle therapy and ^{161}Tb for therapy with electrons (β^-, conversion and Auger electrons). With current technology, only ^{161}Tb can be produced in viable commercial quantities but is not inconceivable that this situation might change in future, depending on the results of present and future preclinical and clinical studies. Thus, the radionuclides of terbium is something to watch with interest as the future unfolds.

A.6 MERCURY-203

Mercury is an element that is highly toxic, a property shared with several other heavy metals such as cadmium and lead. Unlike these last two, however, mercury is volatile at room temperature and poses a significant risk of respitory exposure by inhalation [SYV2012, ROO2012]. Dermal exposure can also be significant as mercury is readily absorbed by the skin, e.g. from cosmetics or by improper handling in certain industrial processes [MOO2009]. The most significant risk, however, is dietary intake as mercury is readily taken up and concentrated in the human food chain, e.g. by fish and other seafood [OLI2015]. Contamination of water resources due to mining and/or other industrial processes can be very problematic as uptake by certain algae and plankton can lead to a significant mercury concentration early in the food chain, subsequently consumed by fish and finally by humans [KAR2007]. The radionuclide ^{203}Hg is an important radiotracer for studying the toxicokinetics of mercury in organisms and in the environment. The different toxic effects of mercury are numerous and serious.

Mercury readily crosses the blood-brain barrier (BBB) and accumulates in the brain [OLI2015]. Toxic exposure can lead to Amyotrophic Lateral Sclerosis (ALS) and other neurodegenerative disorders [ROO2012]. It also readily crosses the placenta of pregnant females and accumulates in the fetus, which can lead to retarded neurological and brain growth, or even fatality in severe exposures. Other toxicological consequences include the renal, hepatic, cardiovascular and reproductive systems. A complication of mercury poisoning is that the onset of symptoms may be delayed after an initial acute or toxic exposure. This “latent phase” may be several weeks or months. Symptoms, which when they do appear often escalate rather rapidly, may include respiratory distress, dyspnea, tremors, delusions, memory loss, kidney and renal failure, various autoimmune diseases, etc.

Mercury is present in the earth crust and to some extent everybody is exposed to it in some form or another, through the air that we inhale, drinking water, food, etc. The main risk is from elevated concentrations in the environment, mainly caused by human activities such as mining. In Canada, for example, there are over 4000 known sites of elevated levels of heavy metals in soil, many of which have elevated levels of mercury [MOO2009]. The radionuclide ^{203}Hg is used to study various aspects pertaining to soil contamination, such as its bioavailability to seeds and plants, transport, accumulation and the risk associated with mercury in its various chemical forms – elemental, inorganic and organic.

Appendix B

MCNP 6.1 input code to model the VBTS

```
Samples irradiated in neutron flux behind VBTS target - INCL4/ABLA selected
c ----------------------------------------------------------------------
c *** CELL CARDS ***
c ----------------------------------------------------------------------
c     Inside the vault: air-filled
  1   601  -0.001225   -101 201 202 #5 #6 #7 #8 #9 #10 #11 #12  &
                        #13 #14 #15 #16 #17 #18 #19 #20 #21 #22 &
                        #23 #24 #25 #26 #27 #30 #33 #34 #35 #36 &
                        #37 #38 #39 #40 #41 #42 #43 #44 #45 #46 &
                        #47                                      imp:h,n=1
c     Concrete building structures (floor, ceiling and walls)
  2   602  -2.35        101 -102 201 202 #28 #29 #30 #31 #32      imp:h,n=1
c     Stainless Steel 316 beam pipe (vacuum filled)
  3   0                -201 #46 #47                              imp:h,n=1
  4   605  -7.92         201 -202 #46 #47                         imp:h,n=1
c     Target station (local iron shielding)
  5   608  -7.874        203 -204 202                             imp:h,n=1
c     Target station (local borated paraffin wax shielding)
  6   607  -0.93         204 -205 202                             imp:h,n=1
c     Target station (local outer lead shielding)
  7   606  -11.35        205 -206 202                             imp:h,n=1
c     Helium-cooled double-foil Havar window (He @ 1.25 Atm)
  8   615  -8.3         -207                                      imp:h,n=1
  9   616  -0.00022313 -208                                      imp:h,n=1
 10   615  -8.3         -209                                      imp:h,n=1
c     Target holder Aluminium entrance window
 11   603  -2.699       -210                                      imp:h,n=1
c     Cooling-water layer: 1st
 12   609  -1.0         -211                                      imp:h,n=1
c     Stainless steel-encapsuled Rb target
 13   605  -7.92        -212 213                                  imp:h,n=1
 14   611  -1.53        -213                                      imp:h,n=1
c     Cooling-water layer: 2nd
 15   609  -1.0         -214                                      imp:h,n=1
c     Niobium-encapsulated Ga target
 16   612  -8.57        -215 216                                  imp:h,n=1
 17   613  -5.91        -216                                      imp:h,n=1
c     Cooling-water layer: 3rd
 18   609  -1.0         -217                                      imp:h,n=1
c     Aluminium target backing
 19   603  -2.699       -218                                      imp:h,n=1
c     Aluminium target-holder body
 20   603  -2.699       -220 219                                  imp:h,n=1
```

```
c     Radial cooling-water layer
 21   609  -1.0        -219 221                                  imp:h,n=1
C     Neutron activation chamber (Nb top plate)
 22   612  -8.57       -222                                      imp:h,n=1
C     Neutron activation chamber (PVC roof of chamber)
 23   610  -1.406      -223                                      imp:h,n=1
c     Neutron activation chamber (source cavity)
 24   601  -0.001225    224 -225                                 imp:h,n=1
c     Neutron activation chamber (bottom of source cavity - paper)
 25   614  -1.20        226 -227                                 imp:h,n=1
C     Neutron activation chamber (PVC floor of chamber)
 26   610  -1.406      -228                                      imp:h,n=1
c     Neutron activation chamber (PVC chamber radial wall)
 27   610  -1.406       229 -230                                 imp:h,n=1
c     Pit in vault floor (filled with air)
 28   601  -0.001225   -231 #29 #30                              imp:h,n=1
c     Iron forward shield in pit
 29   608  -7.874      -232                                      imp:h,n=1
c     Forward paraffin wax with B4C shield
 30   607  -0.93       -233                                      imp:h,n=1
c     Water tanks (with Na-pentaborate) to reduce floor activation
 31   604  -7.82        234 -235 #32                             imp:h,n=1
 32   617  -1.04        236 -237                                 imp:h,n=1
c     Stainless steel pusher assembly
 33   605  -7.92        238 -239 #34                             imp:h,n=1
 34   601  -0.001225    240 -241                                 imp:h,n=1
c     Bottom Al plate of support structure
 35   603  -2.699      -242  243                                 imp:h,n=1
c     Top Al plate of support structure
 36   603  -2.699      -244  245                                 imp:h,n=1
c     Middle Al plate of support structure
 37   603  -2.699      -246  247                                 imp:h,n=1
c     Four vertical supports
 38   603  -2.699      -248 #35 #36 #37                          imp:h,n=1
 39   603  -2.699      -249 #35 #36 #37                          imp:h,n=1
 40   603  -2.699      -250 #35 #36 #37                          imp:h,n=1
 41   603  -2.699      -251 #35 #36 #37                          imp:h,n=1
 42   603  -2.699      -252 #35 #36 #37                          imp:h,n=1
 43   603  -2.699      -253 #35 #36 #37                          imp:h,n=1
 44   603  -2.699      -254 #35 #36 #37                          imp:h,n=1
 45   603  -2.699      -255 #35 #36 #37                          imp:h,n=1
c     Graphite collimator
 46   618  -2.266       256 -257                                 imp:h,n=1
 47   619  -8.933       258 -259                                 imp:h,n=1
c     Cookie cutter cell (ccc)
 48    0     -280                                                imp:h,n=1
c     Outside world-void (UMWELT)
999    0      102 201 202                                       imp:h,n=0
c ---------------------------------------------------------------------------

c ---------------------------------------------------------------------------
c *** SURFACE CARDS ***
c ---------------------------------------------------------------------------
c  Vault inner dimensions (4m x 4m; 2m height)
c
  101   RPP -200 200 -200 200 0 200
c
c  Wall, floor and roof outer concrete surfaces
c
```

```
  102   RPP -600 600 -600 600 -400 400
c
c  Beamline
c
  201   RCC 0 0 46.52    0 0 372.995 5.5
  202   RCC 0 0 46.52    0 0 372.995 6.0
c
c  Inner iron shield
c
  203   RCC 0 0 0        0 0 67.45   39.0
  204   RCC 0 0 0        0 0 116.45  88.0
c
c  Middle B4C + paraffin wax shield
c
  205   RCC 0 0 0        0 0 137.45  109.0
c
c  Outer lead shield layer
  206   RCC 0 0 0        0 0 141.45  113.0
c
  207   RCC 0 0 46.505   0 0 0.005   2.5    $ Inner Havar foil (layer no. 1)
  208   RCC 0 0 45.005   0 0 1.5     2.5    $ Helium Cooling gas (layer no. 2)
  209   RCC 0 0 45.0     0 0 0.005   2.5    $ Outer Havar foil (layer no. 3)
c
c  Target materials located on the beam axis
c
  210   RCC 0 0 44.6     0 0 0.20    5.0    $ Al (layer no. 5) tgt holder window
  211   RCC 0 0 44.48    0 0 0.12    2.0    $ H2O (layer no. 6)
  212   RCC 0 0 42.68    0 0 1.8     2.0    $ SS-316 capsule(layers no. 7 and 9)
  213   RCC 0 0 42.73    0 0 1.7     1.9    $ Rb (layer no. 8)
  214   RCC 0 0 42.56    0 0 0.12    2.0    $ H2O (layer no. 10)
  215   RCC 0 0 42.085   0 0 0.475   2.0    $ Nb (layers no. 11 and 13)
  216   RCC 0 0 42.135   0 0 0.375   1.95   $ Ga (layer no. 12)
  217   RCC 0 0 41.965   0 0 0.12    2.0    $ H2O (layer no. 14)
  218   RCC 0 0 40.965   0 0 1.000   5.0    $ Al (layer no. 15) tgt holder back
c
c  Target holder
c
  219   RCC 0 0 41.965   0 0 2.635   2.2    $ Al target holder inner radius
  220   RCC 0 0 41.965   0 0 2.635   5.0    $ Al target holder outer radius
c
c  Radial cooling-water layer
c
  221   RCC 0 0 41.965   0 0 2.635   2.0    $ H2O layer inner radius
c
c  Sample chamber with materials to activate with neutrons
c
  222   RCC 0 0 40.815   0 0 0.05    4.6    $ Nb (layer no. 17) locating plate
  223   RCC 0 0 40.615   0 0 0.2     4.0    $ PVC (layer no. 18) chamber "roof"
  224   RCC 0 0 40.115   0 0 0.5     1.0    $ Air (top part of center cavity)
  225   RCC 0 0 40.115   0 0 0.5     3.5    $ Air (layer no. 19) sample cavity
  226   RCC 0 0 39.615   0 0 0.5     1.0    $ Air (bottom part of center cavity)
  227   RCC 0 0 39.615   0 0 0.5     3.5    $ Paper (layer no. 20) paper cavity
  228   RCC 0 0 39.415   0 0 0.2     4.0    $ PVC (layer no. 21) chamber "floor"
  229   RCC 0 0 39.615   0 0 1.0     3.5    $ PVC radial inner wall
  230   RCC 0 0 39.615   0 0 1.0     4.0    $ PVC radial outer wall
c
c  Structures under vault floor
c
  231   RCC 0 0 -300.0   0 0 300.0   49.0   $ Pit in floor (filled with air)
```

```
  232   RCC 0 0 -50.0    0 0 50.0    49.0   $ Iron forward shield in pit
  233   RCC 0 0 -70.0    0 0 20.0    49.0   $ Forward paraffin wax & B4C shield
  234   RCC 0 0 -20.0    0 0 20.0    49.0   $ Inner radius of water tanks
  235   RCC 0 0 -20.0    0 0 20.0    109.0  $ Outer radius of water tanks
  236   RCC 0 0 -19.7    0 0 19.4    49.3   $ Inner radius of solution
  237   RCC 0 0 -19.7    0 0 19.4    108.7  $ Outer radius of solution
c
c  Pusher assembly
c
  238   RCC 0 0 26.815   0 0 14.0    4.0    $ Inner radius of pusher assembly
  239   RCC 0 0 26.815   0 0 14.0    15.0   $ Outer radius of pusher assembly
  240   RCC 0 0 27.715   0 0 12.8    4.05   $ Inner radius compressed air volume
  241   RCC 0 0 27.715   0 0 12.8    14.95  $ Outer radius compressed air volume
c
c  Aluminium support structure
c
  242   RPP -27  27   -27  27     0  2.0    $ Bottom plate of support structure
  243   RCC 0 0 0        0 0 2       9.5    $ Hole in bottom plate
  244   RPP -27  27   -27  27    58  60     $ Top plate of support structure
  245   RCC 0 0 58       0 0 2       6.5    $ Hole in top plate
  246   RPP -27  27   -27  27  24.8  26.8   $ Middle plate of support structure
  247   RCC 0 0 24.8     0 0 2       9.5    $ Hole in middle plate
  248   RPP -27 -25   -27 -25    0   60     $ Vertical support 1
  249   RPP -27 -25    25  27    0   60     $ Vertical support 2
  250   RPP  25  27   -27 -25    0   60     $ Vertical support 3
  251   RPP  25  27    25  27    0   60     $ Vertical support 4
  252   RPP -1   1     25  27    0   60     $ Vertical support 5
  253   RPP -1   1    -27 -25    0   60     $ Vertical support 6
  254   RPP -27 -25   -1   1     0   60     $ Vertical support 7
  255   RPP  25  27   -1   1     0   60     $ Vertical support 8
c
c  Graphite collimator with copper base
c
  256   RCC 0 0 48.92   0 0 4.5      1.8    $ Inner graphite aperture
  257   RCC 0 0 48.92   0 0 4.5      7.0    $ Graphite collimator outer radius
  258   RCC 0 0 46.92   0 0 2.0      2.0    $ Aperture in copper base plate
  259   RCC 0 0 46.92   0 0 2.0      7.6    $ Copper base plate
c
c Surface card for ccc (used when Gaussian beam is selected)
  280   cz 1.8                              $ 3.6 cm aperture of collimator
c ---------------------------------------------------------------------------

c ---------------------------------------------------------------------------
c *** DATA CARDS ***
c ---------------------------------------------------------------------------
mode  h n
MPHYS  ON
PHYS:h 70
PHYS:n 72
c
m601  7014.   -0.755636    $ Air (US S. Atm at sea level: density = 0.001225)
      8016.   -0.231475
      18036.  -3.9e-005
      18038.  -8.0e-006
      18040.  -0.012842
c
m602  1001.   -0.0221      $ Concrete, ordinary (density = 2.35)
      6000.   -0.002484
      8016.   -0.57493
```

```
      11023.  -0.015208
      12024.  -0.0009869999
      12025.  -0.00013
      12026.  -0.000149
      13027.  -0.019953
      14028.  -0.279871
      14029.  -0.014677
      14030.  -0.010079
      19039.  -0.009336
      19040.  -1.0e-006
      19041.  -0.000708
      20040.  -0.041526
      20042.  -0.000291
      20043.  -6.2e-005
      20044.  -0.000974
      20046.  -2.0e-006
      20048.  -9.6e-005
      26054.  -0.000367
      26056.  -0.005912
      26057.  -0.000138
      26058.  -1.9e-005
c
m603  13027.  -1          $ 100% Aluminum 27 (density = 2.699)
c
m604  6000.   -0.005       $ Steel, Carbon (density = 7.82)
      26054.  -0.056701
      26056.  -0.914106
      26057.  -0.021303
      26058.  -0.00289
c
m605  14028.  -0.009187    $ Steel, Stainless 316 (density = 7.92)
      14029.  -0.000482
      14030.  -0.000331
      24050.  -0.007095
      24052.  -0.142291
      24053.  -0.016443
      24054.  -0.004171
      25055.  -0.02
      26054.  -0.037326
      26056.  -0.601748
      26057.  -0.014024
      26058.  -0.001903
      28058.  -0.080873
      28060.  -0.031984
      28061.  -0.001408
      28062.  -0.004546
      28064.  -0.001189
      42092.  -0.003554
      42094.  -0.002264
      42095.  -0.003937
      42096.  -0.004169
      42097.  -0.002412
      42098.  -0.006157
      42100.  -0.002507
c
m606  82204.  -0.013781    $ Lead (density = 11.35)
      82206.  -0.239557
      82207.  -0.220743
      82208.  -0.525919
```

```
c
m607  1001.   -0.142661    $ Borated (4% B4C by weight) paraffin wax (density = 0.93)
      6000.   -0.817339
      5010.   -0.007960
      5011.   -0.032040
c
m608  26054.  -0.056986    $ Iron (density = 7.874)
      26056.  -0.918699
      26057.  -0.02141
      26058.  -0.002905
c
m609  1001.   -0.111894    $ Liquid water (density = 1.000)
      8016.   -0.888106
c
m610 1001.    -0.048382    $ Polyvinyl chloride (PVC plastic density = 1.406)
     6000.    -0.384361
     17035.   -0.423941
     17037.   -0.143316
c
m611 37085.   -0.72        $ Natural rubidium (density = 1.53)
     37087.   -0.28
c
m612 41093.   -1           $ 100% Nb93 (density = 8.57)
c
m613 31068.   -1           $ 100% Ga68 (density = 5.91)
c
m614 1001.    -0.05692     $ Paper (density = 1.20)
     6000.    -0.502646
     7014.    -0.019265
     8016.    -0.419
     17037.   -0.002169
c
m615 27059.   -0.425       $ Havar foil (density = 8.3)
     24052.   -0.195
     28000.   -0.127
     74000.   -0.028
     25055.   -0.016
     26000.   -0.183
     6000.    -0.026
c
m616 2004.    -1           $ 100% He4 (density = 0.0001785 at 1 Atm)
c
m617 1001.    -0.107418    $ Liquid Water with 4% Sodium pentaborate
     8016.    -0.882858    $ by weight (density = 1.04)
     5010.    -0.001935
     5011.    -0.007789
c
m618 6000.    -1.000000    $ graphite (density = 2.266)
c
m619 29063.   -0.6915      $ Copper (density = 8.933)
     29065.   -0.3085
c ---------------------------------------------------------------------------
c ** Physics Models INCL4 and ABLA enabled in this run. See choices below **
c ---------------------------------------------------------------------------
LCA 2j 0 5j 2
LEA 6j 2
c
c  Bertini/ABLA      LCA(3) = 1 ; LCA(9) = 0 ; LEA(7) = 2
c  Bertini/Dresner   LCA(3) = 1 ; LCA(9) = 0 ; LEA(7) = 0
```

```
c  CEM 03.03         not used   ; LCA(9) = 1 ; not used
c  INCL4/ABLA        LCA(3) = 0 ; LCA(9) = 2 ; LEA(7) = 2
c  ISABEL/ABLA       LCA(3) = 2 ; LCA(9) = 0 ; LEA(7) = 2
c  ISABEL/Dresner    LCA(3) = 2 ; LCA(9) = 0 ; LEA(7) = 0
c ---------------------------------------------------------------------
c *** Define the beam in negative z direction ***
c ---------------------------------------------------------------------
 sdef  pos  =  0  0  160
       vec  =  0  0  1
       dir  = -1
       par  =  h
       erg  =  66
       axs  =  0  0  1
       ext  =  0
       rad  =  D1
c Uniform beam profile (comment out if using Gauusian profile)
 SI1    0   1.8    $ radial sampling range: 0 to 18 mm: beam width = 36 mm
 SP1   -21  1      $ radial sampling weighting : r^1 for the disk
c Gaussian proton beam with cookie cutter constraint at radius = 1.8 cm
c collimator aperture (of 3.6 cm diameter). Same sdef as above up to ext = 0
c     x   = D1
c     y   = D2
c     CCC = 48
c     SP1 -41 0.75 0.9
c     SP2 -41 0.75 0.9
c ---------------------------------------------------------------------
c *** TALLIES ***
c ---------------------------------------------------------------------
 f4:n 24
c 63 group LaBauve neutron energy group structure from CINDER90
c up to last value lower than 1 MeV, then 1 MeV bins up to 67 MeV.
 e4 1.000e-11  5.000e-09  1.000e-08  1.500e-08  2.000e-08  2.500e-08 &
    3.000e-08  3.500e-08  4.200e-08  5.000e-08  5.800e-08  6.700e-08 &
    8.000e-08  1.000e-07  1.520e-07  2.510e-07  4.140e-07  6.830e-07 &
    1.125e-06  1.855e-06  3.059e-06  5.043e-06  8.315e-06  1.371e-05 &
    2.260e-05  3.727e-05  6.144e-05  1.013e-04  1.670e-04  2.754e-04 &
    4.540e-04  7.485e-04  1.234e-03  2.035e-03  2.404e-03  2.840e-03 &
    3.338e-03  5.603e-03  9.403e-03  1.505e-02  1.997e-02  2.526e-02 &
    4.087e-02  6.738e-02  1.111e-01  1.832e-01  3.020e-01  3.887e-01 &
    4.979e-01  0.639279   0.82085    1.0        2.0        3.0       &
    4.0        5.0        6.0        7.0        8.0        9.0       &
    10.0       11.0       12.0       13.0       14.0       15.0      &
    16.0       17.0       18.0       19.0       20.0       21.0      &
    22.0       23.0       24.0       25.0       26.0       27.0      &
    28.0       29.0       30.0       31.0       32.0       33.0      &
    34.0       35.0       36.0       37.0       38.0       39.0      &
    40.0       41.0       42.0       43.0       44.0       45.0      &
    46.0       47.0       48.0       49.0       50.0       51.0      &
    52.0       53.0       54.0       55.0       56.0       57.0      &
    58.0       59.0       60.0       61.0       62.0       63.0      &
    64.0       65.0       66.0       67.0
c
 f14:n 24
 e14 0 1i 67
c
nps  200000000
ctme 110000
print
```

Appendix C

Calculated physical yields: TENDL-2015

Table C.1: Physical yields determined from TENDL-2015 cross sections and neutron spectra generated with MCNP 6.1.

ID	Reaction	Physical yield (Bq μAh^{-1} g^{-1})					
		Bertini ABLA	Bertini Dresner	CEM	INCL ABLA	ISABEL ABLA	ISABEL Dresner
1	^{9}Be(n,3n)^{7}Be	55.8	55.9	51.9	42.3	58.8	58.8
2	^{23}Na(n,2n)^{22}Na	60.6	60.5	44.8	33.1	64.2	64.1
3	^{23}Na(n,γ)^{24}Na	2705.0	3577.2	2461.7	2669.4	2551.5	3306.4
4	^{nat}Ti(n,x)^{47}Ca	42.2	41.8	31.9	24.2	44.4	44.2
5	^{nat}Ti(n,x)^{44m}Sc	222.5	222.6	202.7	164.5	234.7	234.9
6	^{nat}Ti(n,x)^{46}Sc	295.7	287.5	240.1	203.4	306.5	300.0
7	^{nat}Ti(n,x)^{47}Sc	11987.0	11880.6	9137.4	7096.0	12641.5	12559.9
8	^{nat}Ti(n,x)^{48}Sc	6060.4	5903.5	4454.4	3525.8	6299.3	6180.2
9	^{55}Mn(n,x)^{48}V	0.37	0.37	0.46	0.50	0.38	0.38
10	^{55}Mn(n,x)^{51}Cr	14.3	14.3	16.5	15.2	14.7	14.7
11	^{55}Mn(n,4n)^{52}Mn	266.2	266.2	265.5	222.3	276.8	276.9
12	^{55}Mn(n,2n)^{54}Mn	476.3	471.9	342.3	253.1	501.1	497.9
13	^{59}Co(n,x)^{52}Mn	0.75	0.75	0.93	0.97	0.77	0.77
14	^{59}Co(n,x)^{54}Mn	8.75	8.75	7.71	6.12	9.28	9.28
15	^{59}Co(n,p)^{59}Fe	270.2	255.8	196.6	172.7	274.7	263.3
16	^{59}Co(n,4n)^{56}Co	19.8	19.8	19.6	16.4	20.6	20.6
17	^{59}Co(n,3n)^{57}Co	118.3	118.3	94.2	71.6	126.2	126.3
18	^{59}Co(n,2n)^{58}Co	1923.3	1907.3	1390.4	1028.8	2025.5	2013.8
19	^{59}Co(n,γ)^{60}Co	16.9	24.3	16.0	17.6	15.8	22.2
20	^{nat}Ni(n,x)^{51}Cr	2.87	2.87	2.46	1.98	3.04	3.05
21	^{nat}Ni(n,x)^{52}Mn	25.4	25.4	28.2	25.1	26.1	26.1
22	^{nat}Ni(n,x)^{54}Mn	10.4	10.4	7.94	5.95	11.1	11.1
23	^{nat}Ni(n,x)^{59}Fe	6.82	6.73	5.15	3.95	7.17	7.11
24	^{nat}Ni(n,x)^{56}Co	140.8	140.9	118.5	92.3	149.7	149.9
25	^{nat}Ni(n,x)^{57}Co	396.6	393.5	290.1	215.8	417.9	415.7
26	^{nat}Ni(n,x)^{58}Co	2107.1	1871.0	1599.6	1866.5	1985.5	1783.4
27	^{nat}Ni(n,x)^{60}Co	3.88	3.69	2.84	2.41	3.96	3.82

Table C.1: Physical yields determined from TENDL-2015 cross sections and neutron spectra generated with MCNP 6.1 (continuing from previous page).

ID	Reaction	Physical yield (Bq μAh^{-1} g^{-1})					
		Bertini ABLA	Bertini Dresner	CEM	INCL ABLA	ISABEL ABLA	ISABEL Dresner
28	^{nat}Ni(n,xn)^{56}Ni	28.9	28.9	25.5	20.3	30.6	30.7
29	^{nat}Ni(n,xn)^{57}Ni	5678.7	5663.1	4233.0	3149.1	6008.4	5998.4
30	^{nat}Br(n,x)^{75}Se	2.31	2.31	2.60	2.34	2.38	2.38
31	^{nat}Br(n,x)^{74}As	39.2	39.3	34.7	27.7	41.6	41.7
32	^{nat}Br(n,xn)^{77}Br	8448.2	8448.5	6717.1	5100.9	9010.0	9019.5
33	^{81}Br(n,γ)^{82}Br	47780.5	72164.9	46400.1	49308.8	44124.5	66659.6
34	^{nat}Rb(n,x)^{82}Br	1020.9	1016.0	817.1	632.4	1074.2	1070.8
35	^{nat}Rb(n,xn)^{83}Rb	318.2	318.2	250.5	189.3	339.5	339.8
36	^{nat}Rb(n,xn)^{84}Rb	3036.3	3013.5	2213.8	1641.2	3200.9	3184.7
37	^{nat}Rb(n,x)^{86}Rb	3915.7	4806.1	3274.7	3003.1	3887.5	4704.5
38	^{89}Y(n,x)^{83}Rb	3.11	3.11	3.42	3.01	3.20	3.20
39	^{89}Y(n,x)^{84}Rb	35.2	35.2	32.6	26.5	37.1	37.1
40	^{89}Y(n,x)^{86}Rb	99.0	98.5	73.8	55.4	104.3	103.9
41	^{89}Y(n,4n)^{86}Y	7289.2	7289.9	7291.0	6111.9	7575.2	7576.0
42	^{89}Y(n,3n)^{87}Y	11072.0	11073.0	8866.9	6738.3	11818.9	11834.5
43	^{89}Y(n,3n)^{87m}Y	50819.3	50824.9	40841.1	31087.1	54238.6	54310.2
44	^{89}Y(n,2n)^{88}Y	1078.5	1071.9	772.9	567.5	1137.2	1132.3
45	^{93}Nb(n,x)^{87}Y	55.4	55.4	58.3	50.4	57.2	57.2
46	^{93}Nb(n,x)^{88}Y	8.21	8.21	7.25	5.78	8.70	8.71
47	^{93}Nb(n,x)^{89}Zr	139.2	139.1	155.5	140.0	143.0	143.0
48	^{93}Nb(n,4n)^{90}Nb	8809.3	8813.6	8380.9	6885.1	9251.5	9255.2
49	^{93}Nb(n,3n)^{91m}Nb	163.6	163.6	127.9	96.5	174.4	174.5
50	^{93}Nb(n,2n)^{92m}Nb	4569.6	4485.1	3309.3	2509.0	4772.9	4710.9
51	^{103}Rh(n,x)^{96}Tc	112.4	112.3	130.0	118.7	115.1	115.2
52	^{103}Rh(n,p)^{103}Ru	89.9	85.4	65.8	57.0	91.7	88.2
53	^{103}Rh(n,5n)^{99g}Rh	25.8	25.8	27.3	23.4	26.6	26.6
54	^{103}Rh(n,4n)^{100}Rh	5115.3	5118.9	4545.3	3613.2	5425.5	5430.1
55	^{103}Rh(n,3n)^{101g}Rh	7.92	7.92	5.81	4.25	8.46	8.47
56	^{103}Rh(n,3n)^{101m}Rh	8761.1	8759.6	6490.3	4765.8	9357.9	9365.5
57	^{103}Rh(n,2n)^{102g}Rh	234.3	229.2	167.3	126.9	243.8	240.0
58	^{103}Rh(n,2n)^{102m}Rh	38.4	37.8	27.5	20.5	40.2	39.8
59	^{nat}Ag(n,x)^{105}Rh	592.5	592.4	462.9	349.2	631.0	631.5
60	^{nat}Ag(n,xn)^{105}Ag	635.7	635.6	486.9	364.1	677.0	677.5
61	^{nat}Ag(n,xn)^{106m}Ag	3522.5	3480.7	2648.8	2012.7	3696.6	3666.3
62	^{109}Ag(n,γ)^{110m}Ag	43.4	59.2	40.6	45.0	40.2	54.0
63	^{nat}In(n,x)^{110m}Ag	1.94	1.94	1.69	1.33	2.06	2.06
64	^{115}In(n,p)^{115m}Cd	33.3	33.1	24.8	18.7	35.2	35.0
65	^{nat}In(n,xn)^{111}In	808.3	808.2	656.2	505.5	857.8	858.4
66	^{nat}In(n,x)^{114m}In	2195.2	2242.2	1617.0	1274.9	2273.3	2321.0

Table C.1: Physical yields determined from TENDL-2015 cross sections and neutron spectra generated with MCNP 6.1 (continuing from previous page).

ID	Reaction	Physical yield (Bq μAh^{-1} g^{-1})					
		Bertini ABLA	Bertini Dresner	CEM	INCL ABLA	ISABEL ABLA	ISABEL Dresner
67	^{127}I(n,x)^{120m}Sb	3.35	3.35	3.90	3.61	3.43	3.43
68	^{127}I(n,x)^{122}Sb	97.6	97.6	84.3	66.5	103.6	103.8
69	^{127}I(n,x)^{124}Sb	5.05	5.03	3.92	3.00	5.31	5.29
70	^{127}I(n,x)^{123m}Te	2.68	2.68	2.92	2.58	2.76	2.76
71	^{127}I(n,5n)^{123}I	7102.8	7100.7	7447.5	6370.1	7327.1	7328.0
72	^{127}I(n,4n)^{124}I	4032.6	4035.4	3565.2	2828.9	4279.9	4283.8
73	^{127}I(n,2n)^{126}I	7959.4	7822.7	5714.2	4303.1	8314.5	8213.7
74	^{133}Cs(n,5n)^{129}Cs	2502.4	2501.8	2596.6	2214.7	2586.0	2586.3
75	^{133}Cs(n,2n)^{132}Cs	16273.7	16010.1	11762.2	8861.8	17022.2	16828.8
76	^{133}Cs(n,γ)^{134}Cs	230.0	338.9	221.0	239.7	214.9	313.7
77	^{141}Pr(n,x)^{139}Ce	359.2	359.2	273.4	203.4	383.5	383.9
78	^{141}Pr(n,p)^{141}Ce	52.3	52.0	39.0	29.2	55.3	55.1
79	^{141}Pr(n,γ)^{142}Pr	28837.8	42459.6	27938.3	29866.9	26638.1	39167.0
80	^{nat}Gd(n,x)^{156}Eu	81.5	81.4	68.0	53.1	86.3	86.3
81	^{nat}Gd(n,x)^{157}Eu	1983.4	1982.6	1653.4	1289.2	2101.3	2102.1
82	^{nat}Gd(n,xn)^{151}Gd	9.98	9.95	9.11	7.47	10.5	10.4
83	^{nat}Gd(n,x)^{153}Gd	51.6	51.4	41.6	32.1	54.6	54.5
84	^{nat}Gd(n,x)^{159}Gd	49317.4	56324.3	40258.2	37736.1	48588.9	55268.1
85	^{160}Gd(n,γ)^{161}Gd$\rightarrow^{161}$Tb	2895.3	4176.5	2789.3	2999.8	2672.2	3839.3
86	^{169}Tm(n,5n)^{165}Tm	6972.3	6975.2	6741.5	5564.5	7292.6	7294.2
87	^{169}Tm(n,3n)^{167}Tm	6038.1	6035.8	4414.1	3233.3	6423.2	6424.7
88	^{169}Tm(n,2n)^{168}Tm	1062.3	1030.3	767.8	601.6	1099.6	1075.6
89	^{181}Ta(n,p)^{181}Hf	16.5	16.5	12.5	9.3	17.5	17.5
90	^{181}Ta(n,5n)^{177}Ta	6294.0	6298.9	5766.2	4645.4	6649.3	6652.2
91	^{181}Ta(n,γ)^{182}Ta	2532.0	3740.3	2421.8	2665.2	2412.0	3418.9
92	^{197}Au(n,x)^{192}Ir	1.12	1.12	1.00	0.79	1.19	1.19
93	^{197}Au(n,4n)^{194}Au	14614.9	14617.0	11772.7	8947.2	15631.8	15658.4
94	^{197}Au(n,3n)^{195}Au	285.3	285.2	205.2	149.1	303.6	303.6
95	^{197}Au(n,2n)^{196}Au	13269.1	12854.9	9545.3	7471.0	13716.3	13405.7
96	^{197}Au(n,γ)^{198g}Au	64068.6	93641.6	61166.7	66819.3	59853.4	86634.3
97	^{nat}Tl(n,x)^{203}Hg	31.1	31.0	25.8	20.2	32.8	32.8
98	^{nat}Tl(n,xn)^{200}Tl	5480.0	5480.5	5065.9	4133.9	5773.2	5779.3
99	^{nat}Tl(n,xn)^{201}Tl	5880.8	5881.1	4845.6	3751.0	6225.5	6228.0
100	^{nat}Tl(n,xn)^{202}Tl	3683.6	3630.4	2798.6	2152.1	3872.1	3834.7
101	^{209}Bi(n,6n)^{204}Bi	5104.6	5101.4	5821.1	5215.5	5229.6	5232.3
102	^{209}Bi(n,5n)^{205}Bi	787.7	788.1	754.9	619.7	824.3	824.5
103	^{209}Bi(n,4n)^{206}Bi	4355.2	4356.0	3515.7	2674.9	4657.9	4665.6
104	^{209}Bi(n,3n)^{207}Bi	4.57	4.57	3.28	2.38	4.86	4.86

Appendix D

Calculated physical yields: TENDL-2017

Table D.1: Physical yields determined from TENDL-2017 cross sections and neutron spectra generated with MCNP 6.1.

ID	Reaction	Physical yield (Bq μAh^{-1} g^{-1})					
		Bertini ABLA	Bertini Dresner	CEM	INCL ABLA	ISABEL ABLA	ISABEL Dresner
1	^{9}Be(n,3n)^{7}Be	55.8	55.9	51.9	42.3	58.8	58.8
2	^{23}Na(n,2n)^{22}Na	47.4	47.3	34.6	25.4	50.2	50.2
3	^{23}Na(n,γ)^{24}Na	2565.7	3548.3	2360.7	2557.7	2398.5	3262.9
4	^{nat}Ti(n,x)^{47}Ca	169.7	169.6	145.8	115.0	179.6	179.6
5	^{nat}Ti(n,x)^{44m}Sc	226.8	226.8	205.6	166.2	239.3	239.5
6	^{nat}Ti(n,x)^{46}Sc	270.9	260.8	214.9	187.2	278.8	270.7
7	^{nat}Ti(n,x)^{47}Sc	10566.9	10459.7	7939.8	6175.7	11124.6	11040.0
8	^{nat}Ti(n,x)^{48}Sc	6365.1	6184.2	4675.1	3730.2	6603.8	6466.1
9	^{55}Mn(n,x)^{48}V	0.20	0.20	0.24	0.26	0.20	0.20
10	^{55}Mn(n,x)^{51}Cr	12.9	12.9	14.5	13.2	13.3	13.3
11	^{55}Mn(n,4n)^{52}Mn	335.5	335.5	337.2	283.6	348.5	348.6
12	^{55}Mn(n,2n)^{54}Mn	477.1	472.9	343.9	254.4	502.2	499.1
13	^{59}Co(n,x)^{52}Mn	0.88	0.87	1.08	1.14	0.90	0.90
14	^{59}Co(n,x)^{54}Mn	10.2	10.2	9.0	7.1	10.8	10.8
15	^{59}Co(n,p)^{59}Fe	268.6	254.3	195.3	171.2	273.1	261.9
16	^{59}Co(n,4n)^{56}Co	19.1	19.1	18.9	15.8	19.9	19.9
17	^{59}Co(n,3n)^{57}Co	116.2	116.2	92.6	70.3	123.9	124.0
18	^{59}Co(n,2n)^{58}Co	1909.9	1893.9	1380.9	1021.8	2011.3	1999.7
19	^{59}Co(n,γ)^{60}Co	6.88	9.78	6.53	7.13	6.40	8.94
20	^{nat}Ni(n,x)^{51}Cr	2.31	2.31	2.01	1.63	2.45	2.45
21	^{nat}Ni(n,x)^{52}Mn	24.0	24.0	26.6	23.7	24.6	24.6
22	^{nat}Ni(n,x)^{54}Mn	9.52	9.52	7.36	5.56	10.12	10.12
23	^{nat}Ni(n,x)^{59}Fe	8.02	7.96	6.02	4.54	8.49	8.45
24	^{nat}Ni(n,x)^{56}Co	139.2	139.2	117.4	91.5	148.0	148.2
25	^{nat}Ni(n,x)^{57}Co	406.4	403.2	297.5	221.4	428.2	425.9
26	^{nat}Ni(n,x)^{58}Co	2143.0	1906.1	1626.9	1888.1	2023.2	1820.6
27	^{nat}Ni(n,x)^{60}Co	3.99	3.79	2.92	2.51	4.07	3.91

Table D.1: Physical yields determined from TENDL-2017 cross sections and neutron spectra generated with MCNP 6.1 (continuing from previous page).

ID	Reaction	Physical yield (Bq μAh^{-1} g^{-1})					
		Bertini ABLA	Bertini Dresner	CEM	INCL ABLA	ISABEL ABLA	ISABEL Dresner
28	^{nat}Ni(n,xn)^{56}Ni	29.3	29.3	25.8	20.6	31.0	31.1
29	^{nat}Ni(n,xn)^{57}Ni	5739.2	5723.3	4274.9	3179.2	6072.3	6062.2
30	^{nat}Br(n,x)^{75}Se	2.35	2.34	2.63	2.38	2.41	2.41
31	^{nat}Br(n,x)^{74}As	33.4	33.4	29.6	23.7	35.4	35.5
32	^{nat}Br(n,xn)^{77}Br	8532.4	8532.7	6786.8	5155.0	9099.5	9109.0
33	^{81}Br(n,γ)^{82}Br	50552.2	76123.4	48977.4	52219.1	46769.0	70308.1
34	^{nat}Rb(n,x)^{82}Br	890.0	886.7	727.5	567.0	937.0	934.7
35	^{nat}Rb(n,xn)^{83}Rb	324.9	324.9	255.7	193.2	346.7	347.0
36	^{nat}Rb(n,xn)^{84}Rb	2723.6	2700.7	1979.0	1468.5	2865.6	2848.9
37	^{nat}Rb(n,x)^{86}Rb	4161.7	5164.7	3509.0	3258.4	4117.6	5034.6
38	^{89}Y(n,x)^{83}Rb	2.48	2.48	2.74	2.42	2.55	2.55
39	^{89}Y(n,x)^{84}Rb	25.0	25.0	23.3	19.0	26.4	26.4
40	^{89}Y(n,x)^{86}Rb	95.5	95.0	72.3	54.7	100.5	100.2
41	^{89}Y(n,4n)^{86}Y	6815.3	6815.8	6823.3	5722.0	7081.9	7082.6
42	^{89}Y(n,3n)^{87}Y	10544.0	10545.1	8486.0	6462.3	11253.9	11269.2
43	^{89}Y(n,3n)^{87m}Y	48218.7	48224.7	38966.2	29729.5	51455.8	51525.5
44	^{89}Y(n,2n)^{88}Y	1110.1	1103.6	796.6	584.9	1171.0	1166.3
45	^{93}Nb(n,x)^{87}Y	55.7	55.6	58.8	50.9	57.5	57.5
46	^{93}Nb(n,x)^{88}Y	8.61	8.62	7.64	6.11	9.12	9.13
47	^{93}Nb(n,x)^{89}Zr	131.7	131.6	147.6	133.1	135.3	135.4
48	^{93}Nb(n,4n)^{90}Nb	8751.5	8755.6	8334.0	6849.5	9189.5	9193.1
49	^{93}Nb(n,3n)^{91m}Nb	163.9	163.9	128.2	96.7	174.7	174.8
50	^{93}Nb(n,2n)^{92m}Nb	4634.2	4547.1	3355.3	2546.8	4839.1	4775.0
51	^{103}Rh(n,x)^{96}Tc	131.3	131.2	151.6	138.1	134.5	134.6
52	^{103}Rh(n,p)^{103}Ru	89.9	85.4	65.8	57.0	91.7	88.2
53	^{103}Rh(n,5n)^{99g}Rh	24.4	24.4	25.8	22.1	25.1	25.1
54	^{103}Rh(n,4n)^{100}Rh	4924.6	4928.1	4374.0	3476.4	5223.6	5228.0
55	^{103}Rh(n,3n)^{101g}Rh	7.78	7.78	5.70	4.17	8.30	8.31
56	^{103}Rh(n,3n)^{101m}Rh	8606.1	8604.7	6374.7	4680.9	9192.0	9199.3
57	^{103}Rh(n,2n)^{102g}Rh	233.4	228.3	166.7	126.4	242.9	239.1
58	^{103}Rh(n,2n)^{102m}Rh	38.2	37.6	27.3	20.4	40.0	39.5
59	^{nat}Ag(n,x)^{105}Rh	677.9	677.9	528.2	397.9	722.1	722.6
60	^{nat}Ag(n,xn)^{105}Ag	598.0	597.9	456.8	340.9	637.7	638.2
61	^{nat}Ag(n,xn)^{106m}Ag	3854.8	3813.7	2870.8	2165.8	4049.5	4019.5
62	^{109}Ag(n,γ)^{110m}Ag	52.1	74.6	49.4	54.2	48.5	68.9
63	^{nat}In(n,x)^{110m}Ag	2.05	2.05	1.78	1.41	2.17	2.17
64	^{115}In(n,p)^{115m}Cd	33.3	33.1	24.8	18.7	35.2	35.0
65	^{nat}In(n,xn)^{111}In	801.2	801.1	648.6	499.0	850.5	851.1
66	^{nat}In(n,x)^{114m}In	2067.4	2108.0	1522.5	1206.0	2137.3	2179.1

Table D.1: Physical yields determined from TENDL-2017 cross sections and neutron spectra generated with MCNP 6.1 (continuing from previous page).

ID	Reaction	Physical yield (Bq μAh^{-1} g^{-1})					
		Bertini ABLA	Bertini Dresner	CEM	INCL ABLA	ISABEL ABLA	ISABEL Dresner
67	^{127}I(n,x)^{120m}Sb	2.82	2.82	3.29	3.06	2.89	2.89
68	^{127}I(n,x)^{122}Sb	96.3	96.4	83.5	65.8	102.3	102.4
69	^{127}I(n,x)^{124}Sb	4.79	4.76	3.62	2.74	5.03	5.01
70	^{127}I(n,x)^{123m}Te	1.44	1.44	1.58	1.41	1.48	1.48
71	^{127}I(n,5n)^{123}I	5441.4	5439.7	5718.8	4902.3	5612.6	5613.3
72	^{127}I(n,4n)^{124}I	3322.4	3324.6	2959.7	2358.0	3522.3	3525.3
73	^{127}I(n,2n)^{126}I	7939.4	7817.8	5733.8	4308.8	8309.3	8220.1
74	^{133}Cs(n,5n)^{129}Cs	2497.4	2496.8	2598.2	2220.1	2580.3	2580.6
75	^{133}Cs(n,2n)^{132}Cs	15150.5	14920.1	10962.2	8246.2	15858.7	15689.6
76	^{133}Cs(n,γ)^{134}Cs	228.0	336.1	219.2	237.5	213.0	311.2
77	^{141}Pr(n,x)^{139}Ce	364.7	364.7	279.9	208.9	389.4	389.8
78	^{141}Pr(n,p)^{141}Ce	52.5	52.2	39.1	29.3	55.5	55.3
79	^{141}Pr(n,γ)^{142}Pr	33420.1	49005.4	32341.4	34619.7	30868.6	45184.4
80	^{nat}Gd(n,x)^{156}Eu	76.4	76.3	64.4	50.5	80.8	80.8
81	^{nat}Gd(n,x)^{157}Eu	1984.9	1984.3	1666.2	1302.9	2102.6	2103.6
82	^{nat}Gd(n,xn)^{151}Gd	10.9	10.8	10.0	8.2	11.4	11.4
83	^{nat}Gd(n,x)^{153}Gd	52.9	52.7	42.2	32.4	56.0	55.9
84	^{nat}Gd(n,x)^{159}Gd	53428.8	61710.1	43774.5	41030.9	52699.0	60491.7
85	^{160}Gd(n,γ)^{161}Gd$\rightarrow^{161}$Tb	3434.4	4974.4	3303.1	3561.9	3179.0	4572.7
86	^{169}Tm(n,5n)^{165}Tm	6951.4	6954.3	6721.3	5547.9	7270.8	7272.4
87	^{169}Tm(n,3n)^{167}Tm	6029.6	6027.3	4408.1	3228.9	6414.2	6415.6
88	^{169}Tm(n,2n)^{168}Tm	1062.0	1030.0	767.7	601.5	1099.4	1075.4
89	^{181}Ta(n,p)^{181}Hf	16.5	16.5	12.5	9.4	17.5	17.5
90	^{181}Ta(n,5n)^{177}Ta	6278.0	6282.9	5751.5	4633.4	6632.5	6635.4
91	^{181}Ta(n,γ)^{182}Ta	2579.1	3805.9	2464.0	2713.3	2454.5	3478.8
92	^{197}Au(n,x)^{192}Ir	1.45	1.45	1.27	1.01	1.54	1.54
93	^{197}Au(n,4n)^{194}Au	14744.6	14746.3	11846.7	8993.1	15771.1	15798.1
94	^{197}Au(n,3n)^{195}Au	285.8	285.7	205.4	149.2	304.1	304.1
95	^{197}Au(n,2n)^{196}Au	13208.0	12786.3	9504.1	7455.5	13646.4	13330.0
96	^{197}Au(n,γ)^{198g}Au	71253.5	104537.6	68136.9	74269.1	66619.6	96937.0
97	^{nat}Tl(n,x)^{203}Hg	33.4	33.4	27.9	21.9	35.3	35.3
98	^{nat}Tl(n,xn)^{200}Tl	5779.9	5780.4	5382.5	4398.3	6080.7	6087.0
99	^{nat}Tl(n,xn)^{201}Tl	6070.1	6070.8	4998.0	3866.3	6430.3	6432.9
100	^{nat}Tl(n,xn)^{202}Tl	3784.2	3731.0	2863.1	2194.9	3980.8	3943.7
101	^{209}Bi(n,6n)^{204}Bi	5084.2	5081.0	5798.8	5196.2	5208.7	5211.4
102	^{209}Bi(n,5n)^{205}Bi	787.1	787.4	754.1	619.0	823.7	823.8
103	^{209}Bi(n,4n)^{206}Bi	4345.7	4346.5	3508.1	2669.1	4647.7	4655.4
104	^{209}Bi(n,3n)^{207}Bi	4.56	4.56	3.27	2.38	4.86	4.86

Appendix E

Acronyms and Abbreviations

BNL	Brookhaven National Laboratory
BOB	Beginning of bombardment
B-spline	Basis spline
CEM	Cascade-Exciton Model
EOB	End of bombardment
HEU	Highly-enriched uranium
HPGe	High-purity germanium detector
INC	Intranuclear cascade
INCL	Liège Intranuclear Cascade Model
iThemba LABS	iThemba Laboratory for Accelerator Based Sciences
LANCE	Los Alamos Neutron Science Center
LANL	Los Alamos National Laboratory
LERIB	Low-Energy Radioactive Ion Beam Project
LEU	Low-enriched uranium
LN	Liquid nitrogen
LRP	Long-range plan
MCNP	Monte Carlo N-Particle code
MEIN	Medium Energy Intense Neutron Facility
MEM	Modified Exciton Model
NIST	National Institute of Standards and Technology
NPL	Non-Proliferation Treaty
NURBS	Non-uniform rational basis spline
QMN	Quasi-monoenergetic neutrons
RSICC	Radiation Shielding Information and Computational Center
TENDL	TALYS Evaluated Nuclear Data Library
VBTS	Vertical-beam target station

References

[ADE1995] S. J. Adelstein, F. J Manning, Isotopes for Medicine and the Life Sciences. National Academies Press, 1995.

[ALL2016] J. Allison, K. Amako, J. Apostolakis, P. Arce, M. Asai, T. Aso, E. Bagli, A. Bagulya, S. Banerjee, G. Barrand, B. R. Beck, A. G. Bogdanov, D. Brandt, J. M. C. Brown, H. Burkhardt, Ph. Canal, D. Cano-Ott et al., Recent developments in Geant4. Nucl. Intrum. Meth. A 835 (2016) 186–225.

[ARM1980] T. W. Armstrong, The intranuclear-cascade-evaporation model. In Computer Techniques in Radiation Transport and Dosimetry (pp. 311-322). Springer, Boston, MA.

[AZA2018] F. Azaiez et al., Shaping the Vision for the Future 2018: Long Range Plan–2018. Available from iThemba LABS website <http://www.tlabs.ac.za/>.

[BAU2015] R. P. Baum, A. D. Puranik, H. R. Kulkarni, Peptide receptor radionuclde therapy (PRRT) of neuroendocrine tumors: current state and future perspectives. Int. J. Endo. Oncol. 2 (2015) 151–158.

[BER2001] P. Bernhardt, E. Forssell-Aronsson, L. Jacobsson, G. Skarnemark, Low-energy electron emitters for targeted radiotherapy of small tumours. Acta Oncol. 40 (2001) 602–608.

[BIS2016] J. Biswal, S. Goswami, H. J. Pant, Y. R. Bamankar, T. V. Vittalrao, R. K. Upadhay, A. Dash, Synthesis, characterization, neutron activation, and application of scandium oxide microsphere in radioactive particle tracking experiments. Ind. Eng. Chem. Res. 55 (2016) 3–12.

[BÖH2014] T. T. Böhlen, F. Cerutti, M. P. W. Chin, A. Fassò, A. Ferrari, P. G. Ortega, A. Mairani, P. R. Sala, G. Smirnov, V. Vlachoudis, The FLUKA Code: Developments and Challenges for High Energy and Medical Applications. Nucl. Data Sheets 120 (2014) 211–214.

[CAR1972] B. C. Carlson, The logarithmic mean. Am. Math. Mon. 79 (1972) 615–618.

[CERN2013] Terbium: a new 'Swiss army knife' for nuclear medicine. In: CERN Courier (Ed. C. Sutton), January 2013. Available from <http://cerncourier.com>.

[CHA2013] B. A. Chabner, J. Efstathiou, S. Dryden-Peterson: Cancer in Botswana: The second wave of AIDS in sub-Saharan Africa. The Oncologist 18 (2013) 777–778.

[CON2016] J. L. Conradie, L. S. Anthony, F. Azaiez, S. Baard, R. A. Bark, A. H. Barnard, P. Beukes, J. I. Broodryk, J. C. Cornell, J. G. de Villiers, H. du Plessis, W. Duckitt, D. T. Fourie, P. Gardiner, I. H. Kohler, J. Lawrie, C. Lussi, N. R. Mantengu, R. H. McAlister, J. Mira, H. W. Mostert, C. Naidoo, F. Nemulodi, M. Sakildien, G. F. Steyn, R. W. Thomae, M. J. van Niekerk, P. A. van Schalkwyk, A radioactive ion beam and isotope production facility for iThemba LABS. Proc. 25^{th} Russian Particle Accelerator Conference (RuPAC2016), St. Petersburg, Russia, 21–25 November, 2016, pp. 78–82. Available from <http://www.jacow.org>.

[DAD2013] R. K. Dadhich, R. P. Sharma, S. M. Kumawat, G. Singh, M. P. Sahu, Use of ^{59}Fe isotope in iron chlorosis for fodder sorghum bicolor. Noto-are 18973108: Agric. (2013) 1–5.

[DEL2014] K. A. DeLorme, Production Potential of ^{47}Sc Using Spallation Neutron Flux at the Los Alamos Isotope Production Facility. Thesis, Air Force Institute of Technology, Document AFIT-ENP-14-M-02, United States Air Force, 2014.

[DEM2000] J. F. Dempsey, D. A. Low, S. Mutic, J. Markman, A. S. Kirov, G. H. Nussbaum, J. F. Williamson, Validation of a precision radiochromic film dosimetry system for quantitative two-dimensional imaging of acute exposure dose distributions. Med. Phys. 27 (2000) 2462–2475.

[DOM2017] K. A. Domnanich, C. Müller, M. Benešová, R. Dressler, S. Haller, U. Köster, B. Ponsard, R. Schibli, A. Türler, N. P. van der Meulen, ^{47}Sc as useful β^--emitter for the radiotheragnostic paradigm: a comparative study of feasible production routes. EJNMMI Radiopharm. Chem. 2 (2017) 5.

[ENG2012] J. W. Engle, C. T. Kelsey, H. Bach, B. D. Ballard, M. E. Fassbender, K. D. John, E. R. Birnbaum, F. M. Nortier, Preliminary investigation of parasitic radioisotope production using the LANL IPF secondary neutron flux. Proc. 14^{th} Int. Workshop on Targetry and Target Chemistry, AIP Conf. Proc. 1509 (2012) 171–175.

[ENG2013] J. W. Engle, E. R. Birnbaum, M. E. Fassbender, K. D. John, F. M. Nortier, Parasitic isotopic production with cyclotron beam generated neutrons. Proc. 20^{th} Int. Conf. on Cyclotrons and their Applications, Vancouver, Canada, September 16–20, 2013, pp. 451–453. Available from <http://www.jacow.org>.

[ENG2014] J. W. Engle, M. R. James, S. G. Mashnik, C. T. Kelsey IV, L. W. Wolfsberg, D. A. Reass, M. A. Connors, H. T. Bach, M. E. Fassbender, K. D. John, E. R. Birnbaum, F. M. Nortier, MCNPX characterization of the secondary neutron flux at the Los Alamos Isotope Production Facility. Nucl. Instrum. Meth. A 754 (2014) 71–82.

[FEG2015] A. A. H. Feghhi, Z. Gholamzadeh, C. Tenreiro, Z. Alipoor, Comparison of different INC physical modles of MCNPX to compute spallation neutronics of LBE target. J. Phys. Conf. Ser. 590 (2015) 012043.

[FIL2009] D. Filges, F. Goldenbaum, Handbook of Spallation Research: Theory, Experiments and Applications. Wiley-VCH Verlag GmbH, ISBN: 978-3-527-40714-9, 2009.

[GAI1991] J. J. Gaimard, K. H. Schmidt, A reexamination of the abrasion-ablation model for the description of the nuclear fragmentation reaction. Nucl. Phys. A 531 (1991) 709–745.

[GLA2005] A. Glaser, About the enrichment limit for research reactor conversion: Why 20%? In: 27^{th} Int. Meeting on Reduced Enrichment for Research and Test Reactors (RERTR 27), Boston, 2005, pp. 1–12.

[GOO2013] J. T. Goorley, M. R. James, T. E. Booth, F. B. Brown, J. S. Bull, L. J. Cox, J. W. Durkee, J. S. Elson, M. L. Fensin, R. A. Forster, J. S. Hendricks et al., Initial MCNP 6 Release Overview – MCNP 6 version 1.0. Los Alamos National Laboratory Report LA-UR-13-22934, 2013.

[GOS1990] A. Goshtasby, F. Cheng,, B. A. Barsky, B-spline curves and surfaces viewed as digital filters. Comput. Gr. Image Process. 52 (1990) 264–275.

[HAR2010] R. L. Harrison, Introduction to Monte Carlo simulation. AIP Conf. Proc. 1204 (2010) 17–21.

[HOD2015] A. P. J. Hodgson, R. W. Grimes, M. J. D. Rushton, O. J. Marsden, The impact of neutron cross section group structures on the accuracy of radiological source models. Nucl. Sci. Eng. 181 (2015) 1–8.

[HOF2014] D. Hoffman, M. Sun, L. Yang, P. R. McDonach, F. Corwin, G. Sundaresan, V. Vijayaragavan, C. Thadigiri, N. Lamichhane, J. Zweit, Intrinsically radiolabelled [^{59}Fe]-SCIONs for dual MRI/radionuclide detection. Am. J. Nucl. Med. Mol. Imaging 4 (2014) 548–560.

[HRI2007] H. Hricak, S. J. Adelstein, P. S. Conti, J. Fowler, J. Gray, L.-W. Hu, J. Karp, T. Lewellen, R. Macklis, C. D. Maynard, T. J. Ruth, H. Schelbert, G. von Schulthess, M. R. Zalutsky, Advancing Nuclear Medicine Through Innovation. Report of the Committee on State of the Science of Nuclear Medicine, National Research Council, National Academies Press, ISBN: 0-309-11068-8 (2007). Available from <http://www.nap.edu/catalog/11985.html>.

[JEN2016] A. I. Jensen, G. W. Severin, H. B. Andreasen, P. H. Rasmussena, Stable and high-yielding intrinsic ^{59}Fe radiolabeling of the intravenous iron preparations Monofer and Cosmofer. J. Label. Compd. Radiopharm. 59 (2016) 375–382.

[KAI2011] P. Kaitaniemi, A. Boudard, S. Leray, J. Cugnon, D. Mancusi, INCL intra-nuclear cascade and ABLA de-excitation models in Geant4. Prog. Nucl. Sci. Technol. 2 (2011) 788–793.

[KAR2007] R. Karimi, C. Y. Chen, P. C. Pickhardt, N. S. Fisher, C. L. Folt, Stoichiometric controls of mercury dilution by growth. Proc. Natl. Acad. Sci. USA 104 (2007) 7477–7482.

[KAT1975] S. Katcoff, J. B. Cumming, J. Godel, V. J. Buchanan, H. Susskind, C. J. Hsu, A medium energy intense neutron facility at the Brookhaven 200 MeV linac. Nucl. Instrum. Meth. 129 (1975) 473–485.

[KNA2016] F. F. Knapp, A. Dash, Radiopharmaceuticals for Therapy. ISBN 978-81-322-2606-2, Springer, 2016, p. 150.

[KON2011] A. Yu. Konobeyev, U. Fischer, A. J. Koning, H. Leeb, S. Leray, Y. Yariv, What can we expect from the use of nuclear models implemented in MCNPX at projectile energies below 150 MeV? Detailed comparison with experimental data. J. Korean Phys. Soc. 59 (2011) 927–930.

[KÖS2017] U. Köster, Medical Radioisotopes. Presentation at the 2017 European School in Instrumentation for Particle and Astroparticle Physics (ESIPAP 2017). Available from <https://indico.cern.ch/event/571362/>.

[KWA2007] Y. H Kwak, and L. Ingall, Exploring Monte Carlo simulation applications for project management. Risk Management 9 (2007) 44–57.

[LEH2011] S. Lehenberger, C. Barkhausen, S. Cohrs, E. Fischer, J. Grünberg, A. Hohn, U. Köster, R. Schibli, A. Türler, K. Zhernosekov, The low-energy β^- and electron emitter ^{161}Tb as an alternative to ^{177}Lu for targeted radionuclide therapy. Nucl. Med. Biol. 38 (2011) 917–924.

[LER2013] S. Leray, D. Mancusi, P. Kaitaniemi, J. C. David, A. Boudard, B. Braunn, C. Cugnon, Extension of the Liège Intra Nuclear Cascade model to light-ion collisions for medical and space applications. J. Phys. Conf. Ser. 420 (2013) 012065.

[LIC2000] M. A. Lichtman, J. L. Spivak, L. A. Boxer, S. J. Shattil, E. S. Henderson, Hematology: Landmark Papers of the Twentieth Century. Academic Press Limited, San Diego, California, 2000.

[MAC2012] R. E. MacFarlane, D. W. Muir, R. M. Boicort, A. C. Kahler, The NJOY Nuclear Data Processing System, Version 2012. Los Alamos National Laboratory Report LA-UR-12-27079, 2012.

[MAS2002] S. G. Mashnik, A. J. Sierk, Recent developments of the Cascade-Exciton Model of nuclear reactions. J. Nucl. Sci. and Technol. Suppl. 2 (2002) 720–725.

[MAS2017] T. Mastren, V. Radchenko, P. D. Hopkins, J. W. Engle, J. W. Weidner, R. Copping, M. Brugh, F. M. Nortier, E. R. Birnbaum, K. D. John, M. E. H. Fassbender, Separation of ^{103}Ru from a proton irradiated thorium matrix: A potentail source of Auger therapy radionuclide ^{103m}Rh. PLOS One 12 (2017) e0190308.

[MED2012] D. Medvedev, L. Mausner, G. Meinken, S. H. Maramraju, S. D. Smith, V. Carroll, D. Schlyer, Preparation of Fe-52 core labeled iron oxide nanoparticle contrast agent and evaluation of its dual PET/MRI imaging potential in mouse. J. Nucl. Med. 53 suppl. 1 (2012) 1535.

[MIR1983] S. Mirzadeh, P. P. Parekh, S. Katcoff, Y. Y. Chu, Cross-section systematics for nuclide production at a medium energy spallation neutron facility. Nucl. Instrum. Meth. 216 (1983) 149–154.

[MOG2012] L. Moghaddam-Banaem, A. R. Jalilian, M. R. Pourjavid, E. Radfar, A. Bahrami-Samani, K. Yavari, M. Mazidi, M. Ghannadi-Maragheh, Development of a radioscandium immunoconjugate for radioimmunotherapy. Radiochim. Acta 100 (2012) 215–221.

[MOL2014] R. M. Molina, N. V. Kondura, R. J. Jimenez, G. Pyrgiotakis, P. Demokritou, W. Wohlleben, J. D.Brain, Bioavailability, distribution and clearance of tracheally instilled, gavaged or injected cerium dioxide nanoparticles and ionic cerium. Environ. Sci.: Nano 1 (2014) 561–573.

[MOO2009] R. P. Moody, J. Joncas, M. Richardson, S. Petrovic, I. Chu, Contaminated soils (II): *In vitro* dermal absorption of nickel (Ni-63) and mercury (Hg-203) in human skin. J. Toxicol. Environ. Health A 72 (2009) 551–559.

[MOR2013] I. O. Morhason-Bello, F. Odedina, T. R. Rebbeck, J. Harford, J.-M. Dangou, L. Denny, I. F Adewole, Challenges and opportunities in cancer control in Africa: a perspective from the African Organisation for Research and Training in Cancer. Lancet Oncol. 14 (2013) e142–e151.

[MOS2016] M. A. Mosby, J. W. Engle, K. R. Jackman, F. M. Nortier, E. R. Birnbaum, Determination of spallation neutron flux through spectral adjustment techniques. Nucl. Intrum. Meth. B 381 (2016) 29–33.

[MÜL2014] C. Müller, M. Bunka, S. Haller, U. Köster, V. Groehn, P. Bernhardt, N. van der Meulen, A. Türler, R. Schibli, Promising prospects for ^{44}Sc-/^{47}Sc-based theragnostics: application of ^{47}Sc for radionuclide tumor therapy in mice. J. Nucl. Med. 55 (2014) 1658–1664.

[NIST2018] National Institute of Standards and Technology (NIST), <www.nist.gov>.

[OLI2015] C. Oliveira, L. Joshee, R. K. Zalups, M. E. Pereira, C. C. Bridges, Disposition of inorganic mercury in pregnant rats and their offspring. Toxicology 335 (2015) 62–71.

[PAL1970] H. E. Palmer, J. D. Cook, K. G. Pailthorp, C. A. Finch, A whole-body counter for precision in vivo measurement of radio-iron. Phys. Med. Biol. 15 (1970) 457–465.

[PAR1994] R. M. Parr, C. R. Fjeld, Human health and nutrition: How isotopes are helping to overcome “hidden hunger”. IAEA Bulletin 4 (1994) 18–27.

[PEL2013] D. B. Pelowitz, J. T. Goorley, M. R. James, T. E. Booth, F. B. Brown, J. S. Bull, L. J. Cox, J. W. Durkee, J. S. Elson, M. L. Fensin, R. A. Forster, J. S. Hendricks et al., MCNP 6 User’s Manual. Los Alamos National Laboratory Report LA-CP-13-00634, 2013.

[PER2017] E. Pereira, L. do Quental, E. Palma, M. C. Oliveira, F. Mendes, P. Raposinho, I. Correia, J. Lavrado, S. Di Maria, A. Belchior, P. Vaz, I. Santos, A. Paulo, Evaluation of acridine orange derivatives as DNA-targeted radiopharmaceuticals for Auger therapy: Influence of the radionuclide and distance to DNA. Nature Sci. Rep. 7 (2017) 42544.

[PIZ2016] F. Pizarro, M. Olivares, C. Valenzuela, A. Brito, V. Weinborn, S. Flores, M. Arredondo, The effect of proteins from animal source foods on heme iron bioavailability in humans. Food Chem. 196 (2016) 733–738.

[PRE1997] W. H. Press, S. A. Teukolsky, W. T. Vetterling, B. P. Flannery, Numerical Recipes in Fortran 77: The Art of Scientific Computing–Second Edition. Software version 2.08, Cambridge University Press, 1997.

[QAI1974] S. M. Qaim, R. Wölfle, G. Stöcklin, Radiochemical investigations of fast neutron-induced low-yield nuclear reactions. J. Radioanal. Nucl. Chem. 21 (1974) 395–405.

[RAG2013] M. Raghavan A. Pillai, A. Dash, F. F. Knapp, Sustained availability of ^{99m}Tc: Possible paths forward. J. Nucl. Med. 54 (2013) 313–323.

[RAJ2007] J. G Rajendran, Therapeutic radioisotopes. In: Nuclear Medicine Therapy (Eds. J. Early, W. Brenner), Informa Healthcare, New York, 2007, pp. 9–20.

[REH1999] I. Rehana, K.A. Shahid, S. Husain, D. Muhammad, Characterization and excitation behaviour studies of radionuclide (scandium) in glass matrix. Appl. Radiat. Isot. 51 (1999) 115–120.

[ROC2017] D. Rochman, A. J. Koning, J. Ch. Sublet, M. Fleming, E. Bauge, S. Hilaire, P. Romain, B. Morillon, H. Duarte, S. Goriely, S. C. van der Marck, H. Sjöstrand, S. Pomp, N. Dzysiuk, O. Cabellos, H. Ferroukhi, A. Vasiliev, The TENDL library: hope, reality and future. Proc. Int. Conf. on Nuclear Data for Science and Technology, September 11–16, 2016, Bruges, Belgium, EPJ Web of Conferences 146 (2017) 02006.

[ROO2012] P. M. Roos, L. Dencker, Mercury in the spinal cord after inhalation of mercury. Basic Clin. Pharmocol. Toxicol. 111 (2012) 126–132.

[SCH2009] D. Schlyer, M. R. A. Pillai, M. Haji-Saeid, Cyclotron Produced Radionuclides: Physical Characteristics and Production Methods. IAEA Technical Reports Series 468, IAEA, Vienna, 2009.

[SET2018] D. Setiawan, I. Hastiawan, A. N. Bashiroh, Synthesis, radiochemical purity control and stability of scandium-46-1,4,7-triazacyclononane-1,4,7-triacetic acid (^{46}Sc-NOTA). Indones. J. Chem. 18 (2018) 153–158.

[SHA2005] R. M. Sharkey, H. Karacay, T. M Cardillo, C. H. Chang, W. J. McBride, W, E. A. Rossi, D. M. Goldenberg. Improving the delivery of radionuclides for imaging and therapy of cancer using pretargeting methods. Clin. Cancer Res. 11 (2005) 7109s–7121s.

[SHU2007] J. K. Shultis, R. E. Faw, An MCNP Primer. Kansas State University, Manhattan, Revised edition Sept. 2007.

[SOL2015] F. Soltani, A. B. Samani, M. Sadeghi, S. S. Arani, K. Yavari, Production of cerium-141 using ceria and nanoceria powder: a potential radioisotope for simultaneous therapeutic and diagnostic applications. J. Radioanal. Nucl. Chem. 303 (2015) 385–391.

[STE2013] G. F. Steyn, C. Vermeulen, A. H. Botha, J. L. Conradie, J. P. A. Crafford, J. L. G. Delsink, J. Dietrich, H. du Plessis, D. T. Fourie, Z. Kormány, M. J. van Niekerk, P. F. Rohwer, N. P. Stodart, J. G. de Villiers, A vertical-beam target station and high-power targetry for the cyclotron production of radionuclides with medium energy protons. Nucl. Instrum. Meth. A 727 (2013) 131–144.

[SYV2012] T. Syversen, P. Kaur, The toxicology of mercury and its compounds. J. Trace Elem. Med. Biol. 26 (2012) 215–226.

[SON2018] A. Sonzogni, NuDat 2.7: Interactive Chart of Nuclides. National Nuclear Data Centre, Brookhaven National Laboratory, Long Island, USA. Available from <http://www.nndc.bnl.gov/nudat2/>.

[TAB2018] TableCurve 2D Automated Curve Fitting and Equation Discovery. Available from <http://www.sigmaplot.co.uk/products/tablecurve2d/tablecurve2d.php>.

[TOR1985] L. Törnqvist, P. Vartia, Y. O. Vartia, How should relative changes be measured. Am. Stat. 39 (1985) 43–46.

[WAN2014] Y. Wang, S. Tu, D. Steffen, M.P. Xion, Iron complexation to histone deacetylase inhibitors SAHA and LAQ824 in PEGylated liposomes can considerably improve pharmacokinetics in rats. J. Pharm. Pharm. Sci. 17 (2014) 583–602.

[WEI1975] R. Weinreich, W. Bräutigam, H. J. Machulla, H. J. Probst, S. M. Qaim, G. Stöcklin. Production of short-lived radioisotopes for medical applications using high-energy reactions at Jülich. In: 7^{th} Int. Conf. on Cyclotrons and their Applications, Springer, 1975, pp. 457–460.

[WIL1993] W. B. Wilson, T. R. England, E. D. Arthur, C. A. Beard, C. D. Bowman, L. N. Engel, A. Gavron, D. C. George, L. L. Daemen, G. G. Hughes III, W. W. Kinnison, R. J. LaBauve, D. M. Lee, H. Lichtenstein, P. W. Lisowski, D. W. Muir, A. P. Palounek, R. T. Perry, E. J. Pitcher, R. E. Prael, G. J. Russell, G. Sanders, L. S. Waters, P. G. Young, H.-J. Ziock, Accelerator Transmutation Studies at Los Alamos with LAHET, MCNP, and CINDER'90. Los Alamos National Laboratory Report LA-UR-93-3080, 1993.

[YAN2013] L. Yang, G. Sundaresan, M. Sun, P. Jose, D. Hoffman, P. R. McDonagh, N. Lamichhane, C. S. Cutler, J. M. Perez, J. Zweit, Intrinsically radiolabeled multifunctional cerium oxide nanoparticles for *in vivo* studies. J. Mater. Chem. B 1 (2013) 1421–1431.